

Electronic Thesis and Dissertation Repository

8-22-2019 3:00 PM

Integrity Protection of the DC Microgrid

Jafar Mohammadi

The University of Western Ontario

Supervisor

Badrkhani Ajaei, Firouz

The University of Western Ontario Co-Supervisor

Mclsaac, Ken

The University of Western Ontario

Graduate Program in Electrical and Computer Engineering

A thesis submitted in partial fulfillment of the requirements for the degree in Doctor of Philosophy

© Jafar Mohammadi 2019

Follow this and additional works at: <https://ir.lib.uwo.ca/etd>



Part of the [Power and Energy Commons](#)

Recommended Citation

Mohammadi, Jafar, "Integrity Protection of the DC Microgrid" (2019). *Electronic Thesis and Dissertation Repository*. 6418.

<https://ir.lib.uwo.ca/etd/6418>

This Dissertation/Thesis is brought to you for free and open access by Scholarship@Western. It has been accepted for inclusion in Electronic Thesis and Dissertation Repository by an authorized administrator of Scholarship@Western. For more information, please contact wlsadmin@uwo.ca.

Abstract

The direct current (DC) microgrid has attracted great attention in the recent years due to its significant advantages over the alternating current (AC) microgrid. These advantages include elimination of unnecessary AC/DC power converters, lower investment cost, lower losses, higher reliability, and resilience to utility-side disturbances. A practical DC microgrid requires an effective control strategy to regulate the DC bus voltages, enable power sharing between the distributed energy resources (DERs), and provide acceptable dynamic response to disturbances. Furthermore, when the power demand of the loads is higher than the power generation of the DERs in the DC microgrid, the power balance cannot be maintained by control actions and the DERs fail to regulate the DC bus voltages. Under such conditions, it is necessary to shed some of the non-critical loads in order to protect the integrity of the DC microgrid. Thus, the DC microgrid also requires an effective load shedding scheme.

This thesis is focused on developing advanced control and load shedding strategies for integrity protection of the DC microgrid. The studies reported in this thesis include developing (i) a versatile DC bus signaling control strategy to achieve coordinated decentralized control of the DERs and loads in the DC microgrid without utilizing costly high-bandwidth communication systems, (ii) an improved mode-adaptive droop control strategy to enable desirable and reliable control mode switching by the DERs under various operating conditions, and (iii) adaptive non-communication based load shedding schemes to enable the DC microgrid to ride through the disturbances that cause large power deficit and voltage sags.

The performances of the proposed integrity protection schemes are investigated under various generation and load disturbances in both grid-connected and islanded operation modes of the DC microgrid. Comprehensive time-domain simulation studies are conducted on a detailed DC microgrid study system using the PSCAD/EMTDC software. The study results indicate that the proposed control strategies: (i) improve power sharing between the DERs, (ii) effectively regulate the DC bus voltages under various operating conditions, (iii)

improve the DC microgrid stability and its dynamic response to large disturbances, (iv) do not require an excessively large grid-tie converter or energy storage systems, and (v) enhance the DC microgrid reliability, flexibility, modularity, and expandability.

The study results also indicate that the proposed adaptive load shedding schemes (i) effectively maintain the power balance in the DC microgrid through fast and coordinated shedding of non-critical loads, (ii) prevent the bus voltages in the microgrid from falling below predetermined lower limits, (iii) ensure that the critical loads do not experience excessive steady-state voltage deviations, (iv) minimize the magnitudes and durations of temporary voltage sags caused by sudden disturbances, and (v) increase the reliability of the power supplied to the loads, by preventing over-shedding.

Keywords: DC microgrid, power sharing, voltage regulation, integrity protection, DC bus signaling, mode adaptive droop control, adaptive load shedding.

Summary for Lay Audience

The microgrid is an emerging technology that facilitates the integration of distributed energy resources (DERs) in power distribution networks, reduces the energy losses, and improves the quality and reliability of the electrical energy supplied to the consumers. In the recent years, the direct current (DC) microgrid has attracted great attention compared to the alternating current (AC) microgrid. The reason is that the majority of the DERs, e.g., photovoltaics (PVs), fuel cells, and battery energy storage systems (BESSs), provide DC power, and an increasing portion of the emerging loads require DC power, e.g., electric vehicles (EVs), consumer electronics, and LED lighting systems. The DC microgrid offers significant potential advantages over its AC counterpart. These advantages include (i) lower investment cost and power conversion losses due to elimination of unnecessary power converters, (ii) lower cable losses due to absence of skin effect, (iii) higher reliability and resilience to utility-side disturbances, and (iv) elimination of the need for frequency, phase, and reactive power controllers. Hence, the DC microgrid is becoming a popular solution for many applications such as data centers, telecommunication stations, shipboard systems, EV charging stations, smart homes, commercial buildings, and renewable energy parks.

A practical DC microgrid requires effective control and load shedding strategies to protect the integrity of the DC microgrid under disturbances. This thesis is focused on developing advanced control and load shedding strategies for integrity protection of the DC microgrid. The studies reported in this thesis include developing (i) a versatile DC bus signaling control strategy to achieve coordinated decentralized control of the DERs and loads in the DC microgrid without utilizing costly high-bandwidth communication systems, (ii) an improved mode-adaptive droop control strategy to enable desirable and reliable control mode switching by the DERs under various operating conditions, and (iii) adaptive non-communication based load shedding schemes to enable the DC microgrid to ride through the disturbances that cause large power deficit and voltage sags.

Dedication

To my wife.

Acknowledgements

I would like to express my sincere gratitude to my supervisors, Dr. Firouz Badrkhani Ajaei and Dr. Ken McIsaac for their excellent supervision, guidance, support, and continuous encouragement throughout the course of this thesis.

I would like to thank my Ph.D. examination committee members, Professor Varma, Professor Dounavis, Professor Abdolvand, and Professor Hooshyar, for their review of this thesis, discussions, and constructive comments.

I also acknowledge the generous financial support provided by Western University and NSERC to pursue this research work.

Contents

Abstract.....	i
Summary for Lay Audience.....	iii
Dedication.....	iv
Acknowledgments.....	v
List of Figures.....	x
List of Tables.....	xv
List of Appendices.....	xvi
List of Abbreviations.....	xvii
Nomenclature.....	xvii
1 Introduction.....	1
1.1 Background.....	1
1.2 Statement of the Problem.....	2
1.3 Literature Review.....	2
1.3.1 DC Microgrid Control Strategies.....	2
1.3.1.1 Communication-based Control Strategies.....	2
1.3.1.2 Non-Communication based Control Strategies.....	3
1.3.2 DC Microgrid Load Shedding Schemes.....	5
1.3.2.1 Communication-based Load Shedding Schemes.....	5
1.3.2.2 Non-Communication based Load Shedding Schemes.....	5
1.4 Thesis Objectives.....	6
1.5 Methodology.....	7
1.6 Study System.....	7
1.6.1 System Structure.....	7
1.6.2 System Configuration.....	9
1.6.3 DER Models.....	10
1.6.3.1 WT Model.....	10
1.6.3.2 PV Model.....	12
1.6.3.3 BESS Model.....	13
1.6.3.4 GTC Model.....	14
1.6.4 Load Models.....	15

1.6.5	Cable Models	17
1.7	Thesis Outline.....	17
2	DC Microgrid Control	18
2.1	Introduction	18
2.2	Conventional Droop Control	18
2.3	DC Bus Signaling Control.....	20
2.3.1	Operation States.....	21
2.3.1.1	State I ($V_{th2} < V < V_{th1}$)	21
2.3.1.2	State II ($V_{th3} < V < V_{th2}$).....	22
2.3.1.3	State III ($V_{th4} < V < V_{th3}$).....	22
2.3.1.4	State IV ($V_{th5} < V < V_{th4}$)	22
2.3.1.5	State V ($V_{th6} < V < V_{th5}$).....	23
2.3.2	Voltage Thresholds	23
2.3.3	Control of the DERs and the GTC.....	23
2.3.3.1	WT Control	24
2.3.3.2	PV Control	24
2.3.3.3	BESS Control.....	25
2.3.3.4	GTC Control	25
2.3.4	Performance Evaluation.....	26
2.3.4.1	Case Study 1	26
2.3.4.2	Case Study 2	28
2.3.4.3	Case Study 3	28
2.3.4.4	Case Study 4	31
2.3.4.5	Case Study 5	37
2.4	Mode Adaptive Droop Control.....	40
2.4.1	Conventional MADC Strategy.....	40
2.4.2	Improved MADC Strategy.....	41
2.4.2.1	Adaptive Mode Switching Algorithm.....	41
2.4.2.2	DER Control Systems	45
2.4.2.2.1	WT Control	45
2.4.2.2.2	PV Control	45
2.4.2.2.3	BESS Control.....	45
2.4.3	Performance Evaluation.....	45
2.4.3.1	Case Study 1	47

2.4.3.2	Case Study 2.....	51
2.4.3.3	Case Study 3.....	54
2.4.3.4	Case Study 4.....	57
2.4.3.5	Case Study 5.....	61
2.5	Conclusions	65
3	Existing Load Shedding Schemes.....	66
3.1	Introduction	66
3.1.1	Voltage-based Load Shedding Scheme	66
3.1.2	Timer-based Load Shedding Scheme	66
3.1.3	Combined Load Shedding Scheme	67
3.2	Performance Evaluation.....	68
3.2.1	Case Study 1	71
3.2.1.1	Voltage-based Load Shedding Scheme.....	72
3.2.1.2	Timer-based Load Shedding Scheme.....	74
3.2.1.3	Combined Load Shedding Scheme	76
3.2.2	Case Study 2	78
3.2.2.1	Voltage-based Load Shedding Scheme.....	78
3.2.2.2	Timer-based Load Shedding Scheme.....	80
3.2.2.3	Combined Load Shedding Scheme	82
3.3	Conclusions	83
4	Proposed Load Shedding Schemes.....	84
4.1	Introduction	84
4.2	Adaptive Voltage-based Load Shedding Scheme.....	84
4.2.1	Introduction.....	84
4.2.2	Performance Evaluation.....	87
4.2.2.1	Case Study 1: Large Disturbance.....	88
4.2.2.1.1	Conventional Voltage-based Load Shedding Scheme	89
4.2.2.1.2	Adaptive Voltage-based Load Shedding Scheme	89
4.2.2.2	Case Study 2: Small Disturbance.....	92
4.2.2.2.1	Conventional Voltage-based Load Shedding Scheme	92
4.2.2.2.2	Adaptive Voltage-based Load Shedding Scheme	95
4.2.2.3	Case Study 3: Islanding.....	95
4.2.2.3.1	Conventional Voltage-based Load Shedding Scheme	95

4.2.2.3.2	Adaptive Voltage-based Load Shedding Scheme	98
4.3	Adaptive Timer-based Load Shedding Scheme	98
4.3.1	Introduction.....	98
4.3.2	Performance Evaluation.....	101
4.3.2.1	Case Study 1: Large Disturbance.....	102
4.3.2.1.1	Conventional Timer-based Load Shedding Scheme	102
4.3.2.1.2	Adaptive Timer-based Load Shedding Scheme	104
4.3.2.2	Case Study 2: Islanding.....	106
4.3.2.2.1	Conventional Timer-based Load Shedding Scheme	108
4.3.2.2.2	Adaptive Timer-based Load Shedding Scheme	110
4.4	Conclusions	113
5	Conclusions, Contributions, and Future Work	115
5.1	Summary.....	115
5.2	Conclusions	115
5.3	Contributions	117
5.4	Future Work.....	118
	Appendix A: Study System Parameters	119
	References.....	123
	Curriculum Vitae	133

List of Figures

1.1: Single-line diagram of the LVDC microgrid.	8
1.2: DC microgrid configuration (a) Unipolar, (b) Bipolar.	9
1.3: DC microgrid TN-S grounding systems.	10
1.4: PMSG-based WT connected to the DC microgrid.	11
1.5: The PMSG model in the $d-q$ reference frame.	11
1.6: PV system connected to the DC microgrid.	12
1.7: Single-diode circuit model of the PV.	12
1.8: BESS connected to the DC microgrid.	13
1.9: Equivalent circuit model of the battery.	13
1.10: GTC connected to the AC grid.	15
1.11: GTC model in the $d-q$ reference frame.	15
1.12: Underground cable configuration.	17
2.1: Voltage-current characteristic of a droop controlled DER.	19
2.2: Simplified model of a DC microgrid with two droop-controlled converters.	19
2.3: Proposed DBS operation states: (a) GTC, (b) BESS, (c) RES, (d) load.	22
2.4: Control block diagram of the PMSG-type WT.	24
2.5: Control block diagram of the PV.	24
2.6: Control block diagram of the BESS.	25
2.7: Control block diagram of the GTC.	25
2.8: Performance of the proposed DBS control strategy in the <i>Case Study 1</i> : (a) DER terminal voltages, (b) WT and PVs powers, (c) BESSs powers, (d) GTC and load powers.	27
2.9: Performance of the proposed DBS control strategy in the <i>Case Study 2</i> : (a) DER terminal voltages, (b) WT and PVs powers, (c) BESSs powers, (d) GTC and load powers.	29

2.10: Performance of the proposed DBS control strategy in the <i>Case Study 3</i> : (a) DER terminal voltages, (b) WT and PVs powers, (c) BESSs powers, (d) GTC and load powers.....	30
2.11: Performance of the proposed DBS control strategy with $2V_{th}$ in the <i>Case Study 3</i> : (a) DER terminal voltages, (b) WT and PVs powers, (c) BESSs powers, (d) GTC and load powers.	32
2.12: Performance of the proposed DBS control strategy with $V_{th}/2$ in the <i>Case Study 3</i> : (a) DER terminal voltages, (b) WT and PVs powers, (c) BESSs powers, (d) GTC and load powers.	33
2.13: Performance of the proposed DBS control strategy in the <i>Case Study 4</i> : (a) DER terminal voltages, (b) WT and PVs powers, (c) BESSs powers, (d) GTC and load powers.....	35
2.14: Performance of the conventional droop control strategy in the <i>Case Study 4</i> : (a) DER terminal voltages, (b) WT and PVs powers, (c) BESSs powers, (d) GTC and load powers.	36
2.15: Performance of the proposed DBS control strategy in the <i>Case Study 5</i> : (a) DER terminal voltages, (b) WT and PVs powers, (c) BESSs powers, (d) GTC and load powers.....	38
2.16: Performance of the conventional droop control strategy in the <i>Case Study 5</i> : (a) DER terminal voltages, (b) WT and PVs powers, (c) BESSs powers, (d) GTC and load powers.	39
2.17: Mode switching characteristics of the conventional MADC strategy.	41
2.18: Variations of the adaptive time delay with respect to the ROCOV.	43
2.19: Mode switching characteristics of the improved MADC strategy.....	43
2.20: $V-I$ characteristics of the mode-adaptive droop controlled DERs, (a) BESS, and (b) RES. .	44
2.21: Block diagram of the adaptive mode switching algorithm.	44
2.22: Control block diagram of the PMSG-type WT.....	46
2.23: Control block diagram of the PV.....	46
2.24: Control block diagram of the BESS.....	46
2.25: Performance of the conventional MADC strategy in the <i>Case Study 1</i> : (a) DER terminal voltages, (b) RES powers, (c) BESS powers.	48
2.26: Performance of the improved MADC strategy in the <i>Case Study 1</i> : (a) DER terminal voltages, (b) RES powers, (c) BESS powers.	49
2.27: Performance of the conventional MADC strategy in the <i>Case Study 2</i> : (a) DER terminal voltages, (b) RES powers, (c) BESS powers.	52

2.28: Performance of the improved MADC strategy in the <i>Case Study 2</i> : (a) DER terminal voltages, (b) RES powers, (c) BESS powers.	53
2.29: Performance of the conventional MADC strategy in the <i>Case Study 3</i> : (a) DER terminal voltages, (b) RES powers, (c) BESS powers.	55
2.30: Performance of the improved MADC strategy in the <i>Case Study 3</i> : (a) DER terminal voltages, (b) RES powers, (c) BESS powers.	56
2.31: Performance of the conventional MADC strategy in the <i>Case Study 4</i> : (a) DER bus voltages, (b) RES powers, (c) BESS powers, (d) WT operation mode, (e) PV1 operation mode, (f) PV2 operation mode, (g) BESS1 operation mode, (h) BESS2 operation mode.	58
2.32: Performance of the improved MADC strategy in the <i>Case Study 4</i> : (a) DER bus voltages, (b) RES powers, (c) BESS powers, (d) WT operation mode, (e) PV1 operation mode, (f) PV2 operation mode, (g) BESS1 operation mode, (h) BESS2 operation mode.	59
2.33: Performance of the DBS control strategy in <i>Case Study 5</i> : (a) DER bus voltages, (b) RES powers, (c) BESS powers, (d) GTC and load powers.....	63
2.34: Performance of the proposed MADC strategy in <i>Case Study 5</i> : (a) DER bus voltages, (b) RES powers, (c) BESS powers, (d) GTC and load powers.	64
3.1: The voltage-based load shedding scheme: (a) flowchart, (b) block diagram, (c) operating characteristic.	67
3.2: The timer-based load shedding scheme: (a) flowchart, (b) block diagram, (c) operating characteristic.	68
3.3: The combined load shedding scheme: (a) flowchart, (b) block diagram, (c) operating characteristic.	69
3.4: Single-line diagram of the study system.	70
3.5: Performance of the voltage-based load shedding scheme with high thresholds in the <i>Case Study 1</i> : (a) DC voltages, (b) total load power.....	73
3.6: Performance of the voltage-based load shedding scheme with low thresholds in the <i>Case Study 1</i> : (a) DC voltages, (b) total load power.....	74
3.7: Performance of the timer-based load shedding scheme with short delays in the <i>Case Study 1</i> : (a) DC voltages, (b) total load power.....	75

3.8: Performance of the timer-based load shedding scheme with long delays in the <i>Case Study 1</i> : (a) DC voltages, (b) total load power.....	76
3.9: Performance of the combined load shedding scheme in the <i>Case Study 1</i> : (a) DC voltages, (b) total load power.	77
3.10: Performance of the voltage-based load shedding scheme with high thresholds in the <i>Case Study 2</i> : (a) DC voltages, (b) total load power.....	78
3.11: Performance of the voltage-based load shedding scheme with low thresholds in the <i>Case Study 2</i> : (a) DC voltages, (b) total load power.....	79
3.12: Performance of the timer-based load shedding scheme with short delays in the <i>Case Study 2</i> : (a) DC voltages, (b) total load power.....	80
3.13: Performance of the timer-based load shedding scheme with long delays in the <i>Case Study 2</i> : (a) DC voltages, (b) total load power.....	81
3.14: Performance of the combined load shedding scheme in the <i>Case Study 2</i> : (a) DC voltages, (b) total load power.....	82
4.1: Adaptive voltage threshold that depends on the ROCOV.	85
4.2: Flowchart of the adaptive voltage-based load shedding scheme.	86
4.3: Block diagram of the adaptive voltage-based load shedding scheme.....	86
4.4: Operating characteristics of (a) the conventional load shedding scheme, (b) proposed adaptive load shedding scheme.....	87
4.5: Performance of the conventional voltage-based load shedding scheme in the <i>Case Study 1</i> : (a) DC voltages, (b) ROCOV, (c) total load power.	90
4.6: Performance of the adaptive voltage-based load shedding scheme in the <i>Case Study 1</i> : (a) DC voltages, (b) ROCOV, (c) total load power.	91
4.7: Performance of the conventional voltage-based load shedding scheme in the <i>Case Study 2</i> : (a) DC voltages, (b) ROCOV, (c) total load power.	93
4.8: Performance of the adaptive voltage-based load shedding scheme in the <i>Case Study 2</i> : (a) DC voltages, (b) ROCOV, (c) total load power.	94
4.9: Performance of the conventional voltage-based load shedding scheme in the <i>Case Study 3</i> : (a) DC voltages, (b) ROCOV, (c) total load power.	96

4.10: Performance of the adaptive voltage-based load shedding scheme in the <i>Case Study 3</i> : (a) DC voltages, (b) ROCOV, (c) total load power.....	97
4.11: Adaptive time delay that depends on the ROCOV.....	99
4.12: Flowchart of the adaptive timer-based load shedding scheme.	100
4.13: Block diagram of the adaptive timer-based load shedding scheme.....	101
4.14: Operating characteristics of different load shedding schemes: (a) conventional scheme with short delays, (b) conventional scheme with long delays, (c) adaptive scheme.....	101
4.15: Performance of the conventional timer-based load shedding scheme with short delays, in the <i>Case Study 1</i> : (a) bus voltages, (b) total power demand of the loads.	103
4.16: Performance of the conventional timer-based load shedding scheme with long delays, in the <i>Case Study 1</i> : (a) bus voltages, (b) total power demand of the loads.	104
4.17: Performance of the adaptive timer-based load shedding scheme in the <i>Case Study 1</i> : (a) bus voltages, (b) ROCOV at the load-side terminal of CB1, (c) ROCOV at the load-side terminal of CB2, (d) ROCOV at the load-side terminal of CB3 (e) total power demand of the loads.....	105
4.18: Adaptive time-delay characteristics (solid red line) and the operating point trajectory (dotted blue line) of the load shedding algorithms utilized to trip (a) CB1, (b) CB2, and (c) CB3, in the <i>Case Study 1</i>	107
4.19: Performance of the conventional timer-based load shedding scheme with short delays, in the <i>Case Study 2</i> : (a) bus voltages, (b) total power demand of the loads.	108
4.20: Performance of the conventional timer-based load shedding scheme with long delays, in the <i>Case Study 2</i> : (a) bus voltages, (b) total power demand of the loads.	109
4.21: Performance of the adaptive timer-based load shedding scheme in the <i>Case Study 2</i> : (a) bus voltages, (b) ROCOV at the load-side terminal of CB1, (c) ROCOV at the load-side terminal of CB2, (d) ROCOV at the load-side terminal of CB3 (e) total power demand of the loads.....	111
4.22: Adaptive time-delay characteristics (solid red line) and the operating point trajectory (dotted blue line) of the load shedding algorithms utilized to trip (a) CB1, (b) CB2, and (c) CB3, in the <i>Case Study 2</i>	112

List of Tables

2.1: Proposed DBS operation states.....	21
2.2: Comparison of the conventional and improved MADC strategies.....	61
3.1: Comparison of the non-communication based load shedding schemes.....	83
4.1: Comparison of the conventional and adaptive load shedding schemes.....	113
A.1: Parameters of the DC Microgrid.....	119
A.2: DC Microgrid Load Data.....	120
A.3: Cable Lengths and Types.....	121
A.4: Underground Cable Parameters Per-Unit Length.....	122
A.5: Underground Cable Dimensions.....	122
A.6: Parameters of the PI Controllers [p.u.].....	122

List of Appendices

Appendix A: Study System Parameters.....119

List of Abbreviations

AC	Alternating Current
BESS	Battery Energy Storage System
CB	Circuit Breaker
CCL	Constant Current Load
CPL	Constant Power Load
CRL	Constant Resistance Load
DBS	DC Bus Signaling
DC	Direct Current
DER	Distributed Energy Resource
ESS	Energy Storage System
EV	Electric Vehicles
GTC	Grid Tie Converter
LV	Low Voltage
LVDC	Low Voltage Direct Current
MADC	Mode Adaptive Droop Control
MPPT	Maximum Power Point Tracking
PMSG	Permanent Magnet Synchronous Generator
PV	Photovoltaic
RES	Renewable Energy System
ROCOF	Rate of Change of Frequency
ROCOV	Rate of Change of Voltage
SOC	State of Charge
VSC	Voltage-Sourced Converter
WT	Wind Turbines

Nomenclature

P_t	WT mechanical power
ρ	Air density
R_b	Radius of blades
v_w	Wind speed
C_p	Power conversion coefficient
λ	Tip speed ratio
β	Pitch angle
T_t	WT mechanical torque
ω_t	WT angular speed
V_{sd}	d -axis stator voltage
V_{sq}	q -axis stator voltage
I_{sd}	d -axis stator current
I_{sq}	q -axis stator current
I_s	Stator current
Ψ_{sd}	d -axis stator flux
Ψ_{sq}	q -axis stator flux
Ψ_f	Field flux
R_s	Stator resistance
L_{sd}	d -axis stator inductance
L_{sq}	q -axis stator inductance
ω_s	Synchronous angular speed
T_{em}	Electromagnetic torque
H_g	Generator inertia constant
H_t	Turbine inertia constant
ω_r	Rotor angular speed
V_{pv}	PV voltage
I_{pv}	PV current
I_g	PV full-load current
I_d	PV diode current
I_0	PV reverse saturation current
q	PV charge carrier

k	PV boltzman constant
T	PV cell temperature
n	PV ideality factor
N_p	Number of parallel PV cells/modules
N_s	Number of series PV cells/modules
V_{batt}	Battery voltage
I_{batt}	Battery current
R_{batt}	Battery resistance
E_g	Battery no-load voltage
E_{g0}	Battery constant voltage
Q	Battery capacity
A	Battery exponential zone amplitude
B	Battery exponential zone time constant inverse
V_{td}	d -axis GTC voltage
V_{tq}	q -axis GTC voltage
I_{td}	d -axis GTC current
I_{tq}	q -axis GTC current
L_t	GTC output inductance
R_t	GTC output resistance
A_{CRL}	CRL coefficient
A_{CCL}	CCL coefficient
A_{CPL}	CPL coefficient
I_{CRL}	CRL current
I_{CCL}	CCL current
I_{CPL}	CPL current
P_{CRL}	CRL power
P_{CCL}	CCL power
P_{CPL}	CPL power
V_{load}	Load voltage
I_{load}	Load current
R_{load}	Load resistance
V	Voltage
V_n	Nominal voltage
V_{dc}^*	Voltage reference

V_{thi}	i^{th} voltage threshold
V_{dci}	i^{th} DER output voltage
I_{dci}	i^{th} DER output current
R_{di}	i^{th} DER virtual resistance
R_{linei}	i^{th} Line resistance
K	Droop gain
P_{RES}	RESs total active power
P_{BESS}	BESSs total active power
P_{load}	Loads total power
P_{GTC}	GTC active power
Q_{GTC}	GTC reactive power
P_{PMSG}	PMSG active power
Q_{PMSG}	PMSG reactive power
T_{delay}	Adaptive time delay
T_{max}	Maximum time delay
T_{min}	Minimum time delay
V_{max}	Maximum voltage threshold
V_{min}	Minimum voltage threshold
V_f	Filtered voltage
Δt	Difference step
C_{dc}	DC capacitance
f_{sw}	Switching frequency
S_{GTC}	GTC apparent power
V_{rated}	Rated voltage
f_{rated}	Rated frequency
$R_{f-series}$	Series filter resistance
$L_{f-series}$	Series filter inductance
$R_{f-parallel}$	Parallel filter resistance
$C_{f-parallel}$	Parallel filter capacitance
S_{PMSG}	PMSG apparent power
S_{VSC}	VSC apparent power
P_{WT}	WT Power
X_d	d -axis reactance

X_q	q -axis reactance
X_l	Leakage reactance
L_{in}	Input inductance
C_{in}	Input capacitance

Chapter 1

1 Introduction

1.1 Background

The microgrid is an emerging technology that facilitates the integration of distributed energy resources (DERs) in power distribution networks, reduces the energy losses, and improves the quality and reliability of the electrical energy supplied to the consumers [1]-[4]. In the recent years, the DC microgrid has attracted great attention compared to the alternating current (AC) microgrid [5]-[7]. The reason is that the majority of the DERs, e.g., photovoltaics (PVs), fuel cells, and battery energy storage systems (BESSs), provide DC power, and an increasing portion of the emerging loads require DC power, e.g., electric vehicles (EVs), consumer electronics, and LED lighting systems [5]-[7]. The DC microgrid offers significant potential advantages over its AC counterpart. These advantages include (i) lower investment cost and power conversion losses due to elimination of unnecessary AC/DC converters, (ii) lower cable losses due to absence of skin effect, (iii) higher reliability and resilience to utility-side disturbances, and (iv) elimination of the need for frequency, phase, and reactive power controllers [5]-[7]. Hence, the DC microgrid is becoming a popular solution for many applications such as data centers, telecommunication stations, shipboard systems, EV charging stations, smart homes, commercial buildings, and renewable energy parks [8].

A practical DC microgrid requires an effective control strategy to regulate the DC bus voltages, enable power sharing among the DERs, and provide acceptable dynamic response to disturbances [9]-[13]. Furthermore, when the power demand of the loads is higher than the power generation of the DERs in the DC microgrid, the power balance cannot be maintained by control actions and the DERs fail to regulate the DC bus voltages. Under such conditions, it is necessary to shed some of the non-critical loads in order to protect the integrity of the DC microgrid [14]-[17]. Thus, the DC microgrid also requires an effective load shedding scheme to (i) maintain the power balance in the DC microgrid

through fast and coordinated shedding of the non-critical loads, (ii) prevent the bus voltages in the microgrid from falling below predetermined lower limits, (iii) ensure that the critical loads do not experience excessive steady-state voltage deviations, (iv) minimize the magnitudes and durations of the voltage sags caused by sudden disturbances, and (v) increase the reliability of the power supplied to the critical loads [14]-[17].

1.2 Statement of the Problem

The existing communication-based control and load shedding strategies are costly, suffer from vulnerability to communication failure, and degrade the DC microgrid reliability, flexibility, modularity, and expandability. The non-communication based control strategies suffer from disadvantages such as load-dependent voltage deviations, poor power-sharing accuracy, poor dynamic response to disturbances, and circulating current between the DERs [9]-[13]. Moreover, the existing non-communication based load shedding schemes necessitate a compromise between the voltage regulation performance and the power supply reliability [14]-[17].

1.3 Literature Review

This section highlights the shortcomings of the existing DC microgrid control and load shedding strategies.

1.3.1 DC Microgrid Control Strategies

The DC microgrid control strategies which have been proposed in the literature can be classified into the communication-based [18]-[29] and non-communication based [30]-[53] categories.

1.3.1.1 Communication-based Control Strategies

The communication-based control strategies include the (i) centralized [18], [19], (ii) master-slave [20], (iii) circular chain [21], (iv) distributed [22]-[26], and (v) hierarchical [27]-[29], control strategies. In the centralized control strategy, a microgrid central controller processes the data received from the DERs and sends commands to them via communication links in order to maintain the power balance and regulate the DC bus

voltages [18], [19]. In the master-slave control, the DC voltage is regulated by a DER with a high power rating, i.e., the master unit, and the other DERs, i.e., the slaves, are controlled by either the master or other slaves [20]. In the circular chain control strategy, the current reference of each DER is taken from the other DER, and the current reference of the first DER is obtained from that of the last DER to form a control ring [21]. In the distributed control, the adjacent DERs communicate with each other to improve the overall performance of the DC microgrid [22]-[26]. The hierarchical control strategy consists of the centralized secondary and tertiary control levels and a decentralized primary control level [27]-[29].

The communication-based control strategies result in desirable power-sharing and voltage regulation performances. However, they require communication systems that are costly, vulnerable to failure, and degrade the system reliability, flexibility, modularity, and expandability [9]-[13]. Therefore, the application of the communication-based control strategies in large DC microgrids with multiple geographically dispersed DERs is often avoided [9]-[13].

1.3.1.2 Non-Communication based Control Strategies

The control strategies in the non-communication based category enable autonomous power sharing among different DERs using locally measured DC bus voltages. They offer advantages such as simple implementation and low cost, as well as high reliability, flexibility, modularity, and expandability [9]-[13]. Therefore, these control strategies are more suitable for application in DC microgrids that include multiple geographically dispersed DERs [9]-[13]. The non-communication based category includes the conventional droop [30]-[32], improved droop [33]-[36], DC bus signaling (DBS) [37]-[47], and mode adaptive droop control (MADC) [48]-[53] strategies.

A conventional droop-controlled DER utilizes a fixed droop gain for the entire range of its DC-terminal voltage. Thus, the values of the droop gains significantly affect the microgrid stability, its voltage regulation performance, and the accuracy of power sharing among the DERs that are responsible for the DC voltage regulation. A small gain results in more accurate voltage regulation and less accurate power sharing among the DERs, and

vice versa [30]-[32]. To resolve these issues, a variety of improved droop control strategies have been proposed. The nonlinear droop characteristic of [33] improves the power sharing and voltage regulation performances, but adds complexity and nonlinearity to the control system. The adaptive droop control strategy of [34]-[36] reduces the circulating currents and the power sharing mismatch among the DERs, but requires knowledge of the line parameters, and also becomes excessively complex as the number of DERs increases.

The DBS and MADC strategies offer considerable performance improvement by using control characteristics that adapt to the microgrid operating conditions. Both of these control strategies operate using locally measured bus voltages. The DBS control strategy [37]-[47] utilizes multiple predefined DC voltage ranges to determine the operation modes of the DERs and the grid tie converter (GTC). The operation mode of each component changes instantaneously whenever the corresponding bus voltage enters any of the aforementioned ranges. Most of the DBS control strategies, [37]-[41], have been investigated and verified under a specific operation mode of the DC microgrid, and therefore may not be applicable to both grid-connected and islanded modes. Some of the DBS control strategies perform DC voltage regulation using either the GTC [38], [39], or the BESSs [40], [41], which necessitates high-rated GTC or BESSs to manage large power imbalances. Another strategy is to use the GTC as the main controller and the renewable energy resources (RESs) and BESSs as auxiliary controllers for DC bus voltage regulation in the grid-connected microgrid [42]-[44]. This strategy requires lower-rated GTC and BESSs, but unnecessarily curtails renewable power generation instead of storing the extra power in the BESSs [42].

The MADC strategy utilizes a hysteresis characteristic to switch between voltage control by the RESs and the BESSs in the islanded microgrid, depending on the bus voltage variations [48]-[53]. The conventional MADC strategy is designed based on the assumption that all DERs measure equal bus voltages, neglecting the voltage drops caused by the line resistances. This is not always a valid assumption. Thus, the conventional MADC strategy may fail to provide acceptable coordination between the voltage controlling components in the islanded DC microgrid. This issue degrades the power sharing and voltage regulation in the DC microgrid.

1.3.2 DC Microgrid Load Shedding Schemes

The existing DC microgrid load shedding schemes could be classified into the communication-based [54]-[69] and non-communication-based [32], [42], [43], [44], [51], [70]-[73] categories.

1.3.2.1 Communication-based Load Shedding Schemes

The communication-based load shedding schemes [54]-[69] are able to receive and process large amounts of data pertaining to the state of the microgrid and shed optimal amounts of loads, in the correct order, in a timely manner. However, these load shedding schemes are complex, costly, and vulnerable to communication failure. They also suffer from low flexibility, modularity, and expandability [14], [15]. Due to the aforementioned disadvantages, communication-based load shedding schemes are more suitable for applications in small-scale DC microgrids with fixed and compact configurations.

1.3.2.2 Non-Communication based Load Shedding Schemes

The non-communication based load shedding schemes operate based on locally-measured bus voltages [32], [42], [43], [44], [51], [70]-[73]. They offer advantages such as simple implementation, low cost, robustness against single point of failure, and high flexibility, scalability, and expandability [14], [15]. Therefore, these schemes are suitable for a broader range of DC microgrids including those with geographically dispersed loads that do not have access to communication signals. The non-communication based load shedding schemes that have been proposed in the literature for DC microgrid applications include voltage-based [32], [43], [70]-[72], timer-based [42], and combined [44], [51], [73] schemes.

The voltage-based load shedding scheme [32], [43], [70]-[72] utilizes different voltage thresholds to prioritize non-critical loads and instantaneously sheds a load whenever the voltage seen by that load falls below the corresponding voltage threshold. The voltage-based scheme may cause unnecessary load shedding, i.e., over-shedding, when the voltage thresholds are too close to each other. It also causes large steady-state voltage deviations, i.e., does not shed sufficient amount of loads, when the difference between the voltage

thresholds is large. Hence, application of the voltage-based load shedding scheme necessitates a compromise between the power supply reliability and the voltage regulation performance.

The timer-based load shedding scheme [42] utilizes a common voltage threshold and prioritizes the non-critical loads using different time delays. This strategy sheds a load whenever its voltage remains below the common threshold for a time period longer than the corresponding time delay. This scheme may cause over-shedding of loads when short delays are used. This scheme may also cause large voltage sags when large delays are used. Hence, similar to the voltage-based scheme, application of the timer-based scheme necessitates a compromise between the power supply reliability and the voltage regulation performance.

The combined load shedding scheme [44], [51], [73] utilizes both voltage-based and timer-based algorithms and thus operates whenever either of these two schemes operate. A combined scheme with appropriately set voltage thresholds and time delays can alleviate the voltage sag problem caused by delayed or missed operation of the voltage- and timer-based schemes. However, the combined scheme is more likely to cause unnecessary load shedding as compared with both of the voltage- and timer-based schemes, and thus adversely affects the power supply reliability.

The existing non-communication based load shedding schemes utilize fixed voltage/time thresholds, and thus, either cause excessive bus voltage deviations or cause over-shedding of loads.

1.4 Thesis Objectives

The main objective of this Ph.D. thesis research is to develop advanced control and load shedding strategies to protect the integrity of the DC microgrid under large disturbances, without relying on costly communication systems and centralized controllers that may compromise the system reliability. The proposed integrity protection schemes are expected to:

- effectively maintain the power balance in the DC microgrid under disturbances.
- enable desirable power sharing between the DERs.
- effectively regulate the DC bus voltages and prevent excessive voltage deviations under transient conditions and steady state.
- increase the power supply reliability by preventing unnecessary shedding of loads.

1.5 Methodology

In order to achieve the thesis objectives:

- An accurate model of a DC microgrid study system is developed for simulation studies.
- The behavior of the DC microgrid study system under various disturbances in both the grid-connected and islanded modes is investigated using time-domain simulation in the PSCAD/EMTDC software environment.
- The results of these studies are used to develop and validate advanced control and load shedding strategies that improve the stability and integrity of the DC microgrid.

1.6 Study System

1.6.1 System Structure

The low voltage direct current (LVDC) microgrid study system of Figure 1.1 [74]-[77], is developed by converting the IEEE 37-node AC test system [78] to DC and enabling it to operate as a microgrid. The operating DC voltage is chosen to be ± 750 V to comply with the guidelines of the IEC60038 standard for LVDC systems [79]. The ± 750 V DC microgrid includes a 1 MW permanent magnet synchronous generator (PMSG)-based wind turbine (WT) connected through an AC/DC voltage sourced converter (VSC) to the node 709, and two 0.5 MW PV generation systems connected through DC/DC boost converters to the nodes 712 and 722. Two 0.4 MW BESSs are connected through bidirectional buck-boost DC/DC converters to the nodes 705 and 707 in order to be as close as possible to the critical loads area. A 1 MW bidirectional DC/AC GTC interfaces the DC microgrid with the AC grid through a 0.75kV/4.8kV isolation transformer at the node 701. All converters are represented in detail using switching models. The ratings and parameters of the DERs are provided in the Appendix.

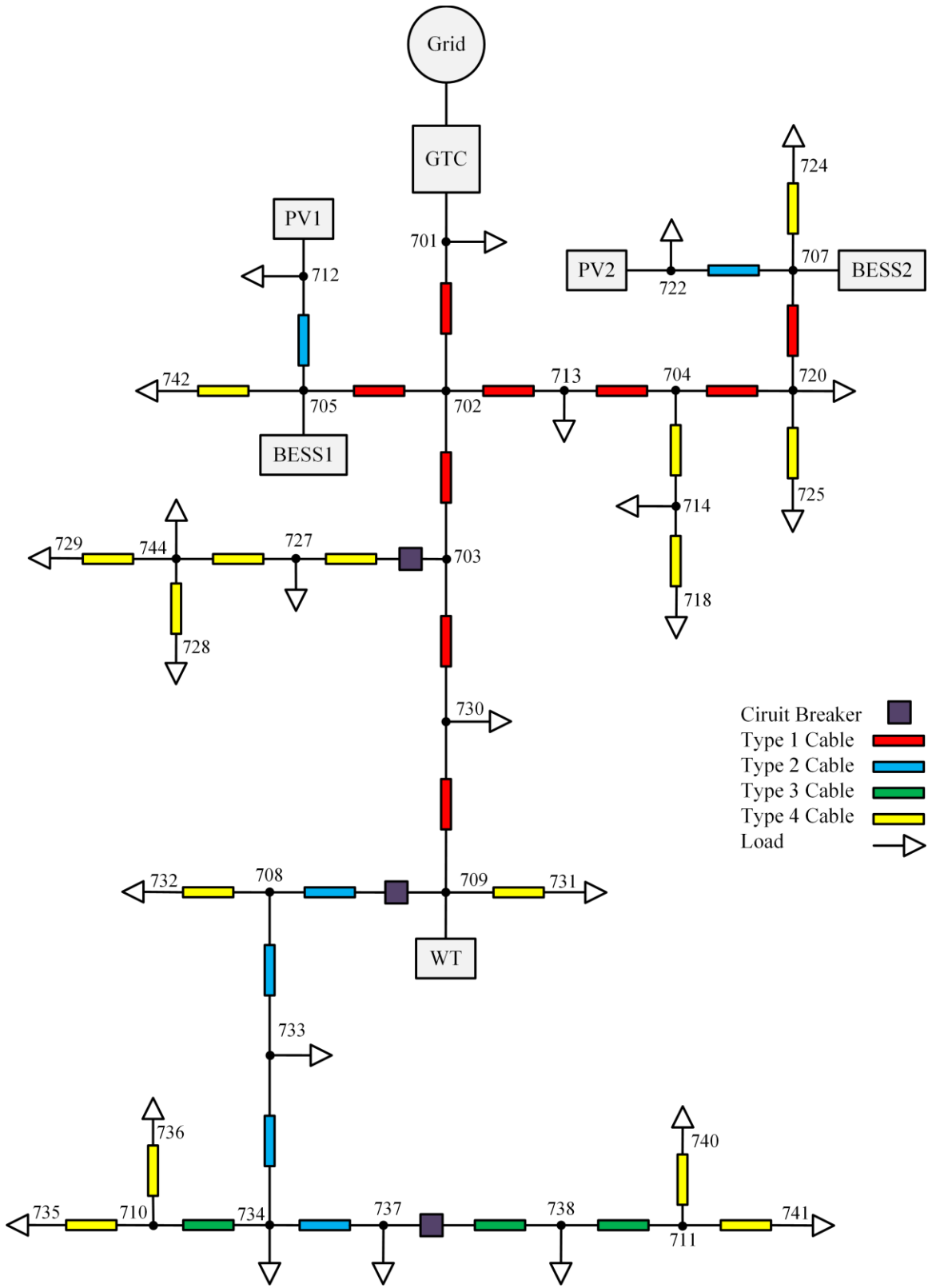


Figure 1.1: Single-line diagram of the LVDC microgrid.

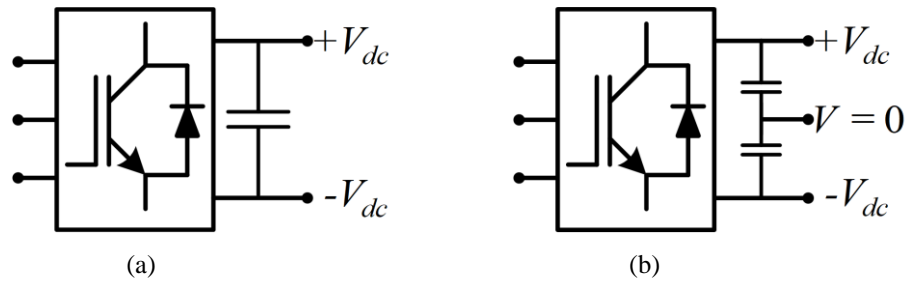


Figure 1.2: DC microgrid configuration (a) Unipolar, (b) Bipolar.

1.6.2 System Configuration

A DC microgrid can be either unipolar or bipolar as shown in Figures 1.2 (a) and (b) [6], [7], [80]. The unipolar configuration has a pair of positive and negative polarity conductors which provide a line-to-line voltage level of $2V_{dc}$. The unipolar configuration has advantages such as simple implementation and symmetry between the DC poles. However, it suffers from drawbacks such as lack of redundancy, lack of different voltage levels, and risk of complete system shutdown under a single fault [6], [7], [80].

The bipolar system could overcome the aforementioned drawbacks of the unipolar system. It has a pair of positive and negative poles and an additional neutral terminal, and thus provides three voltage levels $+V_{dc}$, $-V_{dc}$ and $2V_{dc}$ [6], [7], [80]. These different voltage levels enable interconnection of the DERs and loads with different voltage ratings. Moreover, the bipolar DC microgrid provides higher reliability, availability, and power quality under fault conditions. Thus, the bipolar configuration is selected for the studied DC microgrid [6], [7], [80].

The most commonly recommended grounding configuration for DC microgrids by the international standards is the TN-S [81], [82]. In this configuration, the converter middle point is connected to ground, and the body of the apparatus is connected to the neutral and protective earth as shown in Figure 1.3. The TN-S configuration is typically used to supply power to LVDC residential, commercial, and industrial loads [81], [82]. The DC microgrid study system utilizes the TN-S grounding configuration.

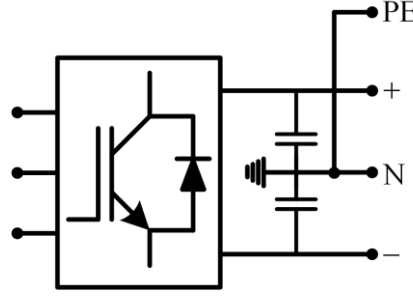


Figure 1.3: DC microgrid TN-S grounding systems.

1.6.3 DER Models

Detailed models of the DERs and the GTC are used in the study system. This section provides a brief description of the utilized models.

1.6.3.1 WT Model

The PMSG-based WT consists of rotor blades, gearbox and generator, and is connected to the DC microgrid through a VSC, as shown in Figure 1.4. The mechanical power extracted by the WT is [83]-[85]:

$$P_t = \frac{1}{2} \rho_{air} \pi R_b^2 v_w^3 C_p(\lambda, \beta) \quad (1.1)$$

where ρ_{air} is the air density, R_b is the radius of the blades, v_w is the wind speed, $C_p(\lambda, \beta)$ is the turbine power conversion coefficient, λ is the tip speed ratio, and β is the pitch angle. To extract maximum power from wind, the C_p should be kept at the maximum value (C_{p-max}), and the tip speed ratio is to be kept around the optimal value (λ_{opt}). The WT mechanical torque is [83]-[85]:

$$T_t = \frac{P_t}{\omega_t} \quad (1.2)$$

The generator is represented by the PMSG model of PSCAD, which is defined in the $d-q$ synchronous reference frame as shown in Figure 1.5. The stator voltage equations in the $d-q$ reference frame are [83]-[85]:

$$V_{sd} = R_s I_{sd} + L_{sd} \frac{dI_{sd}}{dt} - \omega_s L_{sq} I_{sq} \quad (1.3)$$

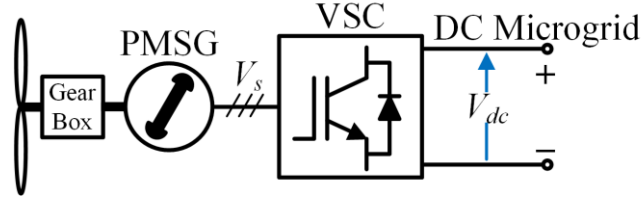
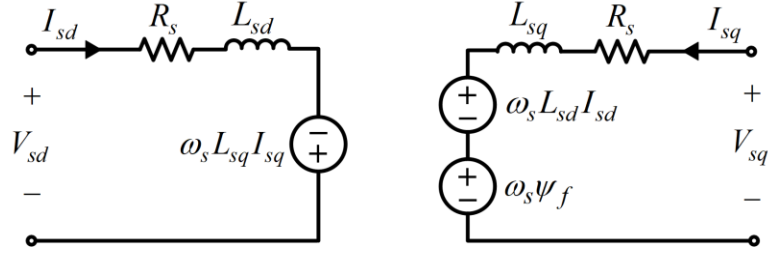


Figure 1.4: PMSG-based WT connected to the DC microgrid.

Figure 1.5: The PMSG model in the d - q reference frame.

$$V_{sq} = R_s I_{sq} + L_{sq} \frac{dI_{sq}}{dt} + \omega_s L_{sd} I_{sd} + \omega_s \psi_f \quad (1.4)$$

where V , I , Ψ , ω , R , and L represent voltage, current, flux, angular speed, resistance and inductance, respectively. Subscripts ‘ s ’, ‘ f ’, ‘ d ’ and ‘ q ’ represent the stator, field, d - and q -axis quantities, respectively. The PMSG active and reactive powers in the d - q reference frame are expressed as follows [83]-[85]:

$$P_{PMSG} = \frac{3}{2} \omega_s \psi_f I_{sq} \quad (1.5)$$

$$Q_{PMSG} = \frac{3}{2} \omega_s \left[L_{sd} |I_s|^2 + \psi_f I_{sd} \right] \quad (1.6)$$

From (1.5) and (1.6), the PMSG active and reactive powers are controlled through the q - and d -axis components of the stator currents, respectively. From (1.3) and (1.4), the d - and q -axis components of the stator current are controlled through the corresponding voltage components. The dynamic equation of the PMSG is [83]-[85]:

$$2H_g \frac{d\omega_r}{dt} = T_t - T_{em} \quad (1.7)$$

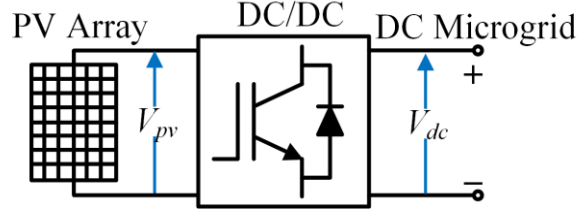


Figure 1.6: PV system connected to the DC microgrid.

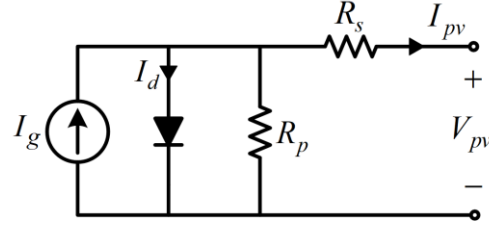


Figure 1.7: Single-diode circuit model of the PV.

where H_g , ω_r and T_{em} represent generator inertia constant, rotor angular speed, and electromagnetic torque, respectively.

1.6.3.2 PV Model

The PV generation system is connected to the DC microgrid through the DC/DC boost converter as shown in Figure 1.6. The PV cells are represented by the single-diode circuit model of PSCAD (Figure 1.7), which is the most commonly used PV model in the literature [39], [41], [51]. The circuit is composed of a current source, a diode, a series resistance R_s and a parallel resistance R_p . The basic equation describing the nonlinear current-voltage characteristics of the PV cell is [39], [41], [51]:

$$I_{pv} = I_g - I_d - \left(\frac{V_{pv} + R_s I_{pv}}{R_p} \right) \quad (1.8)$$

where

$$I_d = I_0 \left(\exp \left(\frac{q(V_{pv} + R_s I_{pv})}{nkT} \right) - 1 \right) \quad (1.9)$$

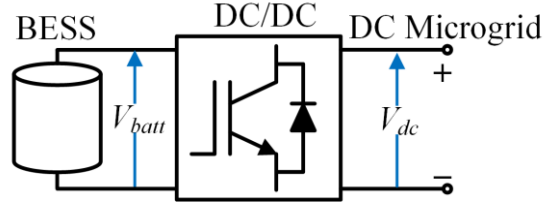


Figure 1.8: BESS connected to the DC microgrid.

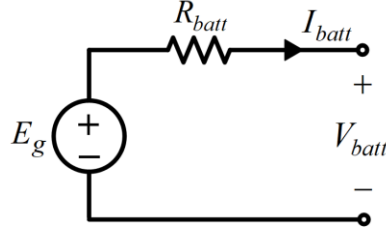


Figure 1.9: Equivalent circuit model of the battery.

and V_{pv} is the PV cell voltage, I_{pv} is the PV cell current, I_g is the full-load current, I_d is the diode current, I_0 is the reverse saturation current, q is the charge carrier, k is the Boltzman constant, T is the cell temperature, and n is the ideality factor [39], [41], [51]. To achieve the desired voltage and current levels, PV cells are connected in series (N_s) (for larger voltage) and in parallel (N_p) (for larger current) to form a PV module. Several modules are connected to each other to form a PV array [39], [41], [51].

1.6.3.3 BESS Model

The BESS is connected to the DC microgrid through a bidirectional buck-boost DC/DC converter as shown in Figure 1.8. The battery model of the PSCAD software is used (Figure 1.9), which includes a simple controlled voltage source in series with a constant resistance [39], [86]. The open voltage source is calculated with a non-linear equation based on the state-of-charge (SOC) of the battery. The controlled voltage source is described by the following equations [39], [86]:

$$V_{batt} = E_g - R_{batt} I_{batt} \quad (1.10)$$

$$E_g = E_{g0} - K \frac{Q}{Q - \int I_{batt} dt} + A \cdot \exp(B \int I_{batt} dt) \quad (1.11)$$

where V_{batt} is the battery voltage (V), E_g is the no-load voltage (V), R_{batt} is the battery resistance (Ω), I_{batt} is the battery current (A), E_{g0} is the battery constant voltage (V), K is the polarization voltage (V), Q is the battery capacity (Ah), $\int I_{batt}.dt$ is the actual battery charge (Ah), A is the exponential zone amplitude (V), B is the inverse of the exponential zone time constant (Ah)⁻¹. The state of charge of the battery is expressed as [39], [86]:

$$SOC = 100 \left(1 + \frac{\int I_{batt}.dt}{Q} \right) \quad (1.12)$$

The BESS must operate within a range of voltage and SOC set-values to protect its elements. If the SOC decreases or increases to its minimum or maximum set-values, the BESS converter stops switching and prevents the exceeding of its set-values [39], [86].

1.6.3.4 GTC Model

The GTC is connected to the AC grid through an output filter, and an interfacing transformer, as shown in Figure 1.10. The GTC model in the d - q synchronous reference frame is shown in Figure 1.11, where [87], [88]:

$$V_{td} = R_t I_{td} + L_t \frac{dI_{td}}{dt} - \omega_s L_t I_{tq} + V_{sd} \quad (1.13)$$

$$V_{tq} = R_t I_{tq} + L_t \frac{dI_{tq}}{dt} + \omega_s L_t I_{td} \quad (1.14)$$

and the subscripts ‘ s ’ and ‘ t ’ represents the AC system and GTC terminal quantities, respectively. The GTC active and reactive powers in the d - q reference frame are expressed as follows [87], [88]:

$$P_{GTC} = \frac{3}{2} V_{sd} I_{td} \quad (1.15)$$

$$Q_{GTC} = -\frac{3}{2} V_{sd} I_{tq} \quad (1.16)$$

From (1.15) and (1.16), the GTC active and reactive powers are controlled through the d - and q -axis components of its terminal currents, respectively. From (1.13) and (1.14), the d - and q -axis components of the GTC terminal current are controlled through the corresponding GTC terminal voltage components.

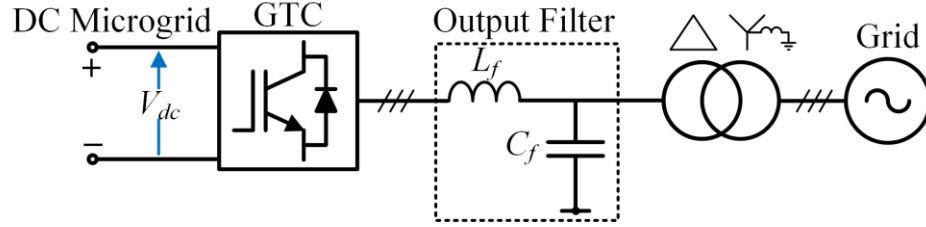
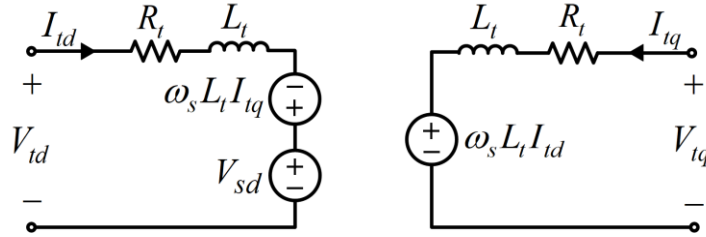


Figure 1.10: GTC connected to the AC grid.

Figure 1.11: GTC model in the d - q reference frame.

1.6.4 Load Models

The loads in the DC microgrid can be characterized as constant resistance load (CRL), constant current load (CCL), constant power load (CPL), or a combination of these [89]-[93]. Incandescent lamps, coffee makers, and electric stoves are classified as CRLs; LED lighting systems, BESS chargers and EV charge piles are classified as CCLs; electronic loads, power converters and electric motor drives are classified as CPLs [89]-[93]. Load characteristic in DC systems can be represented by the polynomial load model [89]-[93]. This model describes the relationship between the load power and voltage as follows:

$$P_{Load} = A_{CRL}V^2 + A_{CCL}V + A_{CPL} \quad (1.17)$$

where A_{CRL} is the CRL coefficient, A_{CCL} is the CCL coefficient and A_{CPL} is the CPL coefficient. The relationship between the current and voltage of the CRL is expressed as follows [89]-[91]:

$$I_{CRL} = \frac{V}{R_{CRL}} = \frac{P_{CRL}V}{V^2} \quad (1.18)$$

where I_{CRL} and V represent the current and voltage of the CRL while P_{CRL} and V_n represent the CRL power and nominal voltage. The current of the CRL increases/decreases when the voltage increases/decreases. The CRL is modeled in PSCAD software using the resistance R_{CRL} as follows [89]-[91]:

$$R_{CRL} = R_{Const} = \frac{V^2}{P_{CRL}} \quad (1.19)$$

The relationship between the current and voltage of the CCL is expressed as follows [89]-[91]:

$$I_{CCL} = I_{Const} = \frac{P_{CCL}}{V_n} \quad (1.20)$$

where I_{CCL} and P_{CCL} represent the current and power of the CCL power. The current of the CCL is constant regardless of the voltage variations. The CCL is modeled in PSCAD software using the resistance R_{CCL} as follows [89]-[91]:

$$R_{CCL} = \frac{V}{I_{CCL}} = \frac{V_n V}{P_{CCL}} \quad (1.21)$$

The relationship between the current and voltage of the CPL is expressed as follows [89]-[93]:

$$I_{CPL} = \frac{P_{CPL}}{V} \quad (1.22)$$

where I_{CPL} and P_{CPL} represent the current and power of the CPL power. The current of the CPL decreases/increases when the voltage increases/decreases. The CPL is modeled in PSCAD software using the resistance R_{CPL} as follows [89]-[91]:

$$R_{CPL} = \frac{V}{I_{CPL}} = \frac{V^2}{P_{CPL}} \quad (1.23)$$

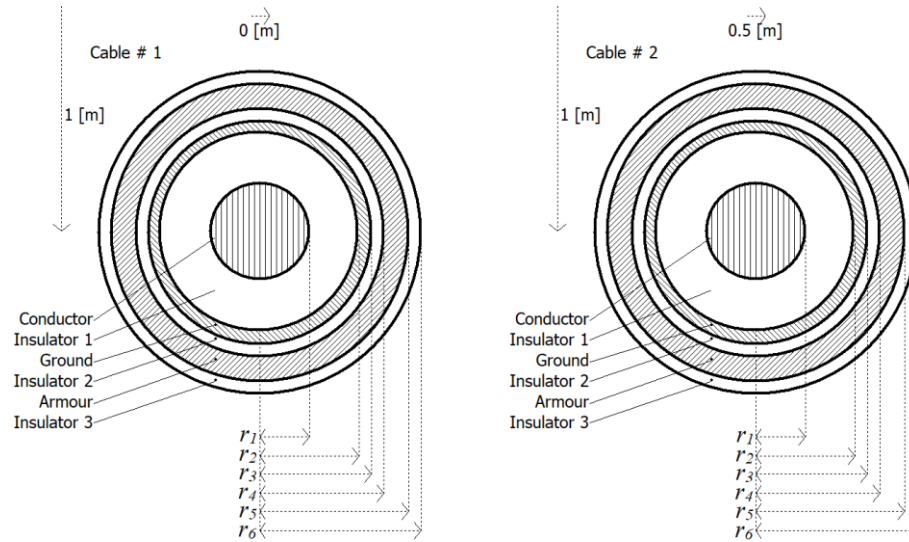


Figure 1.12: Underground cable configuration.

1.6.5 Cable Models

The cables are represented by the PI section model in the PSCAD software. Four different sizes of the 1 kV single-core XLPE cable [94] are used in the study system. The cable size in each feeder section is determined taking into account the load current, maximum allowable voltage drop, and maximum acceptable conduction loss. The positive and negative polarity underground cables are assumed to be buried 1 m deep, with a horizontal separation of 0.5 m. Figure 1.12 shows the general configuration of the underground cable, which applies to all four cable types. The cable length and type for each feeder section, and the per-unit-length parameters and dimensions of each cable type are given in the Appendix.

1.7 Thesis Outline

The next chapters of this thesis are organized as follows:

- Chapter 2 proposes improved DBS and MADC strategies for the DC microgrid.
- Chapter 3 investigates and compares the performances of the existing non-communication based load shedding schemes in the DC microgrid.
- Chapter 4 proposes adaptive voltage- and timer-based load shedding schemes for the DC microgrid.
- Chapter 5 summarizes the thesis contributions and provides concluding remarks.

Chapter 2

2 DC Microgrid Control

2.1 Introduction

This chapter is divided in two main topics. First, an improved DBS control strategy is proposed to achieve coordinated decentralized control of the DERs and loads in the DC microgrid without utilizing costly high-bandwidth communication systems. Subsequently, an improved MADC strategy is proposed for the DC microgrid to minimize the adverse effects of unequal bus voltages on the coordinated participation of the DERs in regulating bus voltages and maintaining the power balance in the DC microgrid. The performances of the proposed DBS and MADC strategies are investigated and verified under various operating conditions and disturbance scenarios in both grid-connected and islanded operation modes of the DC microgrid. The time-domain simulation studies are conducted on a detailed DC microgrid study system using the PSCAD/EMTDC software.

2.2 Conventional Droop Control

The conventional droop control strategy is briefly described in this section to highlight its shortcomings and also to enable comparing its performance with that of the proposed DBS control strategy in Section 2.4. In the grid-connected microgrid, the GTC operates in the constant voltage control mode and regulates the DC bus voltages. When the microgrid is islanded, the BESSs operate in the droop control mode and regulate their DC terminal voltages.

The output current of a converter operating based on the conventional droop control strategy is proportional to the deviation of the corresponding DC bus voltage from a reference value. This enables parallel operation of multiple DERs in the DC microgrid, without a need for communication systems. The voltage-current characteristic of a droop controlled DER is described by (2.1), where V_{dc}^* is the no-load voltage, i.e., the reference voltage, and V_{dci} , I_{dci} and R_{di} are the output voltage, the output current, and the virtual

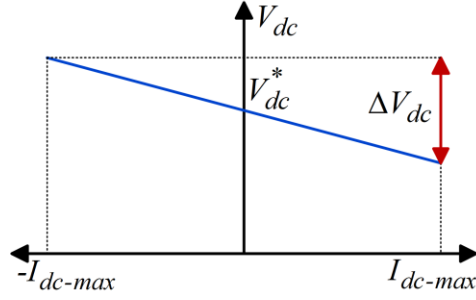


Figure 2.1: Voltage-current characteristic of a droop controlled DER.

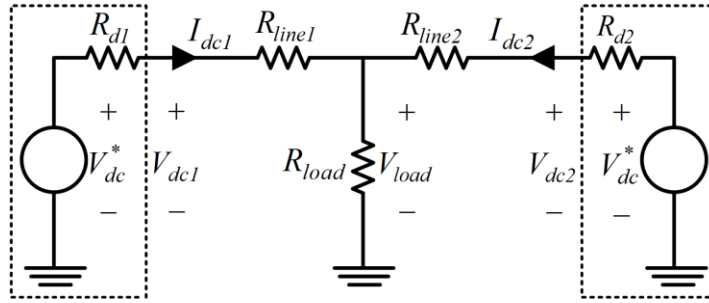


Figure 2.2: Simplified model of a DC microgrid with two droop-controlled converters.

resistance of the i^{th} DER, respectively. Figure 2.1 shows the droop characteristic of (2.1), where the slope of the voltage-current characteristic is the R_{di} [95], [96].

$$V_{dci} = V_{dc}^* - R_{di}I_{dci} \quad (2.1)$$

Figure 2.2 shows a simplified model of a DC microgrid with two DERs providing power to a load. Taking into account the line resistances R_{line1} and R_{line2} , the voltage-current characteristics of the DERs are as follows [95], [96]:

$$V_{load} = V_{dc}^* - R_{d1}I_{dc1} - R_{line1}I_{dc1} \quad (2.2)$$

$$V_{load} = V_{dc}^* - R_{d2}I_{dc2} - R_{line2}I_{dc2} \quad (2.3)$$

The relationship between the output currents of the DERs is described by (2.4). In practice, the line resistances are neither necessarily equal nor negligible. Hence, to achieve acceptable power sharing between the droop-controlled DERs in the simple DC microgrid of Figure 2.2, the virtual resistances should be determined such that (2.5) is satisfied.

However, (2.2) and (2.3) do not apply to realistic DC microgrids where there are multiple loads and also more than one DER may be connected to each line.

$$\frac{I_{dc1}}{I_{dc2}} = \frac{R_{d2} + R_{line2}}{R_{d1} + R_{line1}} \quad (2.4)$$

$$\frac{R_{d1}}{R_{d2}} = \frac{R_{line1}}{R_{line2}} \quad (2.5)$$

The conventional droop control strategy utilizes a simple operating characteristic for all operating conditions of the DERs, i.e., for the entire range of the DC voltage, in the islanded microgrid. Thus, the values of the virtual resistances significantly affect the system stability, voltage regulation, and power-sharing accuracy. Small virtual resistances result in more accurate voltage regulation and less accurate power-sharing, and vice versa [95], [96]. Besides, it is shown in Section 2.3.4 that the droop control strategy may cause unnecessary curtailment of the power generated by the RESs and also requires larger BESSs for acceptable voltage regulation under large disturbances. The DBS control strategy proposed in the next section significantly improves the DC microgrid voltage regulation and power sharing performances, by utilizing more advanced operating characteristics.

2.3 DC Bus Signaling Control

The DBS control strategy [37]-[47] utilizes multiple predefined DC voltage ranges to determine the operation modes of the DERs and the GTC. The operation mode of each component changes instantaneously whenever the corresponding bus voltage enters any of the aforementioned ranges. The existing DBS control strategies differ from each other in terms of how the operation modes of the DERs and the GTC are determined in each DC voltage range. Regardless of these differences, the existing DBS control strategies either necessitate high-rated GTC or BESSs to manage large power imbalances or unnecessarily curtail renewable power generation instead of storing the extra power in BESSs [37]-[47]. In this section, an improved DBS control strategy is proposed for the DC microgrid to address the aforementioned issues.

Table 2.1: Proposed DBS operation states.

State	DC Voltage Level	DC Microgrid	GTC	BESS	RES	Load
I	$V_{th2} < V < V_{th1}$	Grid-Connected	Full-Power Inverting	Full-Power Charging	Voltage Control	Demand
		Islanded	Disconnected			
II	$V_{th3} < V < V_{th2}$	Grid-Connected	Full-Power Inverting	Voltage Control	MPPT	Demand
		Islanded	Disconnected			
III	$V_{th4} < V < V_{th3}$	Grid-Connected	Voltage Control	Standby	MPPT	Demand
		Islanded	Disconnected	Voltage Control		
IV	$V_{th5} < V < V_{th4}$	Grid-Connected	Full-Power Rectifying	Voltage Control	MPPT	Demand
		Islanded	Disconnected			
V	$V_{th6} < V < V_{th5}$	Grid-Connected	Full-Power Rectifying	Full-Power	MPPT	Shedding
		Islanded	Disconnected	Discharging		

2.3.1 Operation States

In the proposed DBS control strategy, the operation characteristics of the RESs, BESSs, and the GTC are divided into five states, which are summarized in Table 2.1 and shown in Figure 2.3. At any time instant, the operation states of the DERs and the GTC are determined by comparing their DC bus voltages with six voltage thresholds $V_{th1} - V_{th6}$. Under steady-state, the power balance equation for the DC microgrid is [39], [44], [51]:

$$P_{RES} + P_{BESS} + P_{GTC} - P_{Load} = 0 \quad (2.6)$$

where P_{RES} , P_{BESS} , P_{GTC} and P_{Load} represent the total active powers of the RESs, BESSs, GTC and loads, respectively. Ideally, in each state, only one of these powers is adjusted by the proposed DBS control strategy, to maintain the power balance of (2.6) and regulate the DC bus voltages. However, in non-compact DC microgrids, where bus voltages are not necessarily equal, more than one converter might simultaneously adjust their powers to regulate the bus voltages.

2.3.1.1 State I ($V_{th2} < V < V_{th1}$)

This state represents the scenario where the excess power in the DC microgrid is beyond the level that can be exported by the GTC or absorbed by BESS(s), and thus renewable power generation has to be curtailed. The GTC exports its maximum power to the AC grid when the DC microgrid is grid-connected. The BESS(s) operate in full-power charging

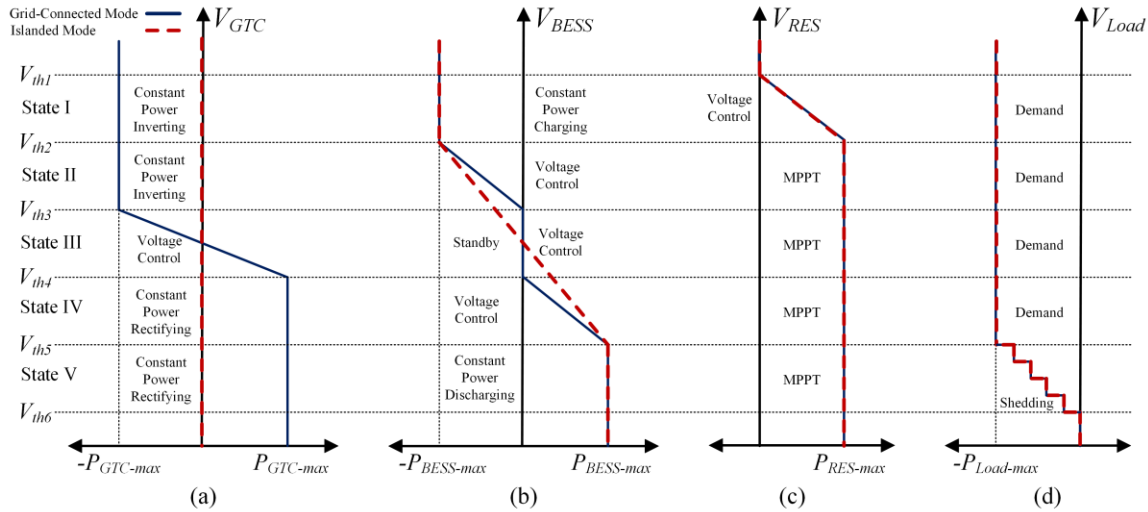


Figure 2.3: Proposed DBS operation states: (a) GTC, (b) BESS, (c) RES, (d) load.

mode. The RES(s) reduce their output powers based on their terminal voltages, to regulate the voltages and maintain the microgrid stability.

2.3.1.2 State II ($V_{th3} < V < V_{th2}$)

In State II, the excess power in the DC microgrid can be absorbed by the BESS(s) without causing curtailment of renewable power generation. If the microgrid is grid-connected, the GTC exports its maximum power to the AC grid. The RES(s) operate in maximum power point tracking (MPPT) mode. The BESS(s) have to adjust their input power(s) in order to maintain the power balance and regulate the DC voltage.

2.3.1.3 State III ($V_{th4} < V < V_{th3}$)

In State III, the GTC and the BESS(s) are both able to balance the power in the DC microgrid. Hence, the GTC and the BESS(s) provide voltage regulation under the grid-connected and islanded mode, respectively, while the RESs operate in MPPT mode.

2.3.1.4 State IV ($V_{th5} < V < V_{th4}$)

In state IV, the power deficit in the DC microgrid can be compensated by the BESS(s), without a need for load shedding. If the microgrid is grid-connected, the GTC imports its maximum power from the AC grid. The RES(s) operate in the MPPT mode. The BESS(s) adjust their output power(s) in order to maintain the power balance and regulate the DC voltage.

2.3.1.5 State V ($V_{th6} < V < V_{th5}$)

In case the power deficit in the microgrid is beyond the level that can be compensated by the GTC or BESS(s), some of the non-critical loads have to be shed to prevent voltage collapse. The GTC receives its maximum power from the AC grid in the grid-connected mode. The RES(s) operate in the MPPT mode and the BESS(s) operate in the full-power discharging mode.

2.3.2 Voltage Thresholds

The voltage thresholds used to determine the operation states should be selected carefully. If the differences between the voltage thresholds are large, the bus voltage deviations can exceed the acceptable range. Using voltage thresholds that are too close to each other should be also avoided, to prevent unnecessary curtailment of the RES output powers, and also because sensor inaccuracy and voltage ripples could cause oscillatory behavior. Therefore, the voltage thresholds are chosen to be $V_{th1} = 1.1$ p.u., $V_{th2} = 1.075$ p.u., $V_{th3} = 1.025$ p.u., $V_{th4} = 0.975$ p.u., $V_{th5} = 0.925$ p.u., and $V_{th6} = 0.9$ p.u. These thresholds limit voltage deviations to $\pm 10\%$. This set of thresholds also coordinates the operating characteristics of all RESs, BESSs, and the GTC without any gaps or overlaps between the five states of Table 2.1. This coordination enables smooth transition between the aforementioned states under large disturbances. The adverse effects of inappropriate voltage thresholds on the power sharing and voltage regulation performance of the DC microgrid are highlighted in Section 2.3.3. It should be noted that the aforementioned thresholds are not universal standards and they could vary from one microgrid to another microgrid. For example, in small-scale DC microgrids, where the voltage drop across the lines are negligible, the voltage thresholds could be closer to 1 p.u. in order to further limit the voltage deviations.

2.3.3 Control of the DERs and the GTC

This section introduces the control systems of the DERs and the GTC, based on the proposed DBS control strategy.

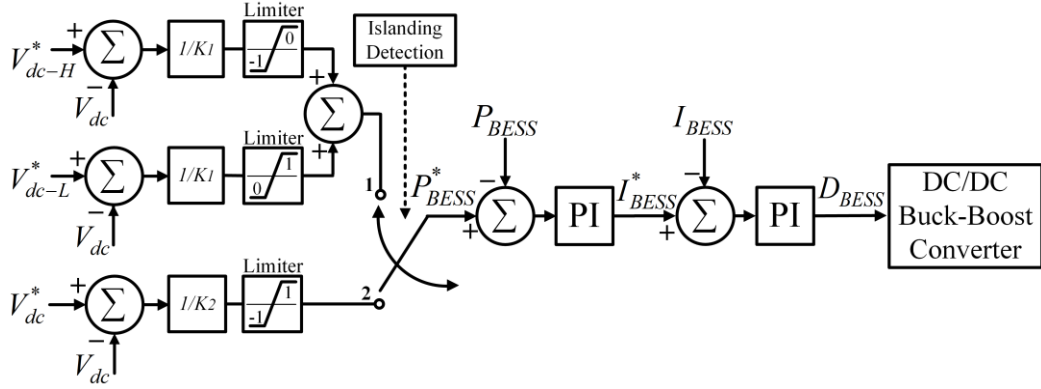


Figure 2.6: Control block diagram of the BESS.

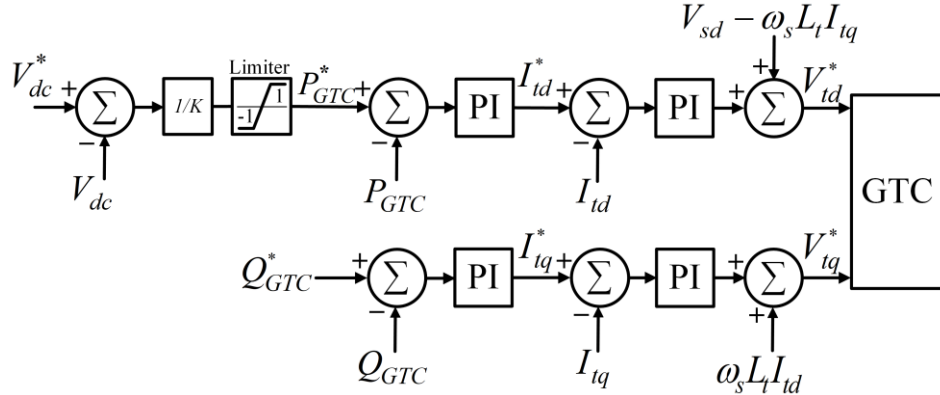


Figure 2.7: Control block diagram of the GTC.

2.3.3.3 BESS Control

The BESS maintains the power balance in both the grid-connected and islanded modes to control the DC bus voltage. The control block diagram of the BESS is shown in Figure 2.6, where the BESS voltage references, V_{dc-H}^* and V_{dc-L}^* , and the droop gain K_1 are 1.025, 0.975 and 0.05 p.u., respectively, in the grid-connected mode, and the BESS voltage reference V_{dc}^* and the droop gain K_2 are 1 and 0.075 p.u., respectively, in the islanded mode. Transition from the grid-connected mode to the islanded mode is detected using the rate of change of voltage (ROCOV).

2.3.3.4 GTC Control

The GTC controls its active and reactive powers in the grid-connected mode to regulate the DC bus voltage and meet the AC grid requirements, respectively. The conventional GTC control method is vector control. The control block diagram of the GTC is shown in

Figure 2.7, where the GTC voltage reference V_{dc}^* and the droop gain K are 1 and 0.025 p.u., respectively.

2.3.4 Performance Evaluation

This section investigates the performance of the proposed DBS control strategy under various generation and load disturbances in both grid-connected and islanded microgrids. Comprehensive time-domain simulation studies are conducted in the PSCAD software environment using the DC microgrid study system of Figure 1.1

2.3.4.1 Case Study 1

The first case study investigates the scenario where the total power demand by the loads is reduced and the grid-connected DC microgrid has to handle the resulting large power surplus. As shown in Figure 2.8, before the disturbance is applied at $t = 1$ s, the DC microgrid is in steady-state, and the DER terminal voltages are between 1.01 and 1.045 p.u. The WT, PV1 and PV2 operate in the MPPT mode and generate 1, 0.5 and 0.5 MW power, respectively, while the total power demand is 1.31 MW. The BESS1 and BESS2 draw 0.04 and 0.1 MW power, respectively, and the GTC exports 0.47 MW power to the AC grid in order to maintain the power balance.

At $t = 1$ s, the total power demand reduces to 0.69 MW, which leads to voltage rise in the DC microgrid, as shown in Figure 2.8(a). Therefore, the GTC and the BESSs start to absorb larger amounts of power from the DC microgrid, to maintain the power balance and limit the voltage rise. At $t = 1.5$ s, the total power demand is further reduced to 0.05 MW (almost no load), which causes the DER voltages to rise again. The GTC reaches its power limit by exporting 1 MW to the AC grid. The power balance is achieved by increasing the powers drawn by the BESSs and decreasing the power generated by the WT.

The results of the *Case Study 1* indicate that, in a practical DC microgrid, the voltages measured by the DERs can be different. Hence, all DERs do not always necessarily operate in the same state. In addition, the results show that the proposed DBS control strategy effectively regulates the DC bus voltages and provides an acceptable dynamic response to a large disturbance, i.e. the maximum power surplus, in the grid-connected microgrid.

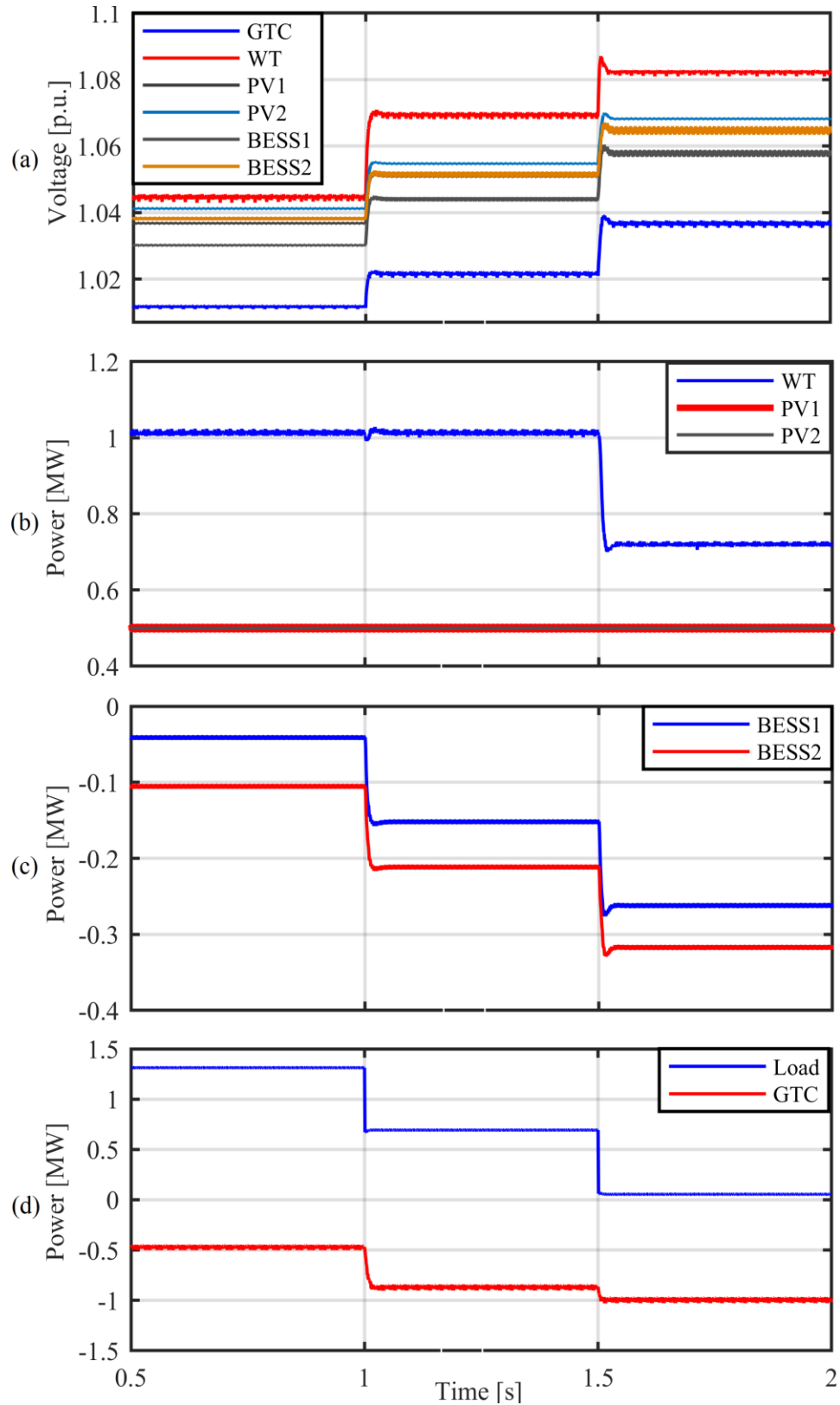


Figure 2.8: Performance of the proposed DBS control strategy in the *Case Study 1*: (a) DER terminal voltages, (b) WT and PVs powers, (c) BESSs powers, (d) GTC and load powers.

2.3.4.2 Case Study 2

The second case study investigates the scenario where the power generation by the RESs is reduced and the grid-connected DC microgrid has to handle the resulting large power deficit. As shown in Figure 2.9, before the disturbance is applied at $t = 1$ s, the DC microgrid is in the initial steady-state described in the *Case Study 1*.

At $t = 1$ s, the power generation levels of the WT, the PV1 and the PV2 are reduced to 0.5, 0.25 and 0.25 MW, respectively, which leads to voltage drop in the entire DC microgrid, as shown in Figure 2.9(a). The GTC reacts to this situation by importing 0.36 MW power from the AC grid to maintain the power balance, while the BESSs are in the standby mode. At $t = 1.5$ s, the power generation of the RESs are reduced to zero, which makes the DER voltages drop again. The GTC reaches its power limit by importing 1 MW from the AC grid. The BESS1 and BESS2 automatically start to inject 0.16 and 0.17 MW power into the DC microgrid, respectively, and maintain the power balance.

The results of the *Case Study 2* indicate that the proposed DBS control strategy effectively regulates the DC bus voltages and provides acceptable transient behavior under the maximum power deficit in the grid-connected microgrid.

2.3.4.3 Case Study 3

The third case study investigates the performance of the proposed DBS control strategy during the transition of the DC microgrid from the grid-connected mode to the islanded mode. As shown in Figure 2.10, before $t = 1$ s, the grid-connected DC microgrid operates in the initial steady-state described in the *Case Study 1*.

At $t = 1$ s, the DC microgrid is disconnected from the AC grid and the GTC power exchange becomes zero. Thus, the DER terminal voltages increase, as shown in Figure 2.10(a). The BESSs react to the voltage rise by drawing 0.64 MW power. At $t = 1.5$ s, the power generation of each PV is reduced to 0.25 MW, while the total power demand is almost unchanged. Thus, the bus voltages start to drop. The BESSs reduce their absorbed powers to about 0.07 MW to maintain the power balance and regulate the bus voltages. The results of the *Case Study 3* indicate that the proposed control strategy effectively

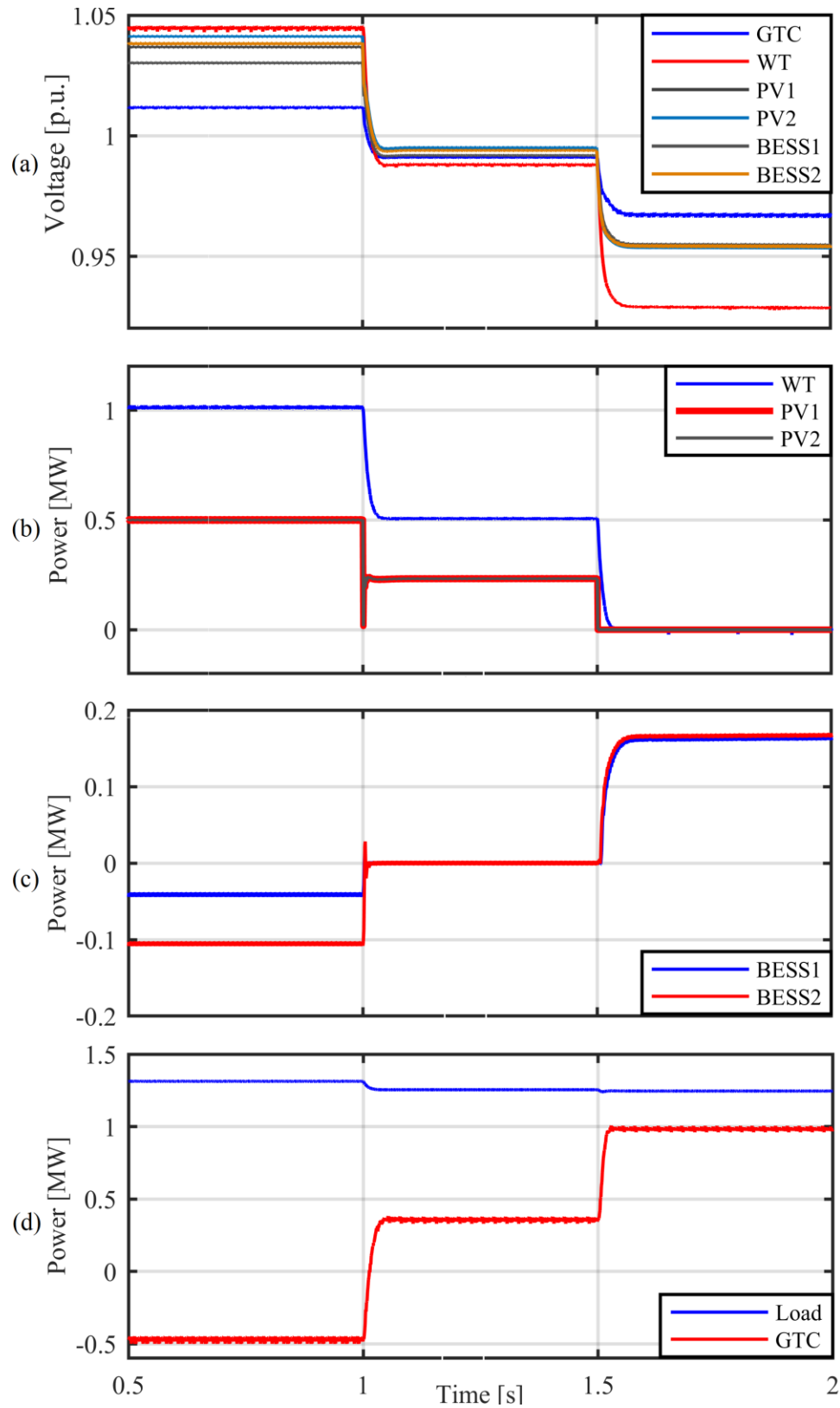


Figure 2.9: Performance of the proposed DBS control strategy in the *Case Study 2*: (a) DER terminal voltages, (b) WT and PVs powers, (c) BESSs powers, (d) GTC and load powers.

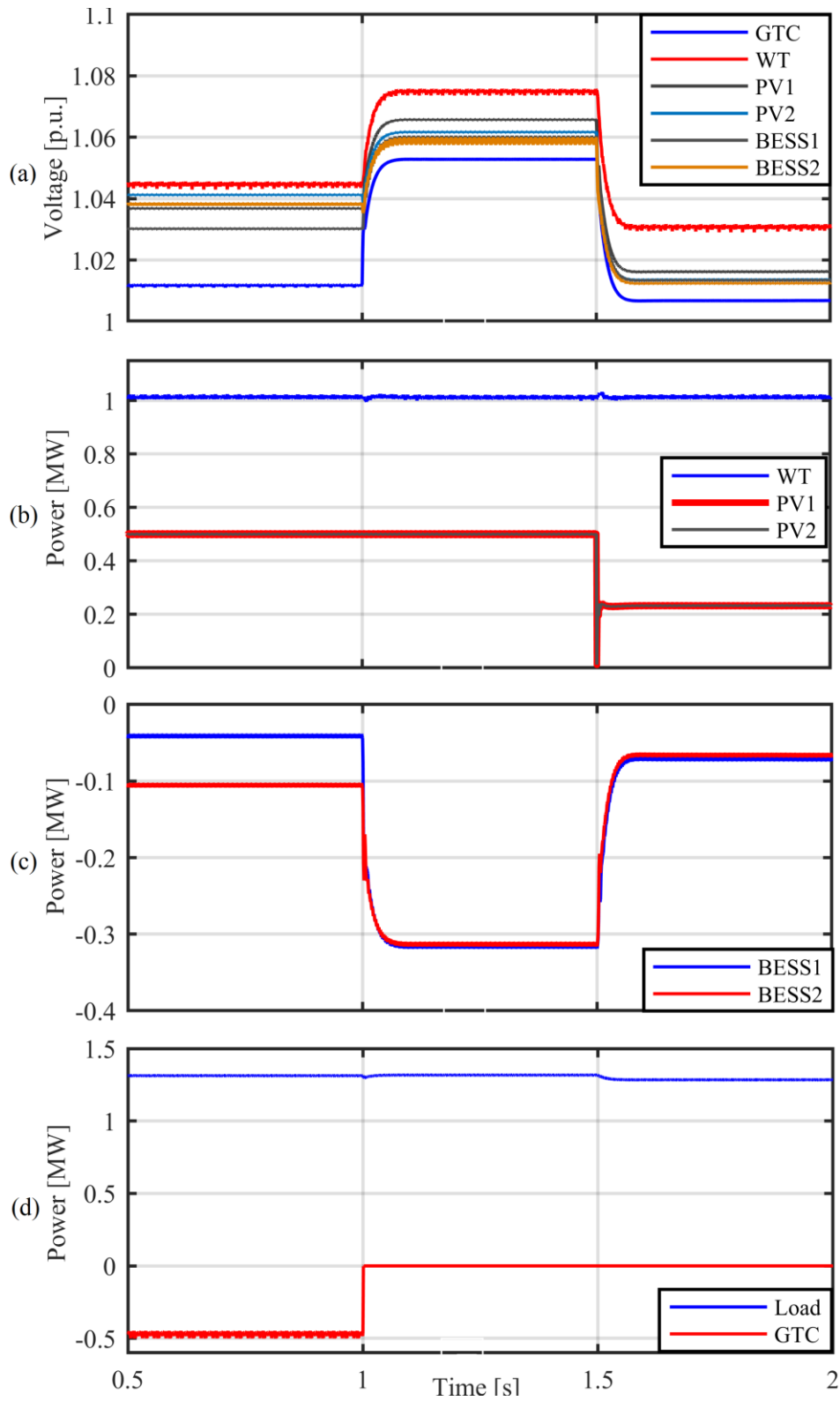


Figure 2.10: Performance of the proposed DBS control strategy in the *Case Study 3*: (a) DER terminal voltages, (b) WT and PVs powers, (c) BESSs powers, (d) GTC and load powers.

regulates the bus voltages and provides acceptable dynamic response during transition of the DC microgrid from the grid-connected to islanded mode and a subsequent disturbance in the islanded mode.

In order to illustrate the impacts of the voltage thresholds $V_{th1} - V_{th6}$ on the performance of the proposed DBS control strategy, the *Case Study 3* is repeated with two different sets of voltage thresholds. The first set of thresholds are exactly two times of the values given in Section 2.3.2, i.e., twice the values used to obtain the results of Figure 2.10. The second set of thresholds are exactly half of the values given in Section 2.3.2.

Figure 2.11 shows the results of the *Case Study 3*, using the first set of thresholds, i.e., $2V_{th}$. As shown in Figure 2.11(a), the larger voltage thresholds cause larger voltage deviations, especially under large disturbances. Although the larger thresholds improve the power sharing between the BESSs, Figure 2.11(c), the voltage regulation performance is not acceptable, since the bus voltages exceed 1.1 p.u.

Figure 2.12 shows the results of the *Case Study 3*, using the second set of thresholds, i.e., $V_{th}/2$. As shown in Figure 2.12(a), the smaller voltage thresholds considerably improve the voltage regulation. However, the smaller thresholds cause unnecessary curtailment of the power generated by the WT, Figure 2.12(b), and also degrade the power sharing among the BESSs, Figure 2.12(c).

The two sets of thresholds used to obtain the results of Figures 2.11 and 2.12 do not represent all possible threshold values, but provide an insight on how higher or lower threshold values could affect the microgrid performance. The results of Figures 2.11 and 2.12 confirm that the voltage thresholds provided in Section 2.3.2.2 provide acceptable performance in terms of power sharing and bus voltage regulation.

2.3.4.4 Case Study 4

The fourth case study investigates the scenario where the total power generation by the RESs is increased and the total power demand is decreased, and the islanded DC microgrid has to handle the resulting large power surplus.

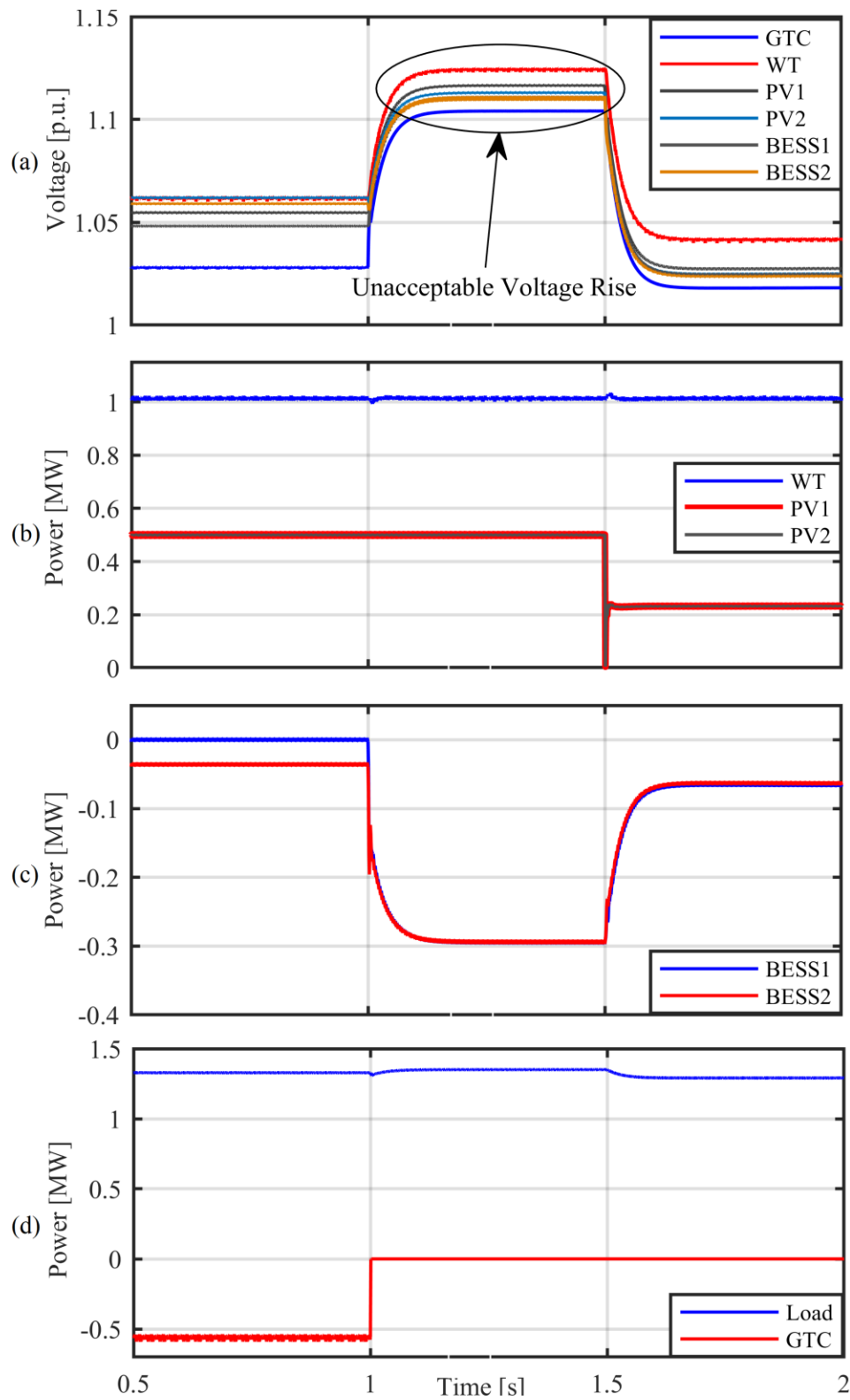


Figure 2.11: Performance of the proposed DBS control strategy with $2V_{th}$ in the *Case Study 3*: (a) DER terminal voltages, (b) WT and PVs powers, (c) BESSs powers, (d) GTC and load powers.

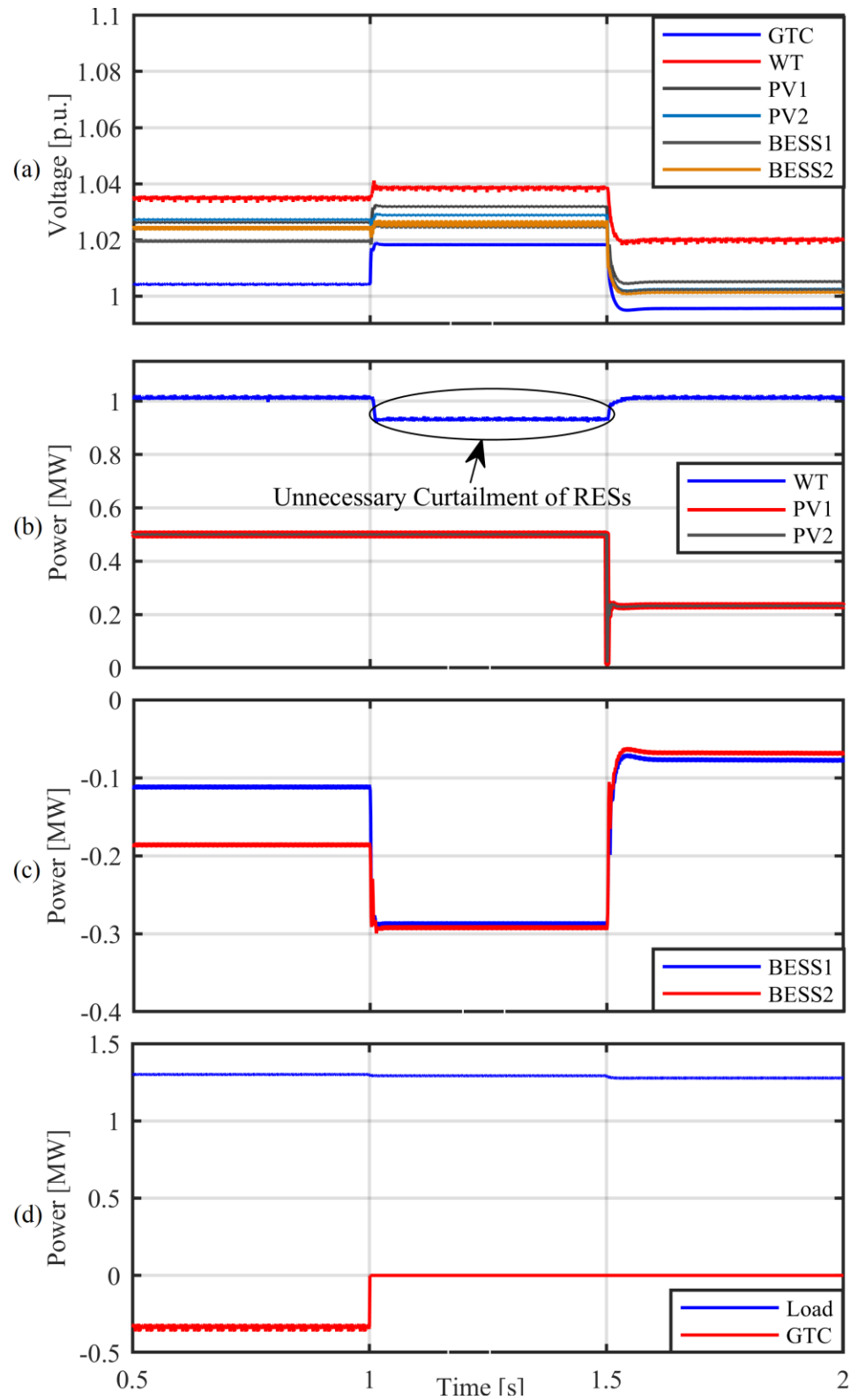


Figure 2.12: Performance of the proposed DBS control strategy with $V_{th}/2$ in the *Case Study 3*: (a) DER terminal voltages, (b) WT and PVs powers, (c) BESSs powers, (d) GTC and load powers.

As shown in Figure 2.13, initially the islanded DC microgrid is in steady-state, and the DER terminal voltages are between 1 and 1.03 p.u. The WT, PV1, and PV2 operate in the MPPT mode and generate 1, 0.25 and 0.25 MW power, respectively, while the total power demand is 1.28 MW. Both BESSs draw 0.07 MW power. At $t = 1$ s, the power generation of each PV is increased to 0.5 MW, which causes voltage rise in the microgrid, Figure 2.13(a). As a result, the BESSs start to absorb larger amounts of power from the DC microgrid to limit the voltage rise. At $t = 1.5$ s, the total power demand is reduced to 0.45 MW, which makes the bus voltages rise again. The BESSs reach their power limits by absorbing 0.4 MW each. Therefore, the power balance is achieved by decreasing the power generated by the WT, PV1, and PV2 to 0.42, 0.42 and 0.47 MW, respectively.

In order to compare the performance of the proposed DBS control strategy with that of the conventional droop control strategy described in Section 2.2, the *Case Study 4* is repeated with the BESSs controlled using droop characteristics and the RESs operated in the MPPT mode. The power ratings of the GTC, BESSs and RESs are not changed. Figure 2.14 shows the performance of the droop-controlled islanded microgrid under the operating conditions and disturbances of Figure 2.13. As shown in Figure 2.14(a), after the total power demand is reduced to 0.45 MW at $t = 1.5$ s, the DER voltages uncontrollably increase and exceed the upper limit of 1.1 p.u. This is due to the limited power ratings of the BESSs.

This issue could be prevented by increasing the power ratings of the BESSs or by operating the RESs using droop controllers as well. Both cases are not economically justifiable since larger BESSs would increase the investment cost and droop control of the RESs (instead of MPPT) would lead to unnecessary curtailment of the power generated by the RESs under normal operating conditions.

The results of the *Case Study 4* indicate that, unlike the conventional droop control strategy, the proposed DBS control strategy provides acceptable voltage regulation and power sharing performance under large power surplus in the islanded microgrid, without requiring oversized BESSs or unnecessarily curtailing the output powers of the RESs.

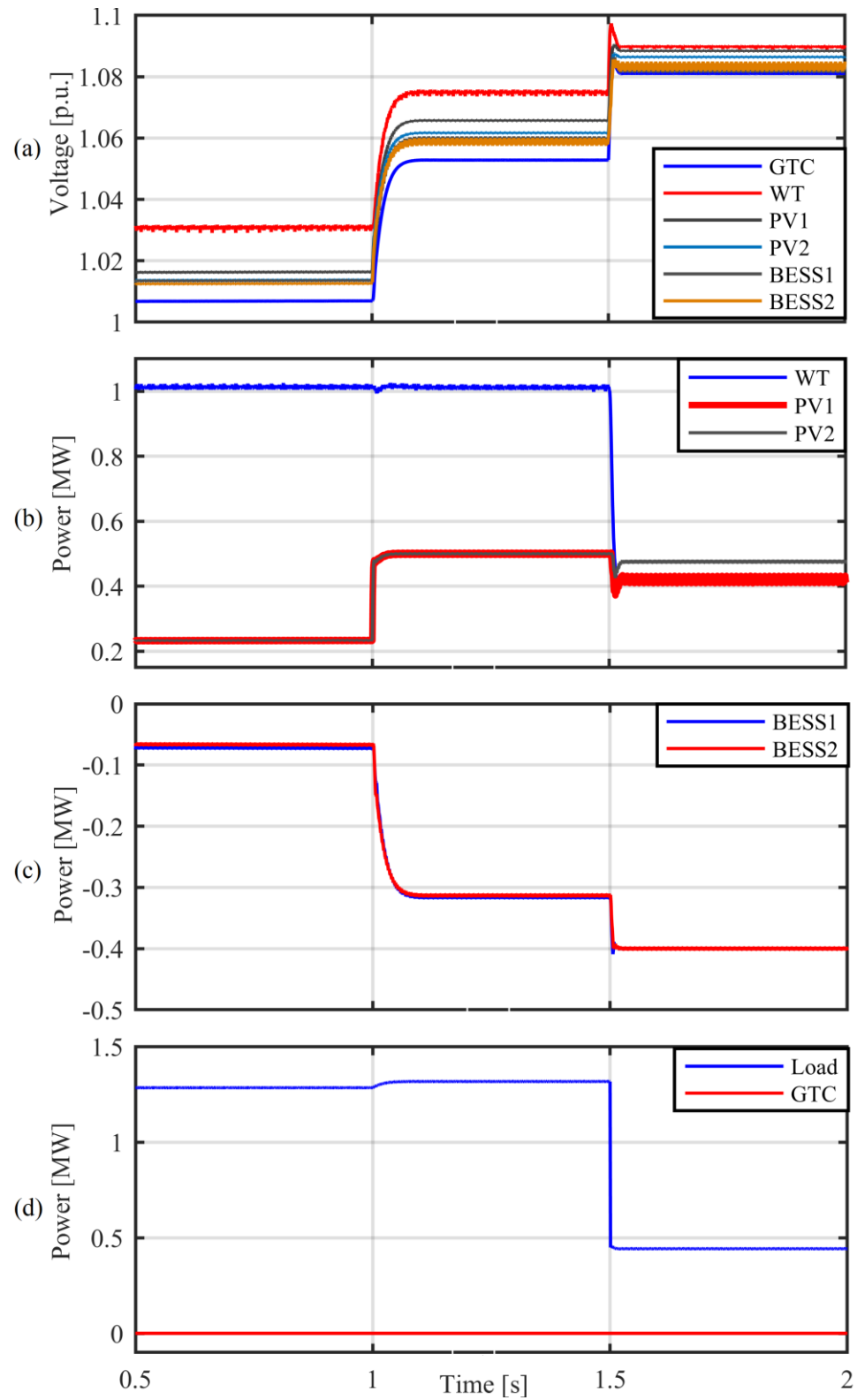


Figure 2.13: Performance of the proposed DBS control strategy in the *Case Study 4*: (a) DER terminal voltages, (b) WT and PVs powers, (c) BESSs powers, (d) GTC and load powers.

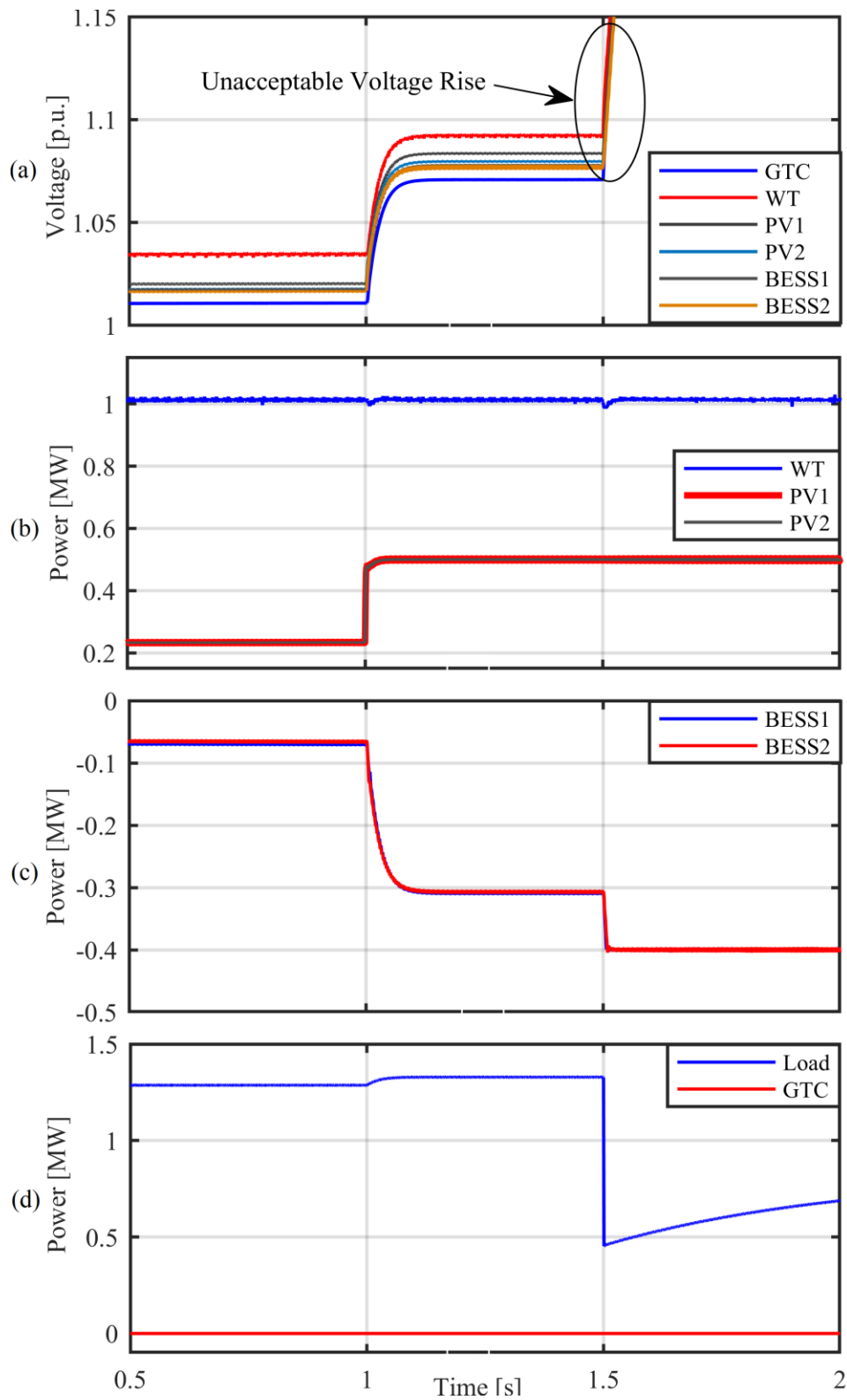


Figure 2.14: Performance of the conventional droop control strategy in the *Case Study 4*: (a) DER terminal voltages, (b) WT and PVs powers, (c) BESSs powers, (d) GTC and load powers.

2.3.4.5 Case Study 5

The fifth case study investigates the scenario where the total power generated by the RESs is reduced and the islanded DC microgrid has to handle the resulting power deficit. As shown in Figure 2.15, initially the islanded DC microgrid operates in the steady-state described in the *Case Study 4*. At $t = 1$ s, the power generated by the WT is reduced to 0.5 MW, which leads to voltage drop in the entire DC microgrid, as shown in Figure 2.15(a). As a result, the BESS1 and the BESS2 respectively inject 0.18 and 0.14 MW power to maintain the power balance, Figure 2.15(c). At $t = 1.5$ s, the total power generated by the RESs is further reduced to 0.25 MW, which causes the DER terminal voltages to drop to lower values. In response to this disturbance, both BESSs inject their maximum power of 0.4 MW to the microgrid. Since the power demand is greater than the maximum power that can be supplied by the DERs, 0.3 MW of the non-critical loads is shed in two steps, to prevent the DC voltage collapse. After the load shedding, the bus voltages return to the acceptable range. Subsequently, the BESS1 and the BESS2 maintain the power balance in the microgrid by injecting 0.38 and 0.34 MW power, respectively.

The *Case Study 5* is also used to compare the performance of the proposed control strategy with that of the droop control strategy. Figure 2.16 shows the performance of the droop-controlled islanded microgrid under the operating conditions and disturbances of Figure 2.15. The BESSs are droop-controlled and the RESs operate in the MPPT mode. The power ratings of the GTC, the BESSs and the RESs are not changed. As shown in Figure 2.16(a), after the total power generation is reduced to 0.25 MW at $t = 1.5$ s, the bus voltages uncontrollably decrease, and fall below the lower limit of 0.9 p.u. This issue could be prevented by increasing the power ratings of the BESSs and the RESs, which would significantly increase the investment cost.

The results of the *Case Study 5* indicate that, unlike the conventional droop control strategy, the proposed DBS control strategy provides acceptable voltage regulation and power sharing performance under large power deficit in the islanded microgrid, without requiring oversized BESSs and RESs.

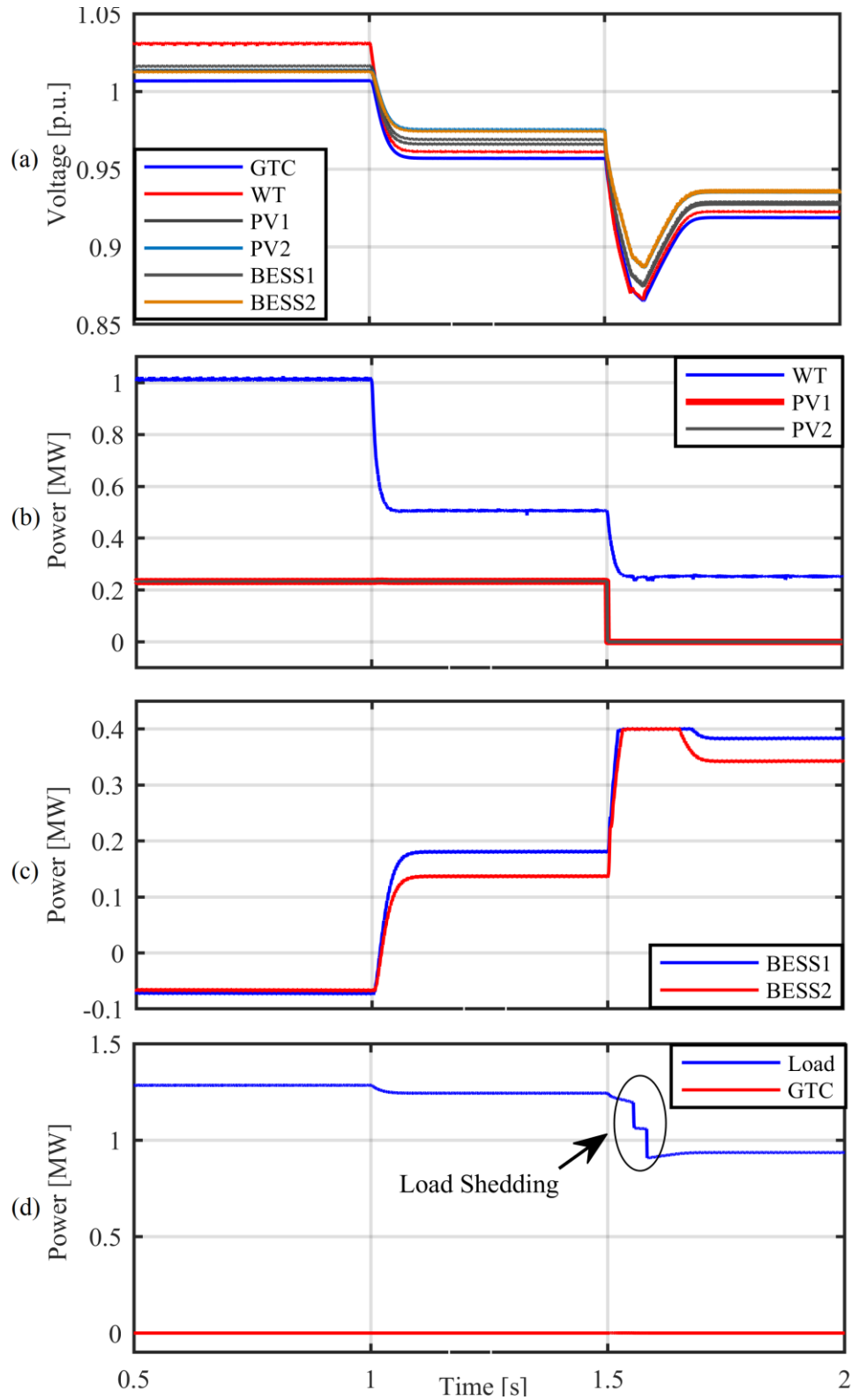


Figure 2.15: Performance of the proposed DBS control strategy in the *Case Study 5*: (a) DER terminal voltages, (b) WT and PVs powers, (c) BESSs powers, (d) GTC and load powers.

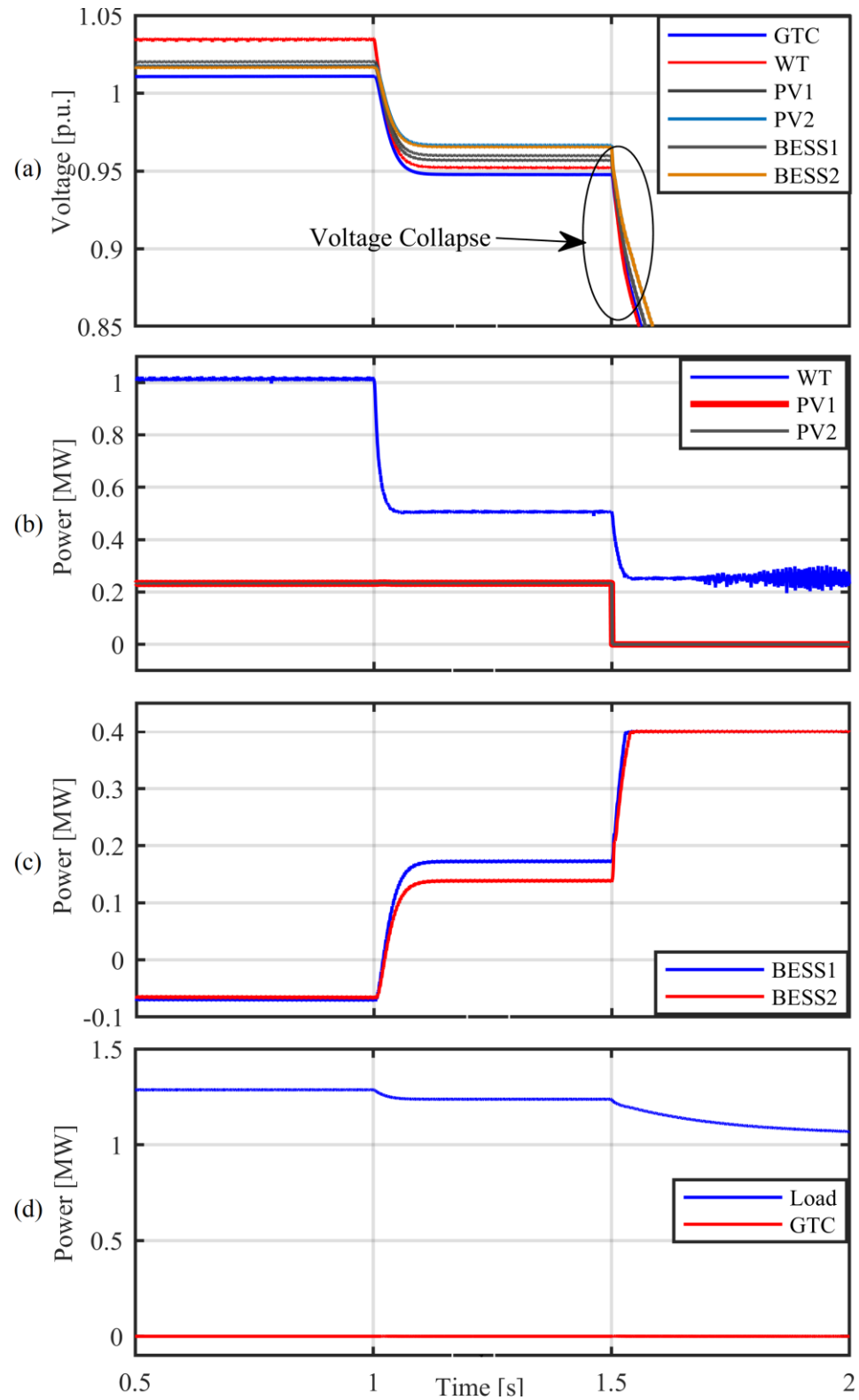


Figure 2.16: Performance of the conventional droop control strategy in the *Case Study 5*: (a) DER terminal voltages, (b) WT and PVs powers, (c) BESSs powers, (d) GTC and load powers.

2.4 Mode Adaptive Droop Control

The MADC strategy utilizes a hysteresis characteristic to switch between voltage control by the RESs and the BESSs in the islanded DC microgrid, depending on the bus voltage variations [48]-[53]. This section briefly introduces the conventional MADC strategy and also proposes an improved MADC strategy.

2.4.1 Conventional MADC Strategy

In the conventional MADC strategy, the GTC regulates the bus voltages of the grid-connected DC microgrid. The bus voltage regulation in the islanded DC microgrid is performed by the DERs, i.e., the RESs and the BESSs, since the GTC is unable to exchange power with the AC grid. Thus, each DER in the islanded DC microgrid operates in one of the following two modes [48], [49].

- *Mode I*: In this operation mode, the BESSs regulate the DC bus voltages using their droop characteristics, while the RESs utilize their MPPT controllers to maximize the harvested energy.
- *Mode II*: This mode is activated when the BESSs are unable to prevent excessive over-voltages by absorbing their maximum powers. Hence, the power balance is maintained and the bus voltages are regulated by curtailing the power outputs of the RESs using droop characteristics.

The operation mode of each DER is determined depending on its DC bus voltage, using the hysteresis characteristic of Figure 2.17. When the voltage falls below the predefined threshold V_{th1} , the operation mode is switched to *Mode I*, and when the voltage exceeds the threshold V_{th2} , the DER operation mode is switched to *Mode II* [48], [49]. In an ideal DC microgrid, the DC voltages seen by all DERs are almost equal. In such a system, depending on the MADC mode, either all BESSs or all RESs participate in regulating the bus voltages.

In a practical DC microgrid, where the voltage drops across the lines may cause the bus voltages to be considerably different, some of the DERs may fail to switch to the appropriate operation mode when it is necessary. This takes place when a relatively large DER switches to the voltage regulation mode, i.e., *Mode I* for the BESSs and *Mode II* for the RESs, before

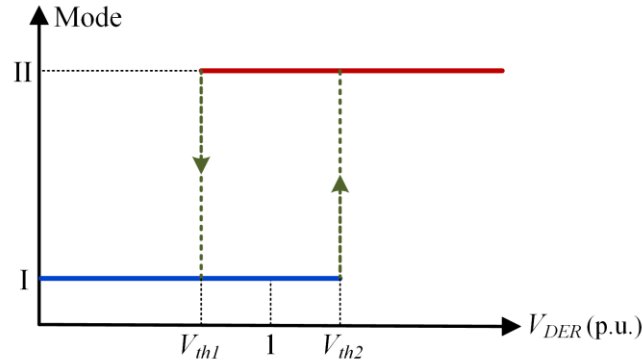


Figure 2.17: Mode switching characteristics of the conventional MADC strategy.

the other DERs do so. The resulting improvement in the voltage profile of the microgrid may prevent some other DERs from performing the appropriate mode change, as shown in Section 2.4.3. This issue may lead to unacceptable power sharing and voltage regulation performances and poor dynamic response to disturbances.

2.4.2 Improved MADC Strategy

In this section, an improved MADC strategy is proposed to address the mode switching issues of the conventional MADC strategy. The aforementioned improvement is made using an adaptive mode switching algorithm and appropriate DER control systems.

2.4.2.1 Adaptive Mode Switching Algorithm

The main idea is to delay all mode change actions such that none of the DERs attempts to change its operation mode in response to a voltage disturbance, before all other DERs detect the disturbance. The delay must be sufficiently large to ensure that all bus voltages will reach the mode change threshold, before the first DER changes its operation mode. The delay must also be sufficiently small to ensure that all of the bus voltages remain within the acceptable range. Thus, the adaptive time delay of (2.7), which depends on the ROCOV, is utilized to satisfy the aforementioned constraints.

$$T_{delay} = \begin{cases} T_{max} & , \quad \text{if } 0 < \left| \frac{dV_{dc}}{dt} \right| < k_1 \\ \frac{\Delta V}{\left| dV/dt \right|} & , \quad \text{if } k_1 \leq \left| \frac{dV_{dc}}{dt} \right| \leq k_2 \\ T_{min} & , \quad \text{if } k_2 < \left| \frac{dV_{dc}}{dt} \right| < \infty \end{cases} \quad (2.7)$$

$$\frac{T_{min}}{T_{max}} = \frac{k_1}{k_2} \quad (2.8)$$

The parameter $\Delta V = \min((V_{max} - V_{th2}), (V_{th1} - V_{min}))$ represents the voltage change caused by the delayed mode switching, before the voltage reaches its upper limit V_{max} or lower limit V_{min} . The maximum and minimum values of the adaptive time delay T_{delay} are denoted by T_{max} and T_{min} , respectively. The constants $k_1 = \Delta V/T_{max}$ and $k_2 = \Delta V/T_{min}$ are the values of the ROCOV at which the T_{delay} reaches the aforementioned maximum and minimum values, respectively. Under large disturbances, where the ROCOV is significant, the adaptive delay becomes shorter and allows faster mode switching to limit the voltage deviation. Under small disturbances, where the ROCOV is insignificant, the adaptive delay becomes longer and enables mode switching of all DERs. Figure 2.18 shows the variations of the adaptive time delay T_{delay} with respect to the ROCOV. Figure 2.19 shows the mode switching characteristics of the improved MADC strategy.

The parameters of the proposed MADC strategy, i.e., V_{min} , V_{max} , V_{th1} , V_{th2} , T_{min} , and T_{max} should be selected carefully. The values of the upper and lower voltage limits V_{max} and V_{min} are assumed to be 1.1 p.u. and 0.9 p.u., respectively. Adopting a much larger V_{max} or a much smaller V_{min} may cause power quality issues (excessive over-voltage or under-voltage conditions). The voltage thresholds V_{th1} and V_{th2} affect the adaptive mode changing performance. Choosing voltage thresholds that are too close to the aforementioned voltage limits leads to a small voltage margin ΔV in (2.7), and disables the adaptive adjustment of the mode changing time delay. On the other hand, using voltage thresholds that are too close to 1 p.u. should be avoided, since sensor inaccuracy and voltage ripples could cause oscillatory behavior [38], [42]. Under normal operating conditions, the bus voltage deviations caused by the voltage drop across the lines can be as high as ± 0.05 per-unit. Thus,

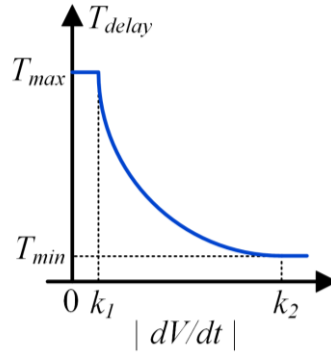


Figure 2.18: Variations of the adaptive time delay with respect to the ROCOV.

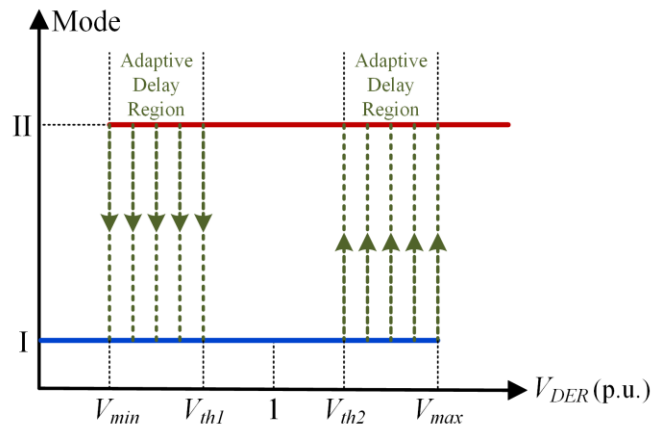


Figure 2.19: Mode switching characteristics of the improved MADC strategy.

choosing voltage thresholds in the ranges of $V_{min} \leq V_{th1} \leq 0.95$ p.u. and 1.05 p.u. $\leq V_{th2} \leq V_{max}$ is recommended. In microgrids with short lines, where the line voltage drops are lower than 0.05 p.u., values closer to 1 p.u. can be chosen for the voltage thresholds. The time delays T_{min} and T_{max} are determined such that reliable mode changing performance is achieved without causing excessively long delays in voltage regulation.

Figure 2.20 shows the V - I characteristics of the DERs in both operation modes. This figure illustrates that all DERs (RESs and BESSs) utilize two modes of operation. In Mode I, all RESs operate in the MPPT mode and all BESSs operate within their current limits to regulate their DC bus voltages. In Mode II, all BESSs operate in the charging mode and all RESs operate within their current limits to regulate their DC bus voltages.

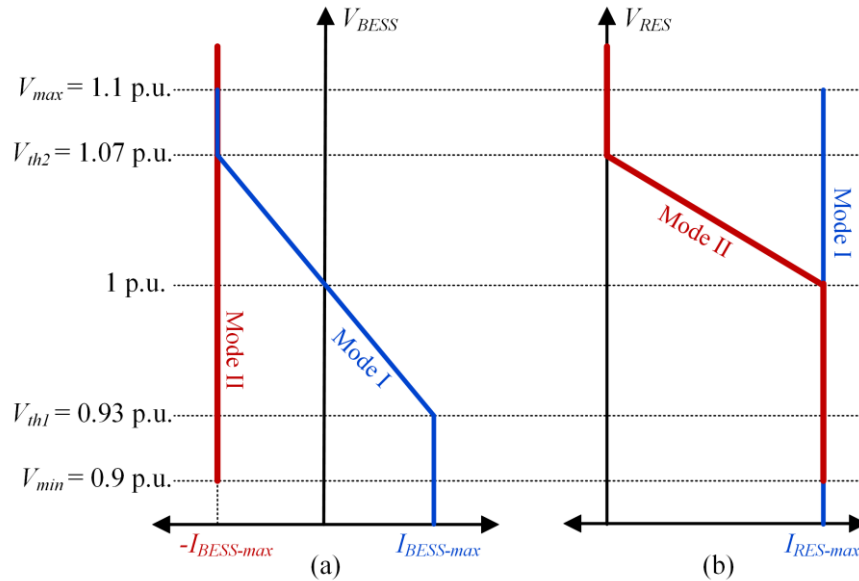


Figure 2.20: V-I characteristics of the mode-adaptive droop controlled DERs, (a) BESS, and (b) RES.

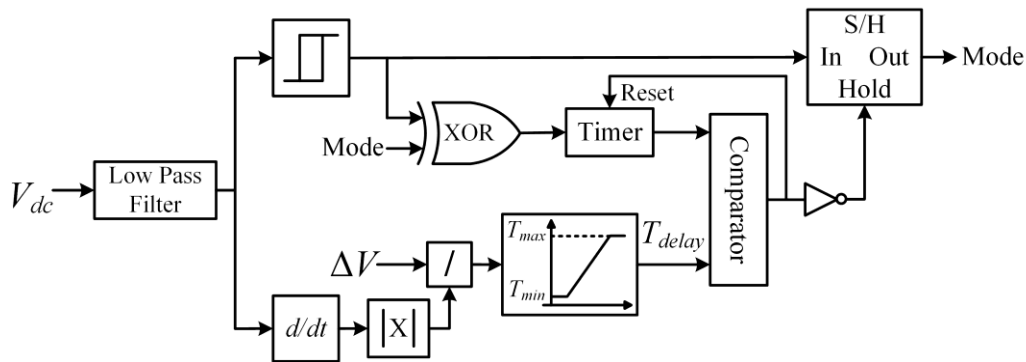


Figure 2.21: Block diagram of the adaptive mode switching algorithm.

The block diagram of the proposed adaptive mode switching algorithm is shown in Figure 2.21. The hysteresis block in Figure 2.21 represents the conventional mode switching algorithm and generates a mode signal that can be either I or II. The timer is enabled to count whenever the output of the hysteresis block is not the same as the current operation mode. The comparator output becomes high as soon as the timer output exceeds the adaptive delay of (2.7), and thereby allows the Sample-and-Hold (S/H) block to refresh its output and perform the mode switching. As shown in Figure 2.21, a fourth-order Butterworth low-pass filter with the cut-off frequency of 500 Hz is applied to the voltage signal to reduce the adverse effects of noise and switching ripples.

2.4.2.2 DER Control Systems

This sub-section introduces the DER control systems utilized by the proposed improved MADC strategy.

2.4.2.2.1 WT Control

The control system of the PMSG-type WT includes a pitch angle controller and the VSC controller. The former limits the aerodynamic torque and keeps the turbine speed in a limited range. The latter is based on the vector control method in the dq reference frame. Depending on the MADC mode, the VSC controls the PMSG active power to achieve MPPT or to regulate the DC voltage. The VSC also controls the reactive power to regulate the stator terminal voltage [83]-[85]. The WT control system is shown in Figure 2.22, where V_{ref}^* and R_d are the DC bus voltage reference and the droop gain, respectively.

2.4.2.2.2 PV Control

Each PV generation unit either generates its maximum power using an MPPT controller or regulates the DC bus voltage, depending on the MADC mode. A general perturbation and observation MPPT method is implemented for the PV system [39], [38], [51]. The control block diagram of the PV system is shown in Figure 2.23.

2.4.2.2.3 BESS Control

Each BESS either operates in the charging mode or participates in regulating the DC bus voltages, depending on the MADC mode. The control block diagram of each BESS is shown in Figure 2.24.

2.4.3 Performance Evaluation

This section investigates and compares the performance of the proposed improved MADC strategy with those of the conventional MADC strategy and the DBS control strategy under various disturbances that cause different levels of power imbalance. Comprehensive time-domain simulation studies are conducted in the PSCAD software environment using the DC microgrid study system of Figure 1.1.

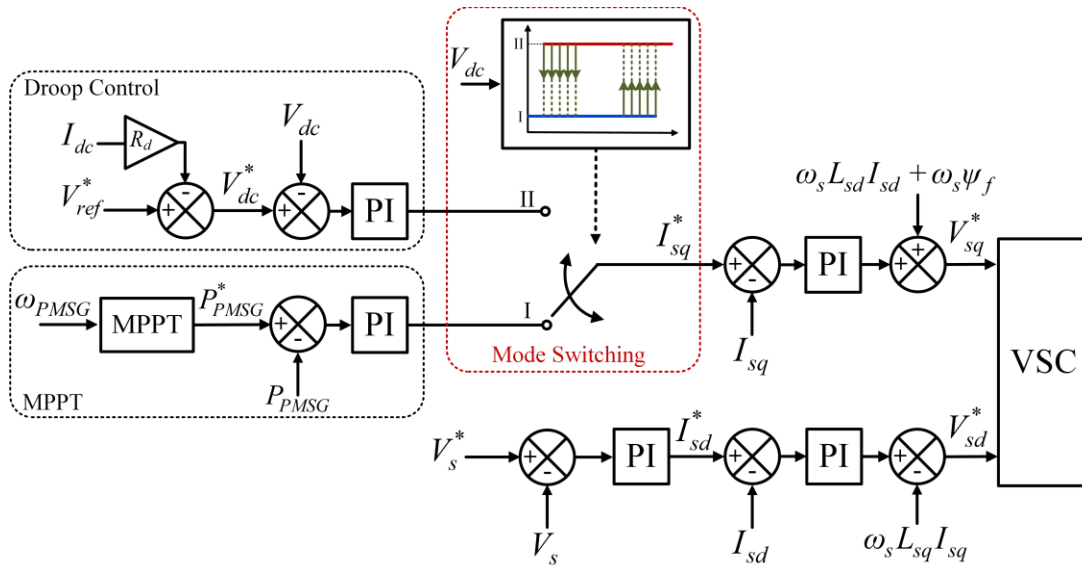


Figure 2.22: Control block diagram of the PMSG-type WT.

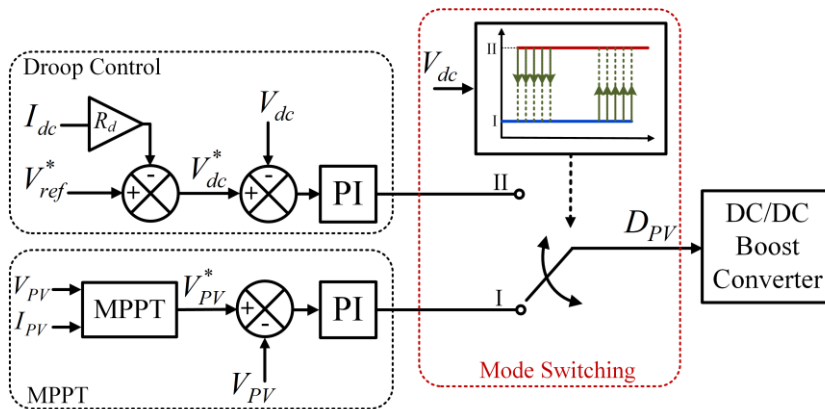


Figure 2.23: Control block diagram of the PV.

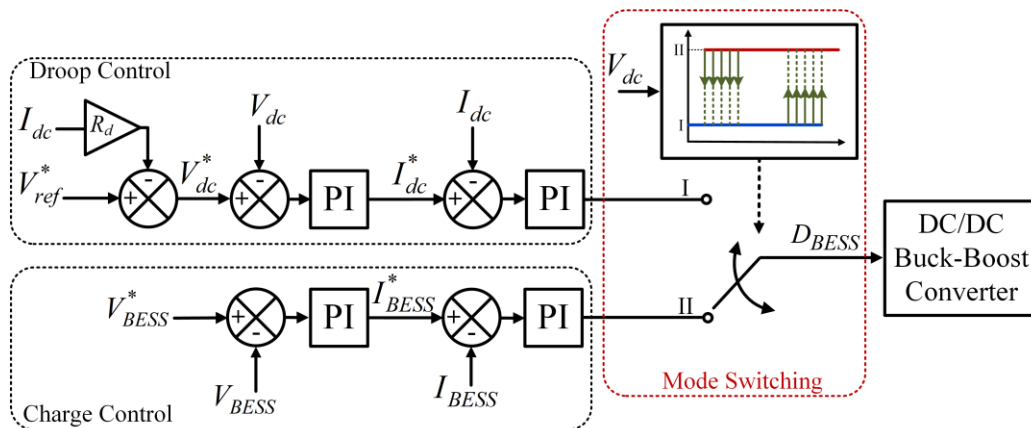


Figure 2.24: Control block diagram of the BESS.

The DER terminal voltages and output powers are reported in per-unit, to enable comparison and easier analysis of the study results. The base values for the DER powers and the bus voltages are the corresponding power ratings and the rated line-to-ground voltage of 750 V, respectively. The parameters of the improved MADC strategy are $V_{th1} = 0.93$ p.u., $V_{th2} = 1.07$ p.u., $V_{min} = 0.9$ p.u., $V_{max} = 1.1$ p.u., $\Delta V = 0.03$ p.u., $k_1 = 0.03$ p.u./s, $k_2 = 3$ p.u./s, $T_{min} = 0.01$ s, and $T_{max} = 1$ s. These values are determined based on the results of comprehensive simulation studies.

2.4.3.1 Case Study 1

The first case study investigates an unscheduled islanding scenario that leads to a large power surplus in the microgrid. Figures 2.25 and 2.26 illustrate the performances of the conventional and improved MADC strategies, respectively. At $t < 0.5$ s, the microgrid is grid-connected, and the DER bus voltages are regulated by the GTC at values approximately between 1.02 p.u. and 1.05 p.u. All RESs operate in MPPT and generate 1 p.u. power, while the total power demand of the loads is 0.4 MW. Both BESSs operate in the charging mode and draw 1 p.u. power from the DC microgrid. As the total power generated by the RESs is larger than the total power demand in the DC microgrid, the GTC exports 0.75 MW to the AC grid.

At $t = 0.5$ s, the DC microgrid is islanded and the GTC power exchange with the AC grid becomes zero. Due to the resulting power surplus in the microgrid, all bus voltages start to rise at an almost equal rate. Therefore, all DERs are expected to switch to the *Mode II* described in Section II. This means, the BESSs must draw their maximum charging currents and the RESs must curtail their output powers in order to maintain the power balance in the microgrid and regulate the bus voltages.

As shown in Figure 2.25, with the conventional MADC strategy, the WT changes its operation mode to *Mode II* as soon as its bus voltage reaches V_{th2} at $t = 0.508$ s. Consequently, the WT reduces its output power to 0.2 p.u. and regulates the DER bus voltages at about 1.06 p.u. The two PV generation systems PV1 and PV2 fail to switch to the voltage control mode since their bus voltages do not reach the mode changing threshold V_{th2} . These results demonstrate that, when the conventional MADC strategy is

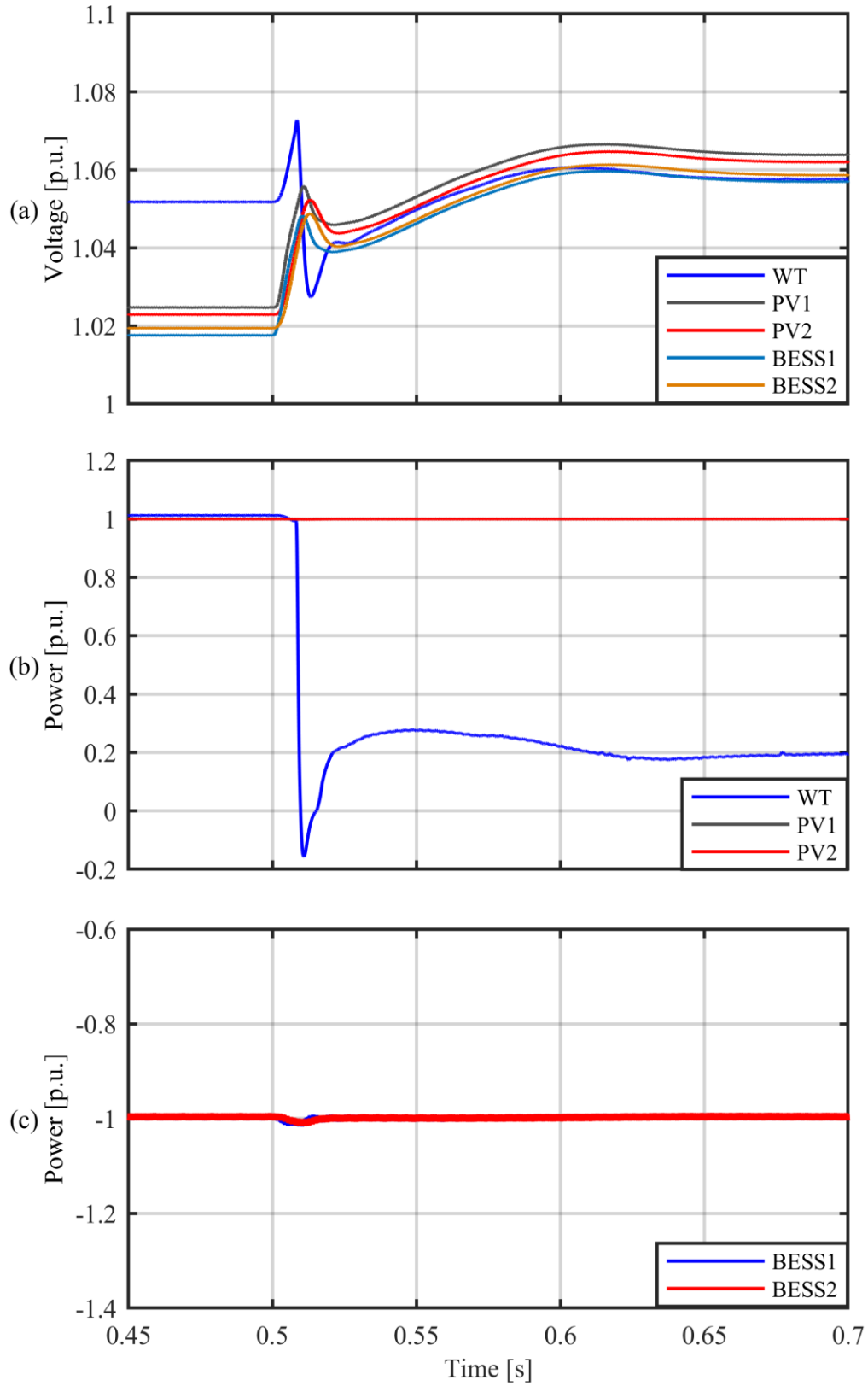


Figure 2.25: Performance of the conventional MADC strategy in the *Case Study 1*: (a) DER terminal voltages, (b) RES powers, (c) BESS powers.

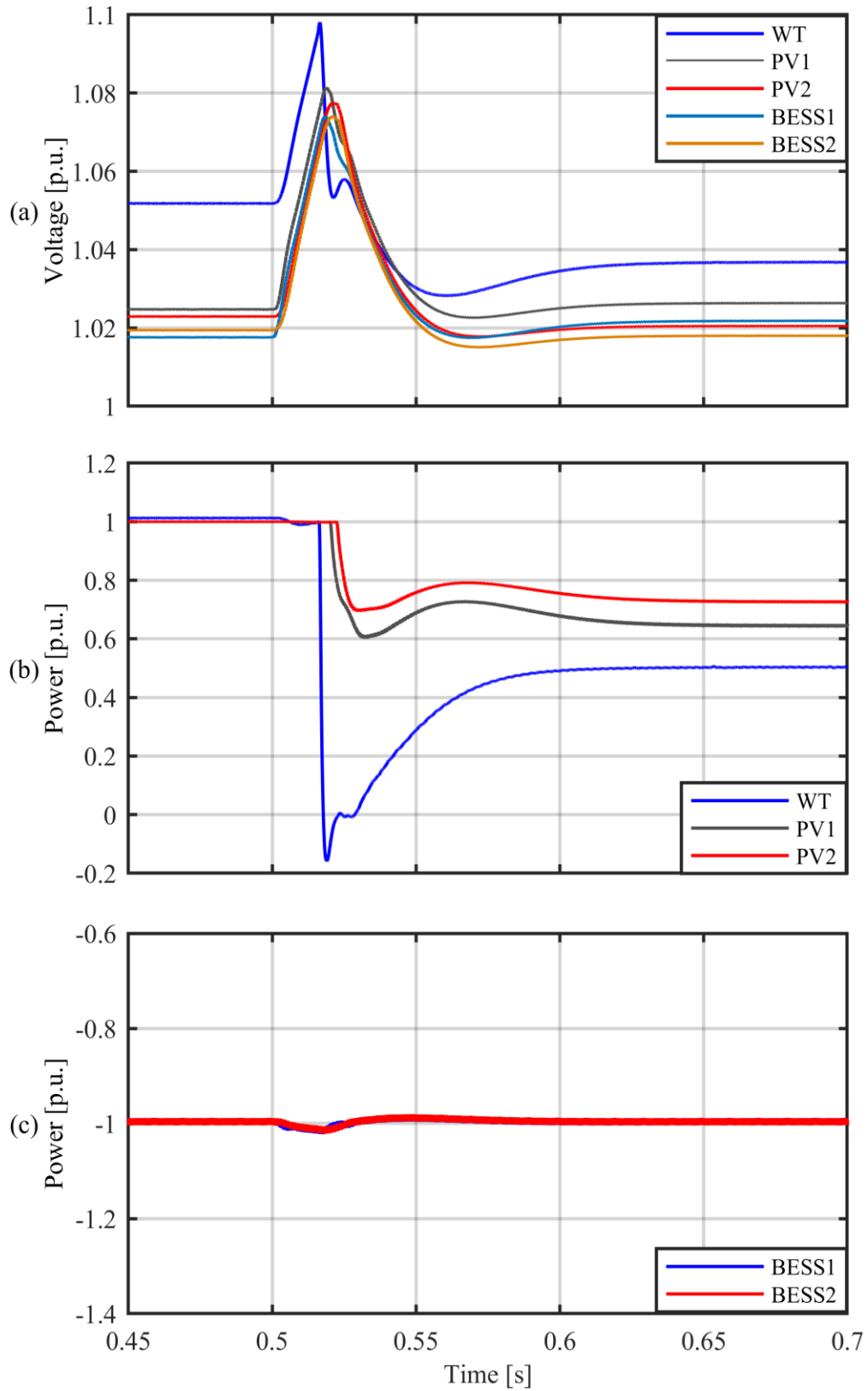


Figure 2.26: Performance of the improved MADC strategy in the *Case Study 1*: (a) DER terminal voltages, (b) RES powers, (c) BESS powers.

implemented in a practical DC microgrid, the faster reaction of a relatively large DER to a disturbance can desensitize some other DERs to that disturbance and prevent them from switching to the appropriate mode. This issue adversely affects the power sharing among the DERs, because the desensitized DERs, i.e., PV1 and PV2, do not participate in maintaining the power balance, as shown in Figure 2.25(b). This issue also leads to poor bus voltage regulation, as shown in Figure 2.25(a) at $t > 0.6$ s, because the only voltage regulating component is the WT, i.e., PVs 1 and 2 do not participate in voltage regulation.

Figure 2.26 shows that the proposed improved MADC strategy enables all RESs, i.e., the WT, the PV1, and the PV2, to switch to *Mode II* and participate in the voltage regulation. Consequently, all of the RESs reduce their output powers and regulate the DER bus voltages at values between 1.02 p.u. and 1.04 p.u. Figure 2.26(b) shows that the proposed improved MADC does not achieve ideal power sharing, i.e., the output powers of the three RESs are not exactly equal. However, this issue is a limitation of non communication-based control strategies, and is caused by unequal bus voltages in a practical microgrid. Achieving ideal power sharing would require costly communication systems. Besides, the power sharing performance of the proposed MADC strategy is considerably better than that of the conventional MADC strategy.

Figure 2.26(a) also shows that the proposed MADC strategy causes a slightly larger temporary voltage deviation before the mode switching takes place, i.e., at $0.51 \text{ s} < t < 0.52 \text{ s}$, as compared with the conventional MADC strategy of Figure 2.25(a). This is due to the additional adaptive mode switching delay that is utilized to prevent the mode switching failure issue illustrated in Figure 2.25(b). Allowing the bus voltages to continue to rise/fall for a short time period T_{delay} enables all DERs to detect the voltage variations and perform reliable mode switching. The utilized adaptive delay is determined by (2.7) such that the bus voltages do not reach the corresponding lower and upper limits which are assumed to be 0.9 p.u. and 1.1 p.u., respectively.

2.4.3.2 Case Study 2

The second case study investigates the islanding scenario of *Case Study 1*, but with different initial conditions. The main difference is that the total power demand of the loads in the grid-connected microgrid is increased to 0.85 MW. Hence, before the islanding, the GTC exports 0.3 MW to the AC grid. When the DC microgrid becomes islanded at $t = 0.5$ s, the power surplus in the microgrid is only 0.3 MW. The bus voltages rise at a rate that is lower than that of the *Case Study 1*. This case study mainly aims to demonstrate the necessity of utilizing a mode switching delay that is not fixed. Figures 2.27 and 2.28 show the performances of the conventional and improved MADC strategies, respectively.

As shown in Figure 2.27, similar to the *Case Study 1*, the conventional MADC strategy fails to provide acceptable mode switching performance in this case. Only the WT changes its operation mode to voltage control, while the other RESs (the PV1 and the PV2) remain in *Mode I*, that is the MPPT mode. Due to the small power surplus, the WT is able to restore the power balance in the islanded DC microgrid and regulate all DER bus voltages at values between 1.01 p.u. and 1.03 p.u. However, the PV1 and the PV2 fail to participate in the voltage regulation, similar to the *Case Study 1*. This failure, which is illustrated in Figures 2.25(b) and 2.27(b), forces the WT to curtail a larger portion of its output power.

Figure 2.28 shows that, by utilizing a larger time delay due to the low ROCOV, the proposed improved MADC strategy enables all three RESs to detect the disturbance, switch to *Mode II*, and participate in the voltage regulation. Consequently, all RESs reduce their output powers and thereby regulate the DER bus voltages at values between 1.0 p.u. and 1.02 p.u. As expected, the BESSs continue to operate in the charging mode before and after the disturbance.

Figure 2.28 shows that the performance of the improved MADC strategy is slightly better than that of the conventional MADC strategy, in terms of bus voltage regulation and power sharing among the RESs. This is due to the small power imbalance of 0.3 MW in the DC microgrid, which does not cause significant voltage deviations or large power curtailment by the RESs. The performance improvement is more significant when the power imbalance caused by the disturbance is large, e.g., *Case Study 1*.

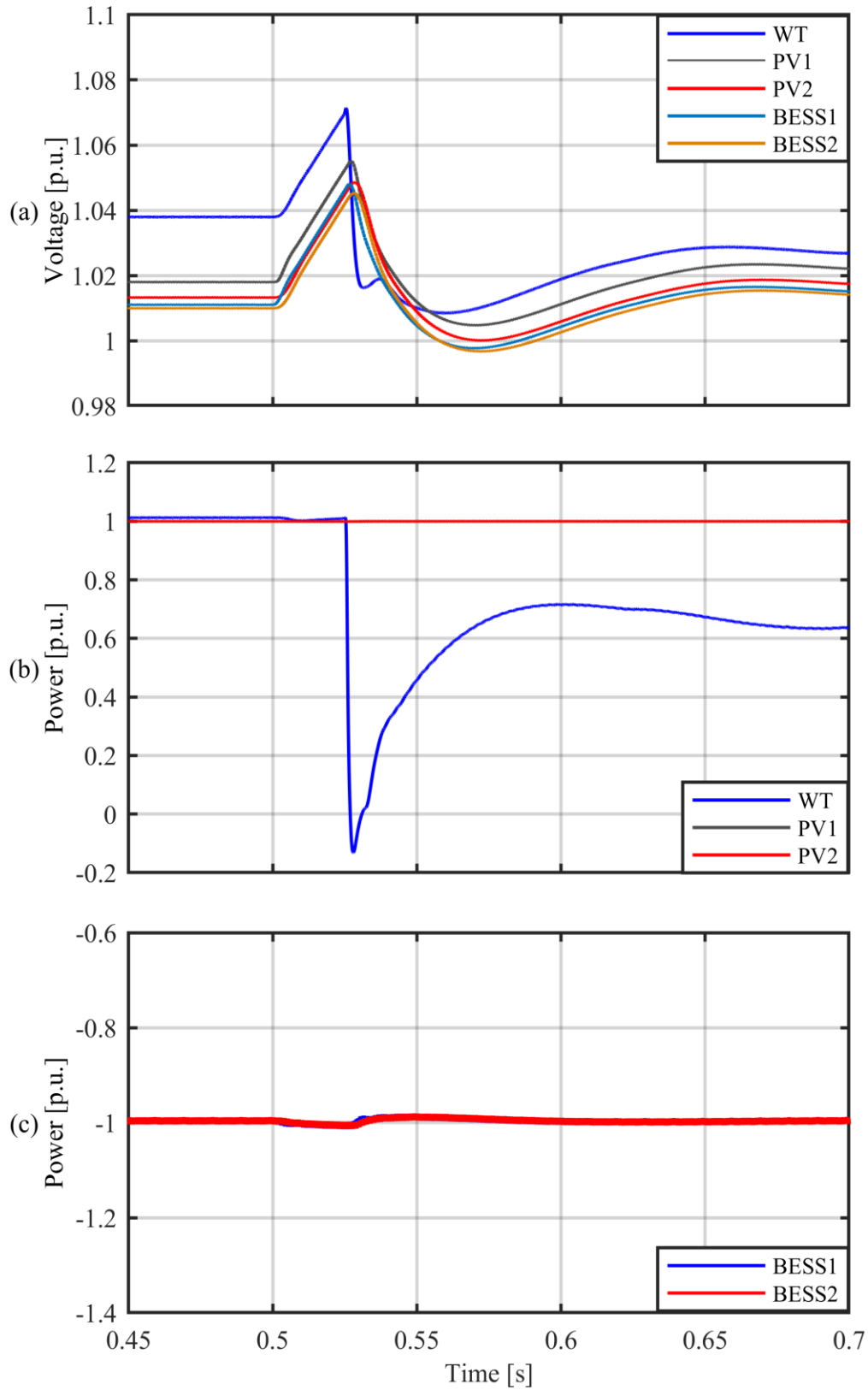


Figure 2.27: Performance of the conventional MADC strategy in the *Case Study 2*: (a) DER terminal voltages, (b) RES powers, (c) BESS powers.

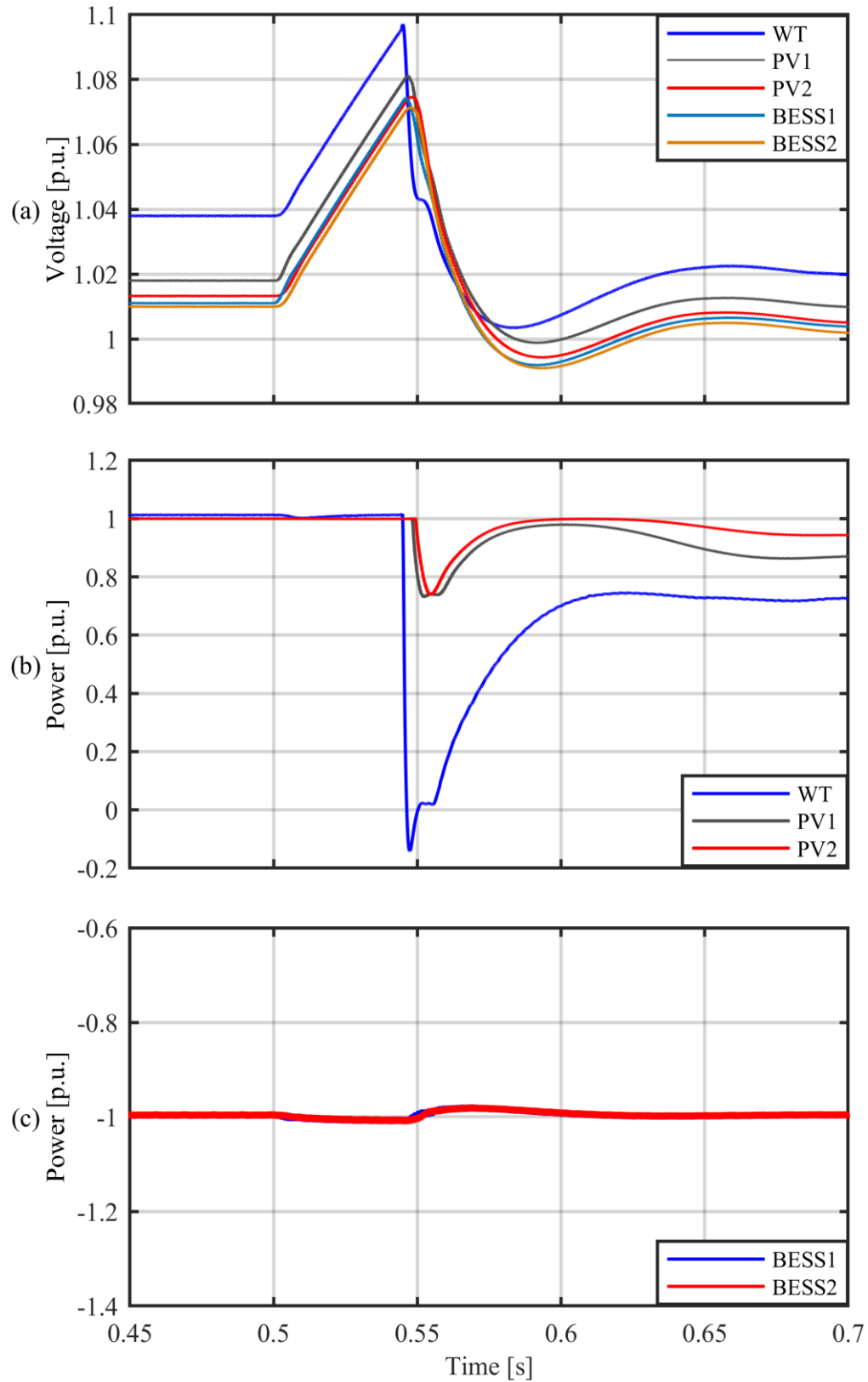


Figure 2.28: Performance of the improved MADC strategy in the *Case Study 2*: (a) DER terminal voltages, (b) RES powers, (c) BESS powers.

The Case studies 1 and 2 highlight two important points. First, the conventional MADC strategy may fail to coordinate the mode switching actions of the RESs under both low and high rates of voltage rise. Second, the adaptive delay utilized by the proposed improved MADC strategy enables reliable and coordinated mode switching by all RESs, regardless of how fast the bus voltages change.

2.4.3.3 Case Study 3

The third case study investigates and compares the performances of the conventional and improved MADC strategies during an islanding scenario that leads to a power deficit in the DC microgrid. Figures 2.29 and 2.30 illustrate the performances of the conventional and improved MADC strategies, respectively. Before $t = 0.5$ s, the microgrid is grid-connected, and the DER bus voltages are between 0.97 p.u. and 1.02 p.u. The WT, PV1, and PV2 operate in MPPT and generate 1, 0.5, and 0.5 p.u. power, respectively, while the total power demand of the loads is 1.25 MW. Both BESSs operate in the charging mode and draw 1 p.u. power. As the total power demand in the grid-connected microgrid is larger than the power generated by the RESs, the GTC imports 0.6 MW from the grid.

At $t = 0.5$ s, the microgrid is islanded. Due to the resulting 0.6 MW power deficit in the microgrid, all bus voltages start to fall at an almost equal rate. In this case study, all DERs are expected to switch to *Mode I* after islanding. Thus, after the islanding, the RESs are expected to continue to operate in MPPT and the BESSs are expected to adjust their power outputs in order to maintain the power balance and regulate the bus voltages.

As shown in Figure 2.29, with the conventional MADC strategy, only the BESS2 changes its operation mode to voltage control, due to its lower bus voltage. Thus, the DER bus voltages are regulated by the BESS2 at values between 0.96 p.u. and 0.98 p.u., while the BESS1 fails to perform the necessary mode switching and does not participate in the voltage regulation. In this case, the BESS1 is being charged in part by the BESS2, which increases the energy loss in the microgrid and causes faster discharge of the BESS2. The results of Figure 2.29 indicate that the shortcomings of the conventional MADC strategy also apply to the mode switching performances of the BESSs.

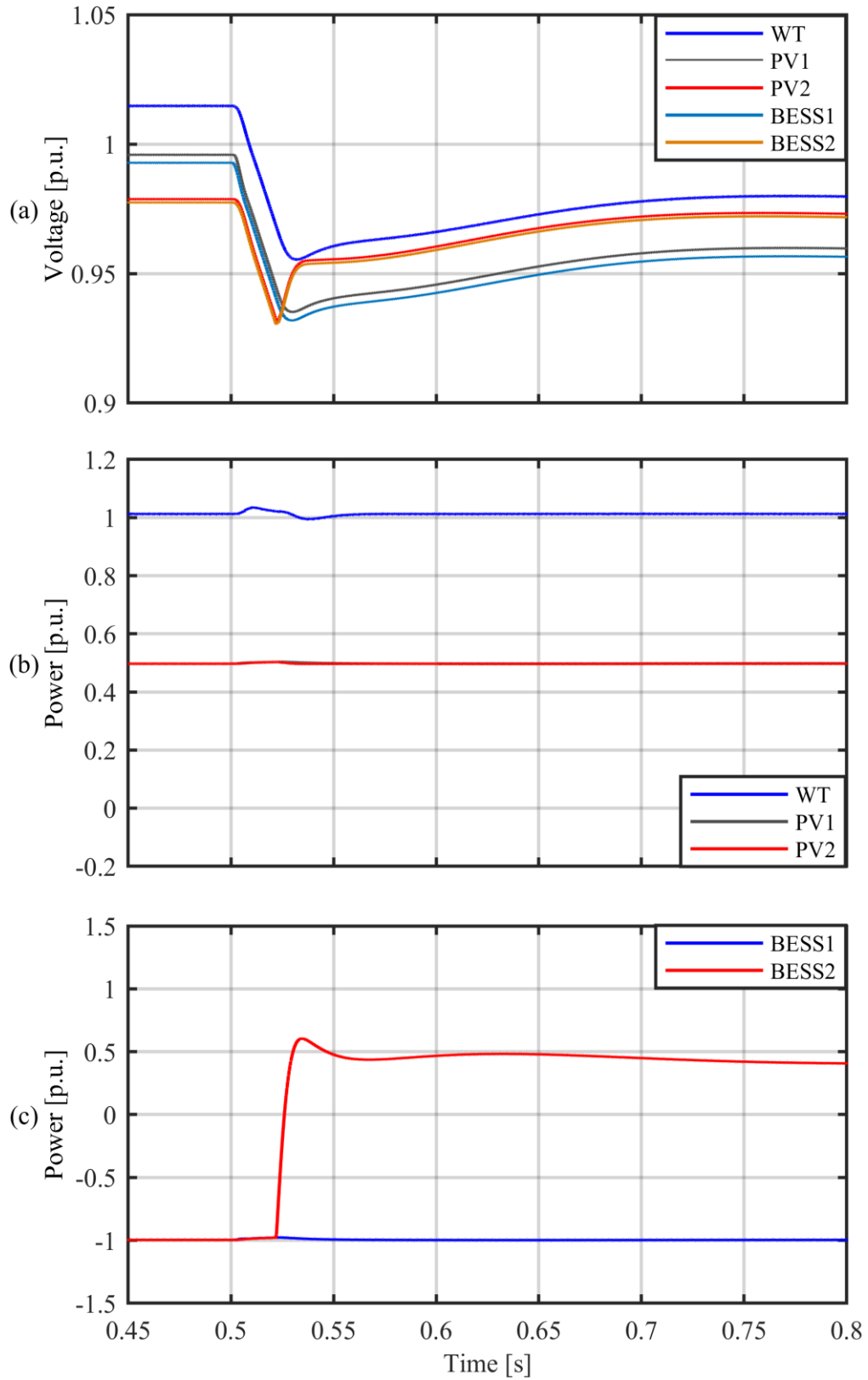


Figure 2.29: Performance of the conventional MADC strategy in the *Case Study 3*: (a) DER terminal voltages, (b) RES powers, (c) BESS powers.

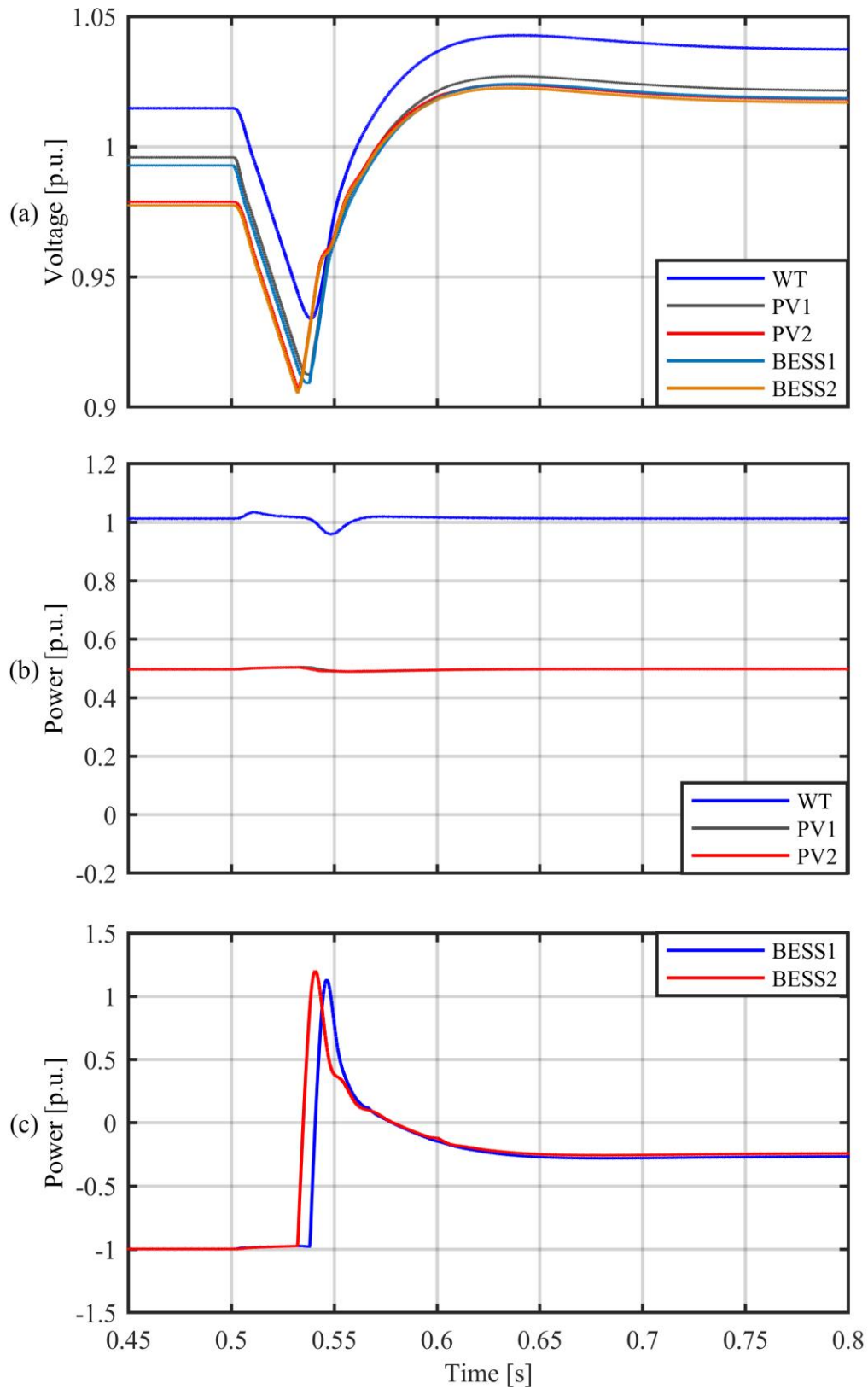


Figure 2.30: Performance of the improved MADC strategy in the *Case Study 3*: (a) DER terminal voltages, (b) RES powers, (c) BESS powers.

Figure 2.30 shows that the proposed improved MADC strategy enables both BESSs to participate in the voltage regulation and provide acceptable power sharing performance. Although the improvement in terms of reducing the voltage deviations is less significant in this specific case study, the fact that the BESSs perform desirable power sharing and do not cause circulating currents is a significant improvement.

2.4.3.4 Case Study 4

The fourth case study investigates two successive disturbances with opposite effects in terms of the power balance in the microgrid. The first disturbance is an islanding scenario that leads to a power deficit in the microgrid. The second disturbance is a load disconnection that causes a power surplus. Figures 2.31 and 2.32 illustrate the performances of the conventional and improved MADC strategies, respectively. Before $t = 0.5$ s, the microgrid is grid-connected, and the DER bus voltages are regulated by the GTC at about 1 p.u. The WT, the PV1, and the PV2 operate in MPPT and generate 0.5, 1, and 1 p.u. power, respectively, while the total power demand of the loads is 0.97 MW. Both BESSs operate in the charging mode and draw 1 p.u. power from the microgrid. As the total power demand in the grid-connected microgrid is larger than the power generated by the RESs, the GTC imports 0.3 MW from the AC grid.

At $t = 0.5$ s, the microgrid is islanded and the GTC power exchange with the AC grid becomes zero. Due to the resulting power deficit in the microgrid, all bus voltages start to fall at an almost equal rate. Therefore, after the islanding, all of the DERs are expected to switch to *Mode I*. In other words, the RESs are expected to continue to operate in MPPT and the BESSs are expected to adjust their power outputs in order to maintain the power balance and regulate the bus voltages.

At $t = 1$ s, the CB at node 709 is tripped, which decreases the total power demand of the loads to 0.68 MW. Due to the resulting power surplus in the microgrid, all bus voltages start to rise. Therefore, all DERs are expected to switch to *Mode II* described in Section II. This means the BESSs must draw their maximum charging currents and the RESs must curtail their output powers in order to maintain the power balance and regulate the bus voltages.

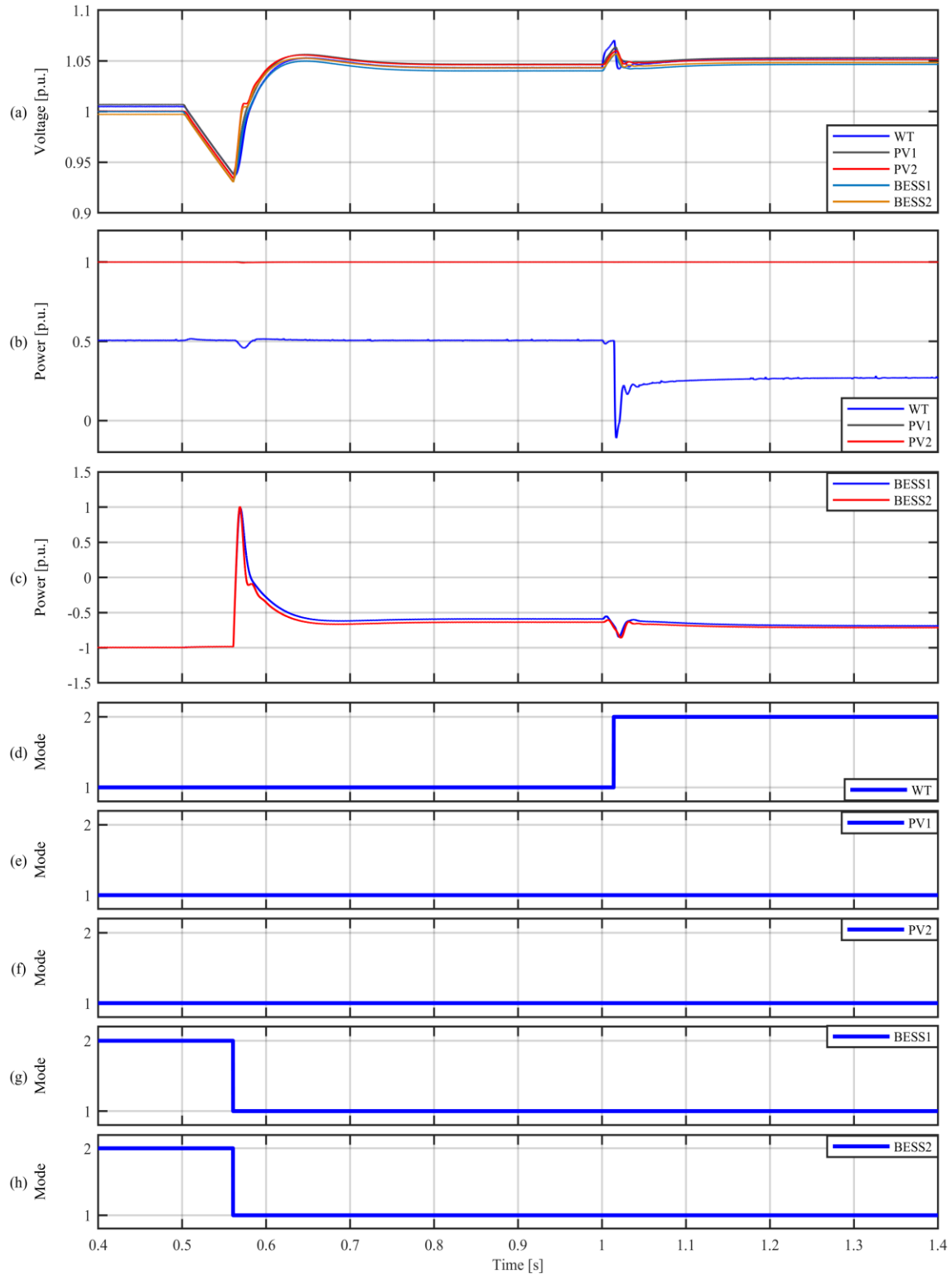


Figure 2.31: Performance of the conventional MADC strategy in the *Case Study 4*: (a) DER bus voltages, (b) RES powers, (c) BESS powers, (d) WT operation mode, (e) PV1 operation mode, (f) PV2 operation mode, (g) BESS1 operation mode, (h) BESS2 operation mode.

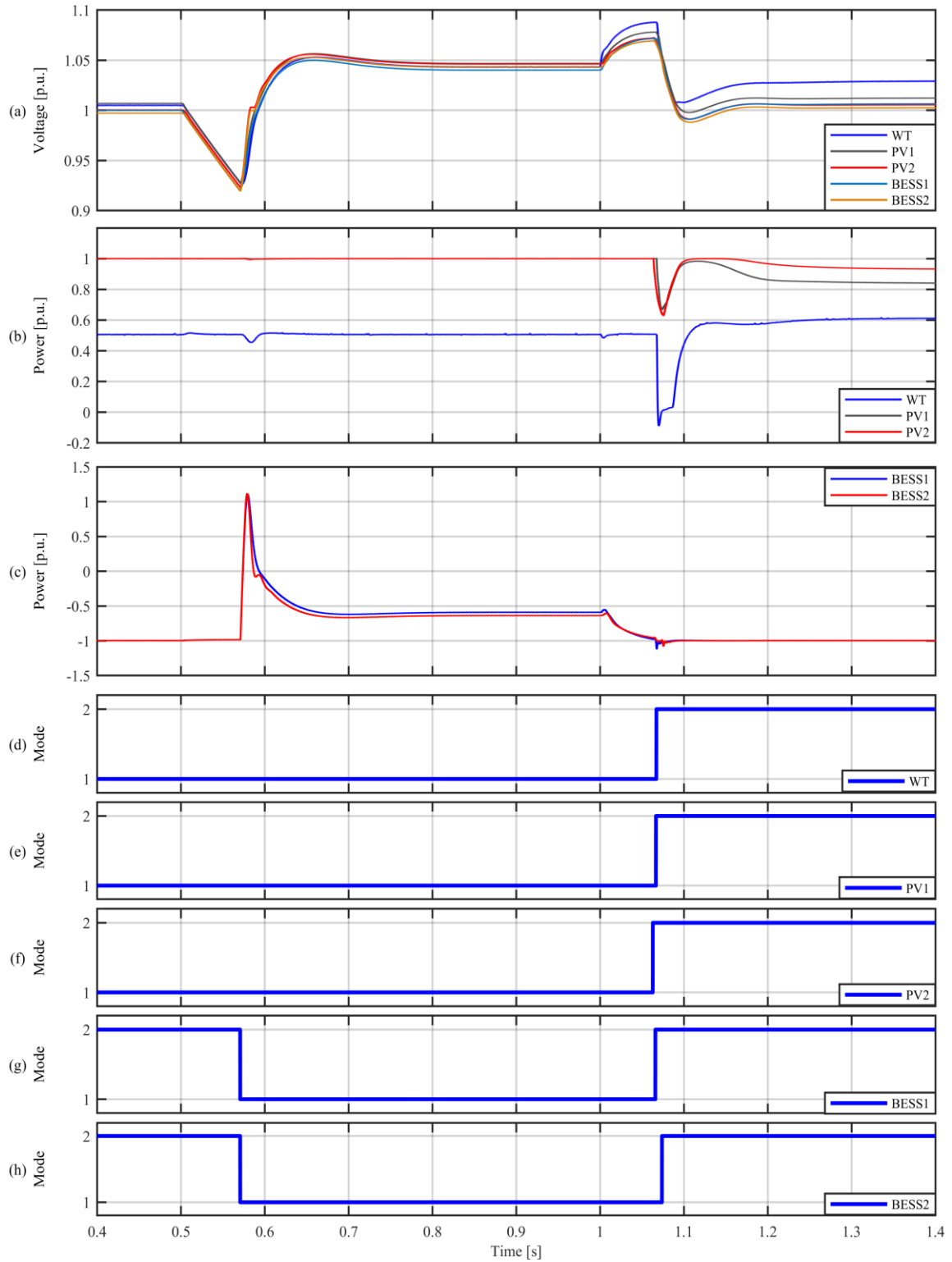


Figure 2.32: Performance of the improved MADC strategy in the *Case Study 4*: (a) DER bus voltages, (b) RES powers, (c) BESS powers, (d) WT operation mode, (e) PV1 operation mode, (f) PV2 operation mode, (g) BESS1 operation mode, (h) BESS2 operation mode.

As shown in Figure 2.31, after the islanding, the conventional MADC strategy enables both BESSs to change their operation modes to *Mode I*. The BESS1 and the BESS2 reduce their absorbed powers from 1 p.u. to 0.6 p.u. and 0.64 p.u., respectively, and regulate the DER bus voltages at values between 1.04 p.u. and 1.047 p.u. However, after the load disturbance (at $t > 1$ s), only the WT changes its operation mode to *Mode II*.

The WT reduces its output power from 0.5 p.u. to 0.27 p.u. and regulates the DER bus voltages at values between 1.046 p.u. and 1.053 p.u. After the load disturbance, the PVs and the BESSs fail to switch to *Mode II*, because their bus voltages do not reach the mode changing threshold V_{th2} . This issue adversely affects the power sharing between the DERs, because the PVs do not participate in maintaining the power balance, as shown in Figure 2.31(b). The study results shown in Figure 2.31 also indicate that the conventional MADC strategy leads to unnecessary curtailment of the renewable energy generated by the WT, since the batteries could absorb a larger amount of power (at $t > 1$ s).

Figure 2.32 shows that, before the load disturbance is applied at $t = 1$ s, the proposed improved MADC strategy operates similar to the conventional MADC strategy (both satisfactory). However, after the load disturbance, it provides a much more acceptable performance by enabling all DERs to switch their operation modes to *Mode II*. Using the proposed control strategy, in response to the power surplus at $t > 1$ s, both BESSs draw their maximum charging currents and all RESs participate in regulating the bus voltages by adjusting their output powers. The *Case study 4* highlights the capability of the proposed control strategy in maintaining the power balance in the microgrid, facilitating power sharing among the DERs, and maximizing the generated renewable energy, under successive disturbances that may have opposite effects.

Table 2.2 compares the mode switching performances of the conventional and improved MADC strategies under the *Case Studies 1-4*.

Table 2.2: Comparison of the conventional and improved MADC strategies.

Case Study	MADC Strategy	Time (s)	DER Voltages (p.u.)	WT Power (p.u.)	PV1 Power (p.u.)	PV2 Power (p.u.)	BESS1 Power (p.u.)	BESS2 Power (p.u.)
1	Conventional	$t < 0.5$	1.02-1.05	1	1	1	-1	-1
		$t \geq 0.5$	1.06	0.2	1	1	-1	-1
	Improved	$t < 0.5$	1.02-1.05	1	1	1	-1	-1
		$t \geq 0.5$	1.02-1.04	0.5	0.64	0.72	-1	-1
2	Conventional	$t < 0.5$	1.01-1.04	1	1	1	-1	-1
		$t \geq 0.5$	1.01-1.03	0.65	1	1	-1	-1
	Improved	$t < 0.5$	1.01-1.04	1	1	1	-1	-1
		$t \geq 0.5$	1-1.02	0.74	0.87	0.94	-1	-1
3	Conventional	$t < 0.5$	0.97-1.02	1	1	1	-1	-1
		$t \geq 0.5$	0.96-0.98	1	1	1	-1	0.42
	Improved	$t < 0.5$	0.97-1.02	1	1	1	-1	-1
		$t \geq 0.5$	1.02-1.04	1	1	1	-0.27	-0.25
4	Conventional	$t < 0.5$	1	0.5	1	1	-1	-1
		$t \geq 0.5$	1.04-1.047	0.5	1	1	-0.6	-0.64
		$t \geq 1$	1.046-1.053	0.27	1	1	-0.7	-0.72
	Improved	$t < 0.5$	1	0.5	1	1	-1	-1
		$t \geq 0.5$	1.04-1.047	0.5	1	1	-0.6	-0.64
		$t \geq 1$	1-1.03	0.6	0.84	0.93	-1	-1

2.4.3.5 Case Study 5

The fifth case study investigates and compares the performances of the proposed MADC and DBS control strategies under the same scenario as in Section 2.3.4.1. In this case study, the total power demand of the loads is reduced and the grid-connected DC microgrid has to handle the resulting large power surplus.

As shown in Figure 2.33, with the DBS control strategy, before $t = 1$ s, the grid-connected DC microgrid is in steady-state, and the DER terminal voltages are between 1.01 and 1.045 p.u. The WT, PV1 and PV2 operate in MPPT mode and generate 1, 0.5 and 0.5 MW power, respectively, while the total power demand is 1.31 MW. The BESS1 and BESS2 draw 0.04 and 0.1 MW power, respectively, and the GTC exports 0.47 MW power to the AC grid in order to maintain the power balance.

At $t = 1$ s, the total power demand is reduced to 0.69 MW, which leads to voltage rise in the entire DC microgrid, as shown in Figure 2.33 (a). Therefore, the GTC and BESSs start to absorb larger amount of power from the DC microgrid to maintain the power

balance and limit the voltage rise. At $t = 1.5$ s, the total power demand is further reduced to 0.05 MW (almost no load), which causes the DER voltages to rise again. The GTC reaches its power limit by exporting 1 MW to the AC grid. Therefore, the power balance is achieved by increasing the powers drawn by the BESSs and curtailing the power generated by the WT. As shown in Figure 2.33, the DBS control strategy effectively regulates the DC bus voltages and provides acceptable dynamic performance under the maximum power surplus in the grid-connected microgrid. The main shortcoming of the DBS control strategy in this case study is the fact that it causes unnecessary curtailment of the renewable power generation (Figure 2.33 (b)) and reduced energy storage by the BESSs (Figure 2.33 (c)) that are expected to remain in the full-power charging mode in the grid-connected DC microgrid. The DC microgrid power balance could be restored by increasing the charging currents of the BESSs, without curtailing the WT output power.

As shown in Figure 2.34, with the proposed MADC strategy, before $t = 1$ s, the grid-connected DC microgrid is in steady-state, and the DER terminal voltages are between 1 and 1.025 p.u. The WT, PV1 and PV2 operate in MPPT mode and generate 1, 0.5 and 0.5 MW power, respectively, while the power demand is 1.31 MW. Both BESSs draw their maximum power, i.e. 0.4 MW, and the GTC imports 0.13 MW power from the AC grid.

At $t = 1$ s, the total power demand is reduced to 0.69 MW, which leads to voltage rise in the entire DC microgrid, as shown in Figure 2.34 (a). The GTC exports 0.48 MW power to the AC grid to maintain the power balance and limit the voltage rise. Therefore, the DER terminal voltages increase to values between 1 and 1.043 p.u. At $t = 1.5$ s, the total power demand is further reduced to 0.05 MW (almost no load), which makes the DER voltages to rise again. The GTC exports 1.1 MW power to the AC grid to maintain the power balance and limit the voltage rise. Therefore, the DER terminal voltages increase to values between 1 and 1.06 p.u.

As shown in Figure 2.34, the proposed MADC strategy effectively regulates the DC bus voltages without unnecessarily curtailing the renewable power generation. Moreover, all RESs and BESSs operate in the intended modes, i.e. MPPT and charging, respectively, while GTC regulates the bus voltages of the grid-connected DC microgrid.

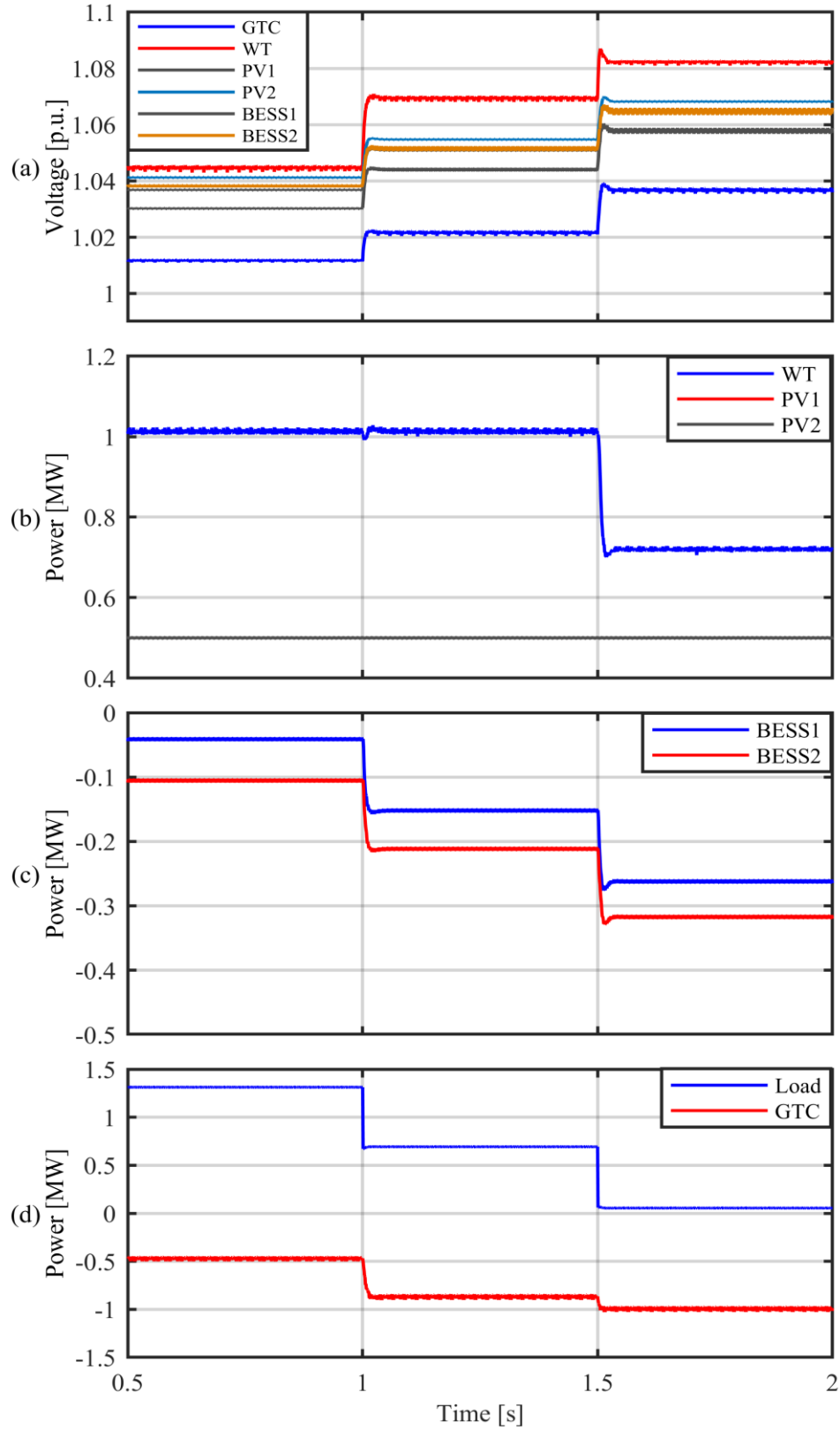


Figure 2.33: Performance of the DBS control strategy in *Case Study 5*: (a) DER bus voltages, (b) RES powers, (c) BESS powers, (d) GTC and load powers.

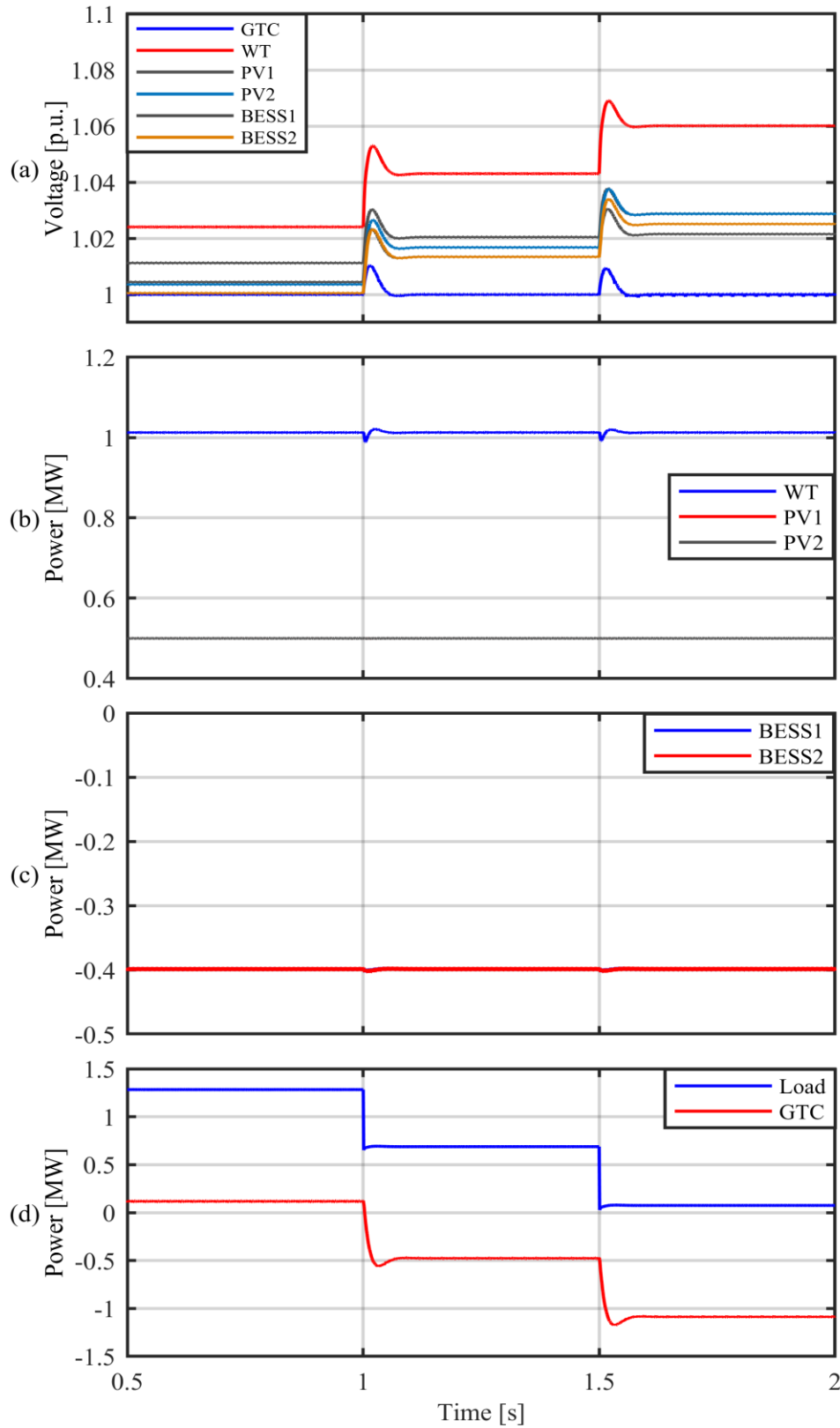


Figure 2.34: Performance of the proposed MADC strategy in *Case Study 5*: (a) DER bus voltages, (b) RES powers, (c) BESS powers, (d) GTC and load powers.

2.5 Conclusions

This chapter proposes improved DBS and MADC strategies for the DC microgrid. The performances of the proposed DBS and MADC strategies are investigated and verified under various operating conditions and disturbance scenarios in both grid-connected and islanded operation modes of the DC microgrid. The results of comprehensive studies conducted on a detailed study system indicate that the proposed DBS control strategy: (i) effectively maintains the power balance in the DC microgrid by properly and quickly changing the voltage-power characteristics of the DERs and the GTC, (ii) effectively limits the DC bus voltage deviations to 0.1 p.u. under large disturbances, (iii) realizes smooth transitions between different operation states, and (iv) provides acceptable dynamic response to disturbances.

The study results also indicate that the proposed MADC strategy (i) effectively maintains the power balance in the DC microgrid, (ii) effectively regulates the DC bus voltages under various operating conditions, by properly switching the operation modes of the DERs, (iii) improves power sharing between the DERs, (iv) significantly reduces the circulating currents between the DERs in the islanded microgrid, and (v) enables reliable and coordinated operation of the DERs, regardless of how fast the bus voltages change in response to disturbances.

The proposed DBS control strategy provides better dynamic response to disturbances, since it does not cause extra delay in the DER mode. Thus, it is more suitable for application in relatively small-scale microgrids, where the voltage drops caused by the line resistances are negligible and all the DERs and the GTC measure equal bus voltages. On the other hand, the MADC provides better power sharing performance, and is more suitable for application in large-scale DC microgrids with multiple geographically dispersed DERs, where the voltage drops caused by the line resistances are not negligible.

Chapter 3

3 Existing Load Shedding Schemes

3.1 Introduction

This chapter investigates and compares the performances of the existing non-communication based load shedding schemes in the DC microgrid. The non-communication based load shedding schemes that have been proposed in the literature for DC microgrid applications include voltage-based [32], [43], [70]-[72], timer-based [42], and combined [44], [51], [73] schemes. The following sections briefly describe these load shedding schemes.

3.1.1 Voltage-based Load Shedding Scheme

The voltage-based load shedding scheme [32], [43], [70]-[72] utilizes different voltage thresholds to prioritize non-critical loads and instantaneously sheds the i^{th} non-critical load whenever the voltage seen by that load falls below the corresponding voltage threshold V_{th-i} . The loads with lower priorities are assigned higher voltage thresholds and thus are shed faster. The flowchart, block diagram, and operating characteristic of the voltage-based load shedding scheme are shown in Figures 3.1 (a)-(c), respectively.

3.1.2 Timer-based Load Shedding Scheme

The timer-based load shedding scheme [42] utilizes a common voltage threshold, and prioritizes the non-critical loads using different time delays. This strategy sheds the i^{th} non-critical whenever its voltage remains below the common threshold V_{th} for a time period longer than the corresponding time delay T_i . The loads with lower priorities are assigned lower time delays and thus are shed faster. The flowchart, block diagram, and operating characteristic of the timer-based load shedding scheme are shown in Figures 3.2 (a)-(c), respectively.

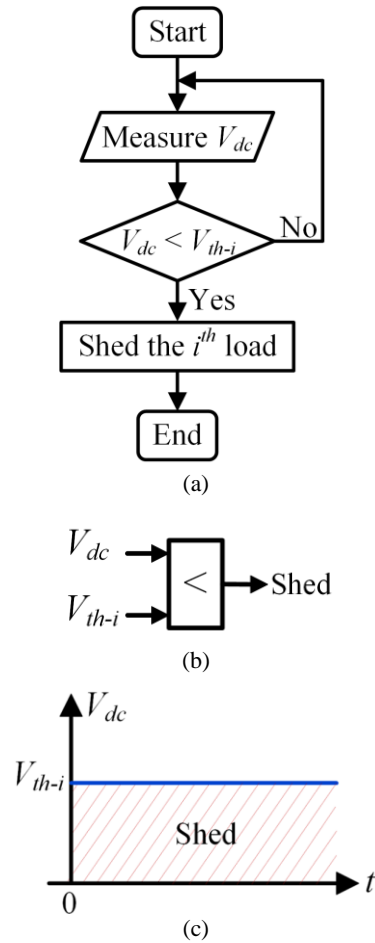


Figure 3.1: The voltage-based load shedding scheme: (a) flowchart, (b) block diagram, (c) operating characteristic.

3.1.3 Combined Load Shedding Scheme

The combined load shedding scheme [44], [51], [73] utilizes both voltage-based and timer-based algorithms and thus operates whenever either of these two schemes operate. Two different voltage thresholds are used for each load. The load-specific voltage thresholds V_{th-i} are used for instantaneously shedding the corresponding loads, similar to the voltage-based scheme. In addition, the i^{th} load is shed when the voltage seen by that load remains below the common threshold V_{th} for a time period longer than the corresponding time delay T_i . The loads with lower priorities are assigned higher load-specific voltage thresholds and shorter time delays, and thus are shed faster. The flowchart, block diagram, and operating characteristic of the combined load shedding scheme are shown in Figures 3.3 (a)-(c), respectively.

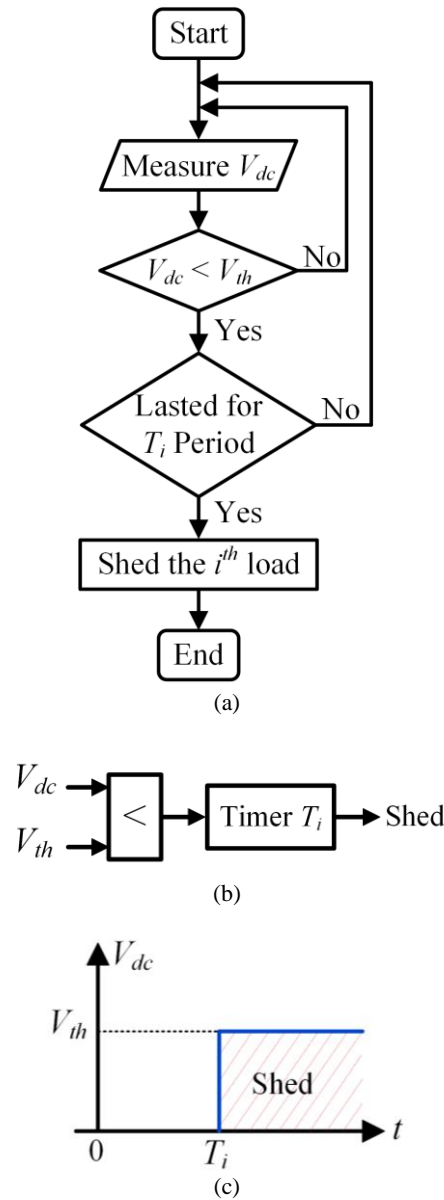


Figure 3.2: The timer-based load shedding scheme: (a) flowchart, (b) block diagram, (c) operating characteristic.

3.2 Performance Evaluation

This section investigates and compares the performances of the three load shedding schemes described in Sections 3.1. Comprehensive time-domain simulation studies are conducted in the PSCAD software environment using the DC microgrid study system as shown in Figure 3.4. The shaded area in Figure 3.4 contains the non-critical loads. Three fast-acting solid-state circuit breakers (CBs) are used for a three-step load shedding. As

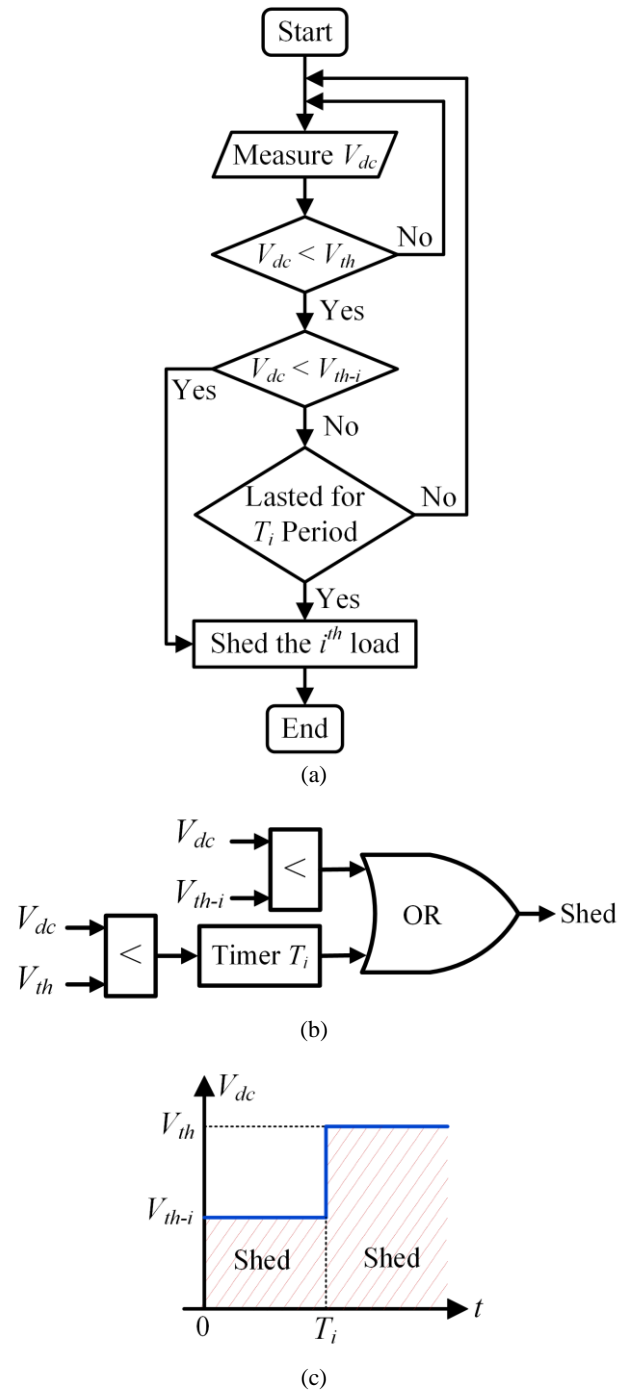


Figure 3.3: The combined load shedding scheme: (a) flowchart, (b) block diagram, (c) operating characteristic.

shown in Figure 3.4, tripping each of the CBs results in shedding a group of downstream loads. Whenever there is a need for load shedding, the CB1 should be tripped first. The next step is tripping CB2. Tripping the CB3 is the last step. The amounts of non-critical loads that are shed in each step are 126.5, 126, and 218 kW, respectively.

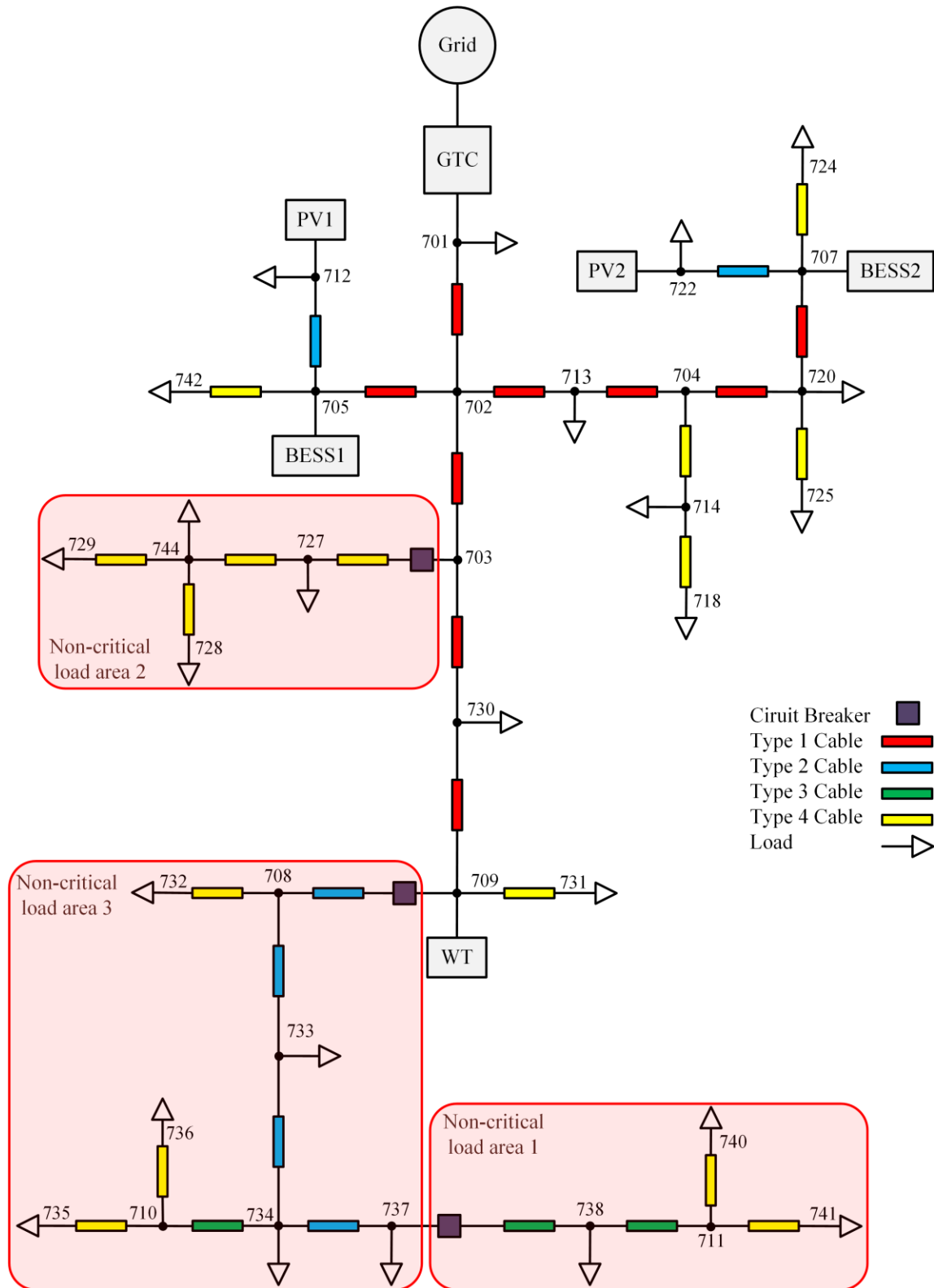


Figure 3.4: Single-line diagram of the study system.

Under normal operating conditions, the bus voltage deviations caused by voltage drop across the lines can be as high as ± 0.05 p.u. Thus, choosing load shedding voltage thresholds below 0.95 p.u. is recommended to avoid unnecessary load shedding. In microgrids with short lines, where the line voltage drops are lower than 0.05 p.u., a threshold closer to 1 p.u. can be chosen. In this study, the voltage drops across the lines are considerable. Therefore, the highest load shedding voltage threshold for all non-critical loads is set at 0.9 p.u. to prevent load shedding under normal operating conditions.

The performance evaluation criteria are (i) avoiding over-shedding, i.e., maintaining power balance by disconnecting the minimum amount of loads, and (ii) limiting the magnitudes and durations of voltage sags through sufficiently fast load shedding. Since the node 702 is at the center of the area containing the critical loads, the variations of the voltage of that node is used as the indicator of the performances of both shedding schemes. This is done to avoid figures that would otherwise contain numerous waveforms corresponding to the voltages of all nodes. Hence, the study results presented in this section highlight the variations of the node 702 voltage and the voltages of the three groups of the non-critical loads, i.e., voltages at the terminals of CBs 1-3.

The following sub-sections investigate two disturbance scenarios in the islanded microgrid. The initial operating conditions ($t < 0.5$ s) are the same for all investigated disturbance scenarios. Before the disturbances are applied, the DC microgrid is islanded and the DC bus voltages at the load-side terminals of the CB1, CB2 and CB3 are between 0.96 and 0.992 p.u. The RESs operate in the MPPT mode and generate 1 MW power, while the total power demand of the loads is 1.25 MW. The BESSs inject 0.3 MW into the DC microgrid to maintain the power balance and regulate the DC bus voltages.

3.2.1 Case Study 1

The first case study investigates the performances of the three load shedding schemes under a large generation disturbance, in the islanded mode. At $t = 0.5$, the total power generated by the WT instantaneously decreases from 1 to 0.15 MW. The BESSs attempt to maintain the power balance by injecting their maximum power, i.e., 0.8 MW, into the DC microgrid.

However, as the total power that can be provided by the DERs is smaller than the total power demand of the loads, the DC bus voltages start to fall.

3.2.1.1 Voltage-based Load Shedding Scheme

The voltage-based scheme trips the CBs 1-3 whenever the corresponding bus voltages fall below the thresholds V_{th1} , V_{th2} , and V_{th3} , respectively. The performance of the voltage-based scheme is investigated using two different sets of voltage thresholds. The first set of thresholds are $V_{th1} = 0.9$ p.u., $V_{th2} = 0.88$ p.u., and $V_{th3} = 0.86$ p.u., hereafter referred to as the *high thresholds*. The second set are the *low thresholds* $V_{th1} = 0.9$ p.u., $V_{th2} = 0.85$ p.u., and $V_{th3} = 0.8$ p.u.

Figure 3.5 shows the performance of the voltage-based scheme with high thresholds. Figure 3.5(a) shows the approximate voltage seen by the critical loads and the voltages seen by the non-critical loads. Figure 3.5(b) shows the total power demand of the loads in the microgrid. As shown in Figure 3.5(b), the voltage-based scheme with high thresholds sheds 0.51 MW non-critical loads by tripping the CB1, CB2, and CB3, at $t = 0.517$ s, 0.559 s, and 1.035 s, respectively. The third load shedding step is considerably delayed because the power mismatch in the microgrid becomes small after the second group of loads are shed. This causes the voltages to decrease at a low rate and reach the third threshold after about 0.5 s. Due to the delayed third load shedding step, the critical loads experience a voltage sag for a relatively long time (about 0.6 s), before the voltage is eventually restored to 0.94 p.u.

Figure 3.6 shows the performance of the voltage-based scheme with low thresholds. As shown in Figure 3.6(b), when lower thresholds are utilized, the voltage-based scheme sheds 0.31 MW non-critical loads by tripping the CB1, and CB2, at $t = 0.517$ s, and 0.59 s, respectively. Since the third group of the non-critical loads is not shed, the voltage seen by the critical loads remains at the relatively low value of 0.86 p.u., as illustrated in Figure 3.6(a). The study results shown in Figure 3.6 indicate that the voltage-based scheme may cause under-shedding and steady-state under-voltage conditions if the utilized voltage thresholds are too low.

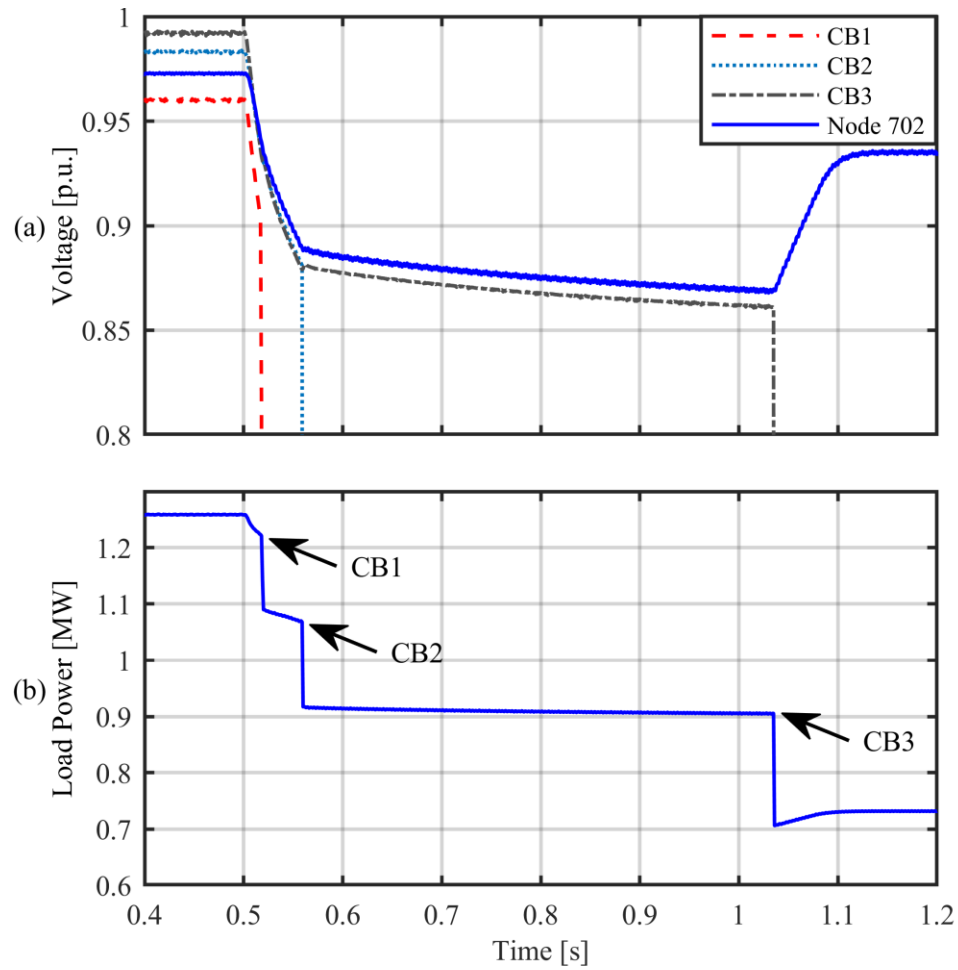


Figure 3.5: Performance of the voltage-based load shedding scheme with high thresholds in the *Case Study 1*: (a) DC voltages, (b) total load power.

The study results illustrated in Figures 3.5 and 3.6 indicate that higher voltage thresholds improve the voltage regulation performance of the voltage-based load shedding scheme. The length and magnitude of the voltage sag in Figure 3.5(a) could be further reduced by increasing the values of V_{th2} and V_{th3} to 0.89 and 0.88 p.u., respectively. However, using voltage thresholds that are too close to each other may result in shedding an unnecessarily large amount of loads due to voltage ripples and measurement errors. Hence, utilizing the voltage-based load shedding scheme requires a compromise between the voltage regulation performance and the power supply reliability.

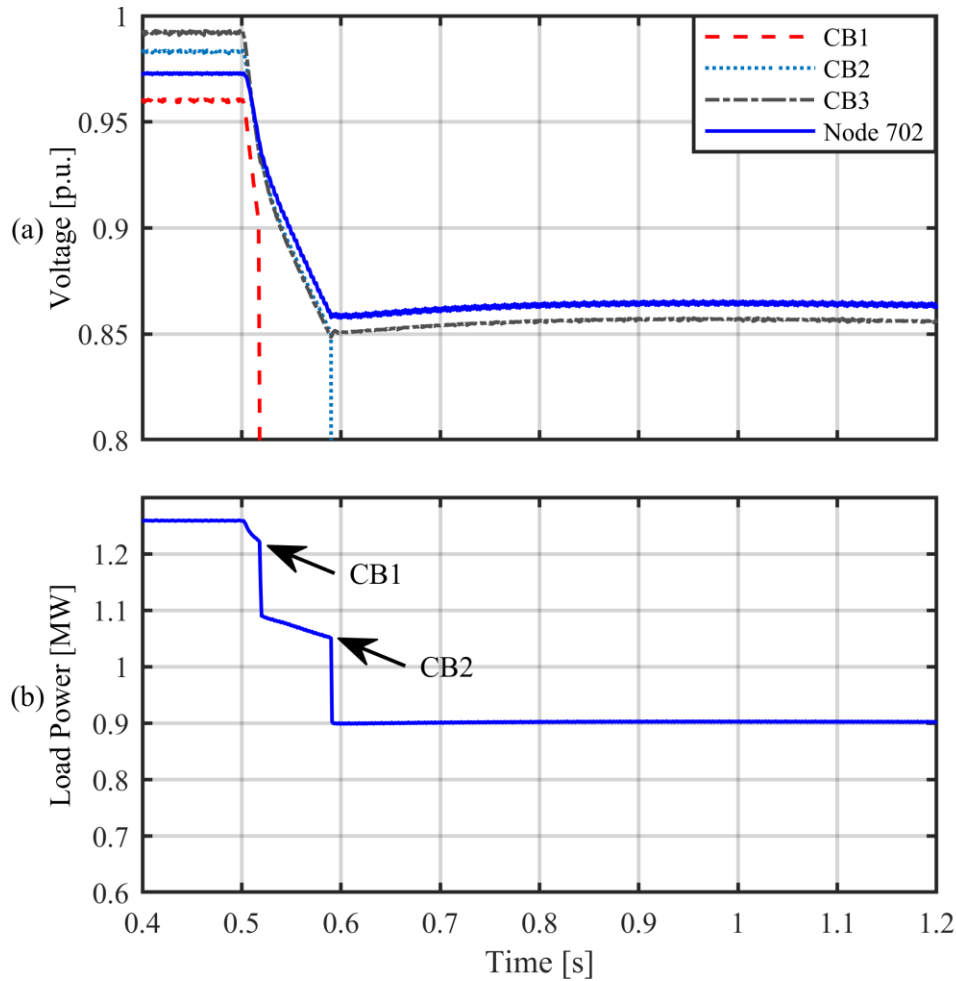


Figure 3.6: Performance of the voltage-based load shedding scheme with low thresholds in the *Case Study 1*: (a) DC voltages, (b) total load power.

3.2.1.2 Timer-based Load Shedding Scheme

The timer-based scheme trips the CBs 1-3 whenever the corresponding bus voltages remain below the common voltage threshold V_{th} for time periods longer than the delays T_1 , T_2 , and T_3 , respectively. The performance of the timer-based scheme is investigated using $V_{th} = 0.9$ p.u. and two different sets of time delays. The first set of delays are $T_1 = 10$ ms, $T_2 = 20$ ms, and $T_3 = 30$ ms, hereafter referred to as the *short delays*. The second set are the *long delays* $T_1 = 50$ ms, $T_2 = 100$ ms, and $T_3 = 150$ ms, which are five times longer than the *short delays*.

Figure 3.7 shows the performance of the timer-based load shedding scheme with short delays. As shown in Figure 3.7(b), the timer-based scheme with short delays sheds 0.51

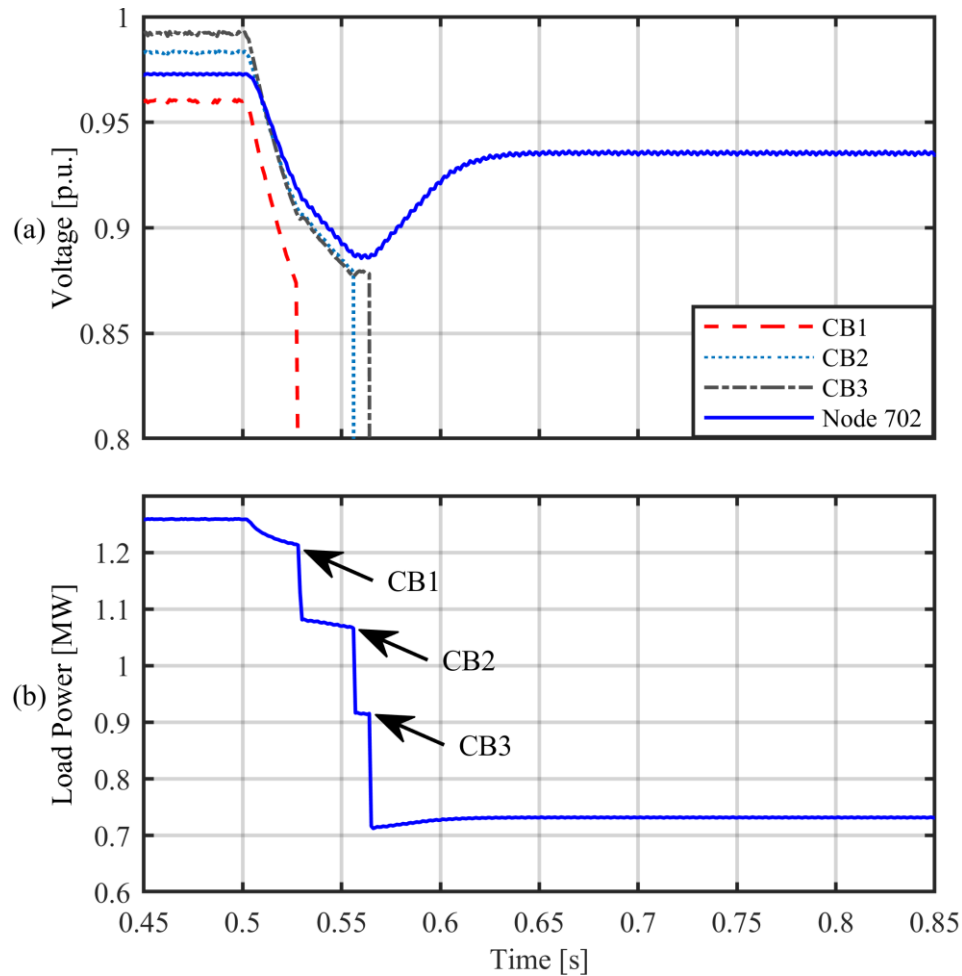


Figure 3.7: Performance of the timer-based load shedding scheme with short delays in the *Case Study 1*: (a) DC voltages, (b) total load power.

MW non-critical loads by tripping the CB1, CB2 and CB3 at $t = 0.527$ s, 0.556 s, and 0.564 s, respectively. As a result, the voltage seen by the critical loads is regulated at an acceptable level (0.94 p.u.) within a relatively short time (about 0.15 s) after the disturbance, as illustrated in Figure 3.7(a).

Figure 3.8 shows the performance of the timer-based scheme with long delays. Figure 3.8(b) shows that the non-critical loads are shed by tripping the CB1, CB2 and CB3 at $t = 0.567$ s, 0.632 s, and 0.68 s, respectively. Figure 3.8(a) illustrates that the longer delays cause the critical loads to experience a considerably larger voltage sag for a longer time period.

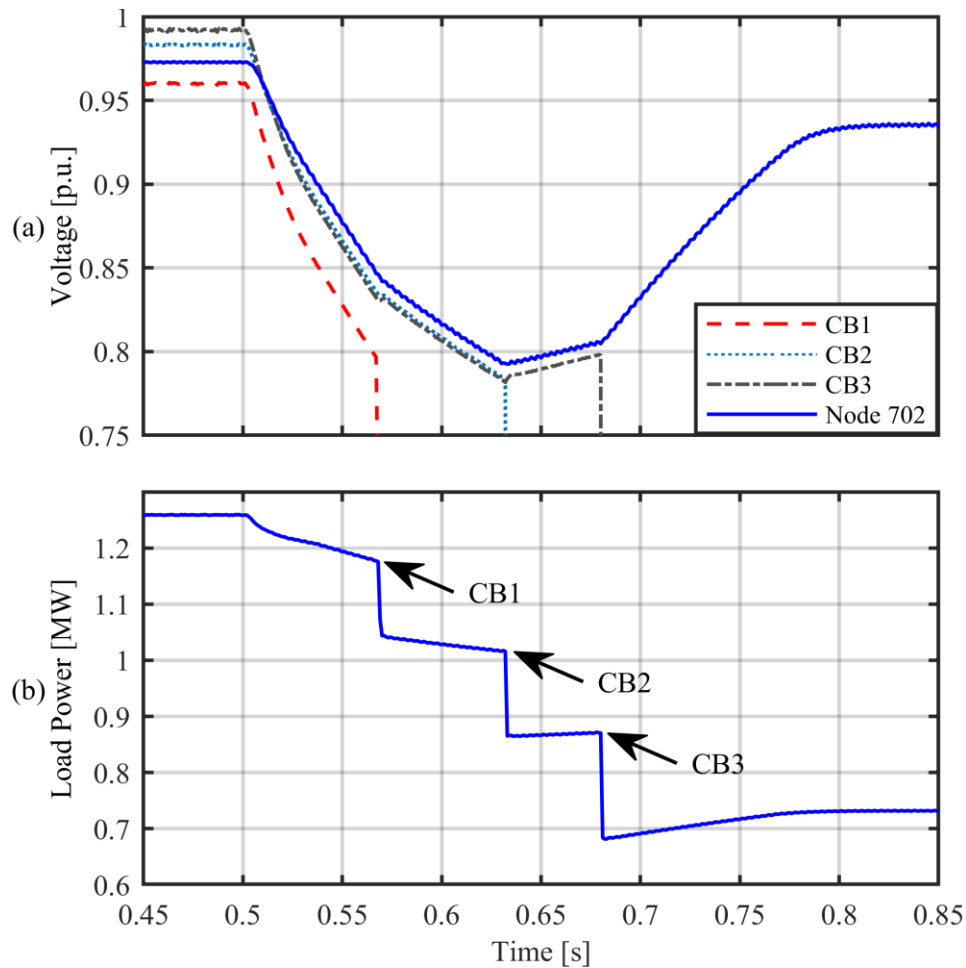


Figure 3.8: Performance of the timer-based load shedding scheme with long delays in the Case Study 1: (a) DC voltages, (b) total load power.

Figures 3.7 and 3.8 indicate that the timer-based scheme can effectively limit the magnitude and time duration of the voltage sags, if sufficiently short time delays are used. Using excessively short delays may cause unnecessary load shedding, if the bus voltages fall below the common voltage threshold even for a short time. On the other hand, using long delays adversely affects the voltage regulation performance by causing delayed voltage restoration. Thus, utilizing the timer-based scheme necessitates a compromise between the voltage regulation performance and the power supply reliability.

3.2.1.3 Combined Load Shedding Scheme

The combined load shedding scheme trips the CBs 1-3 whenever the corresponding bus voltages (i) fall below the thresholds $V_{th1} = 0.9$ p.u., $V_{th2} = 0.88$ p.u., and $V_{th3} = 0.86$ p.u.,

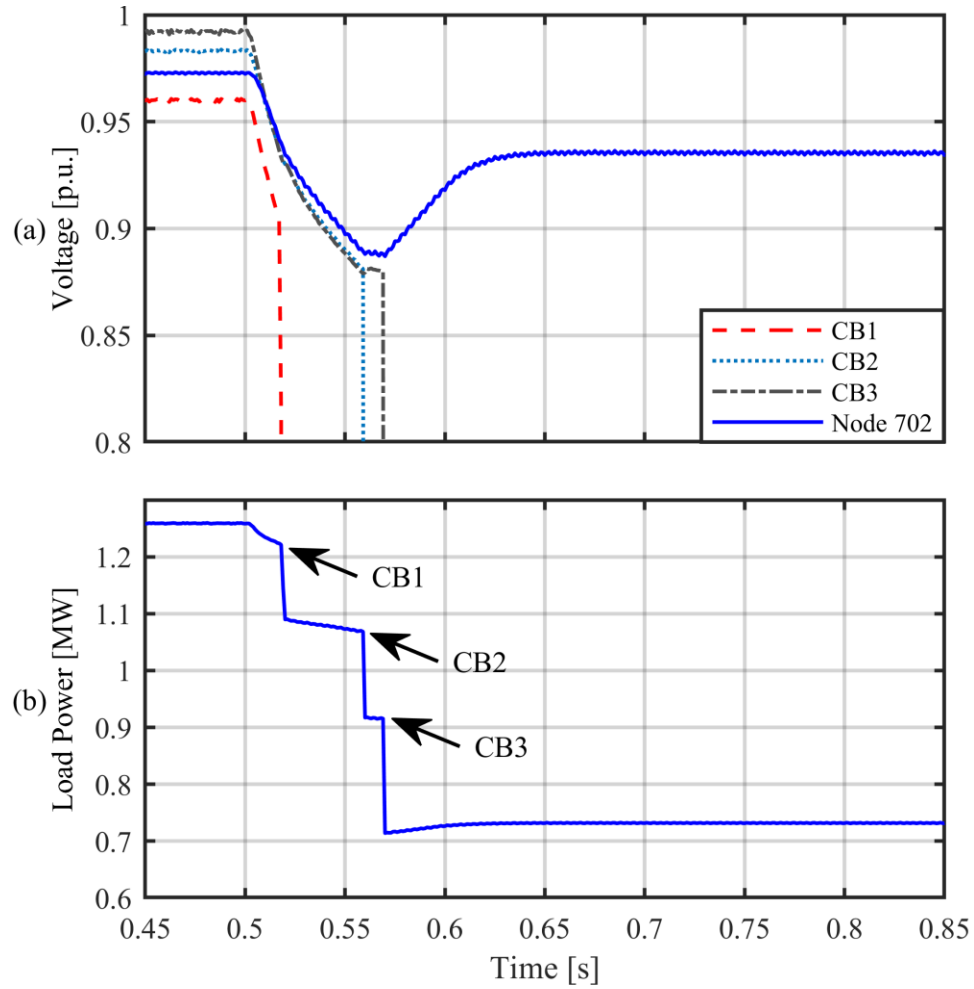


Figure 3.9: Performance of the combined load shedding scheme in the *Case Study 1*: (a) DC voltages, (b) total load power.

respectively, or (ii) remain below the common voltage threshold $V_{th} = 0.9$ p.u. for time periods longer than $T_1 = 10$ ms, $T_2 = 20$ ms, and $T_3 = 30$ ms, respectively. Figure 3.9 shows the performance of the combined load shedding scheme under the disturbance scenario of the *Case Study 1*. As shown in Figure 3.9(b), the combined scheme sheds 0.51 MW non-critical loads by tripping the CB1, CB2, and CB3 at $t = 0.517$ s, 0.559 s, and 0.569 s, respectively. As a result, the voltage seen by the critical loads is regulated at 0.94 p.u. within a relatively short time (0.15 s) after the disturbance, as illustrated in Figure 3.9(a). Figure 3.9 shows that the combined load shedding scheme does not suffer from the voltage sag issue of the voltage-based scheme.

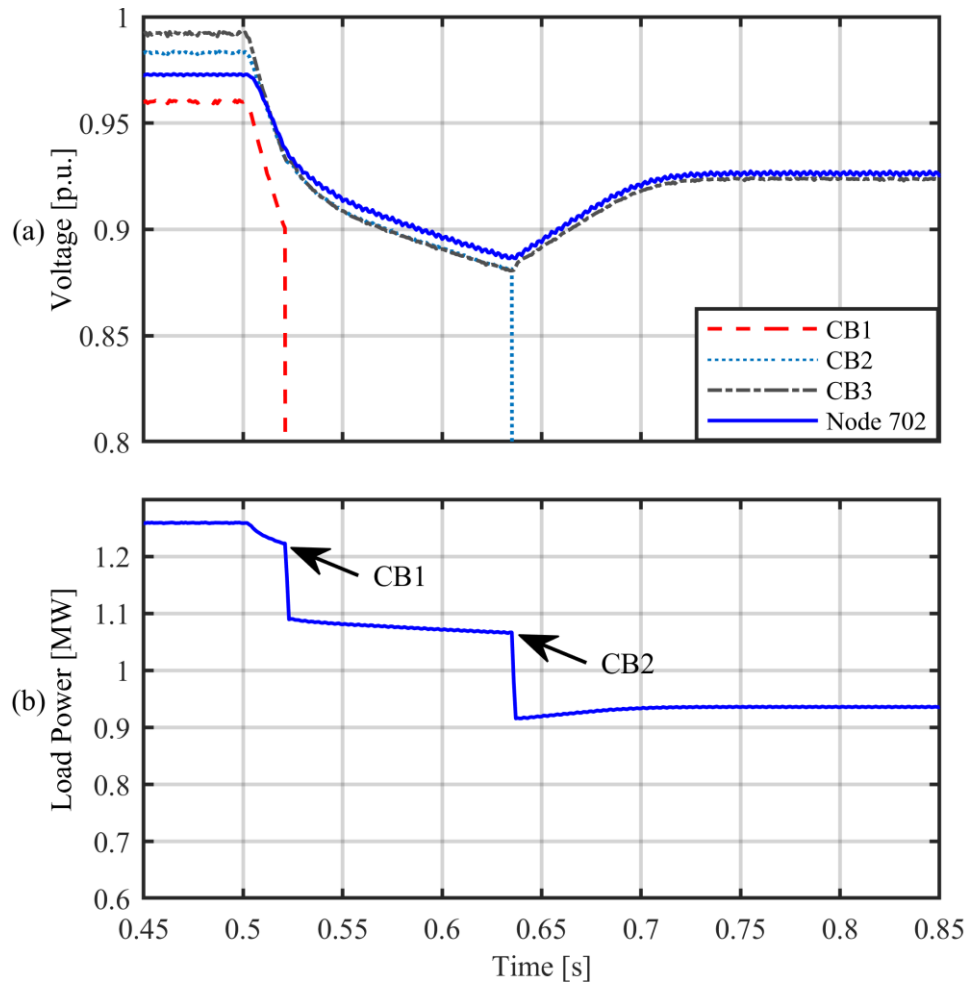


Figure 3.10: Performance of the voltage-based load shedding scheme with high thresholds in the *Case Study 2*: (a) DC voltages, (b) total load power.

3.2.2 Case Study 2

This case study represents a less severe generation disturbance in the islanded mode. At $t = 0.5$ s, the total power generated by the WT instantaneously decreases from 1 to 0.25 MW. The following three parts investigate the performances of the three load shedding schemes under this disturbance.

3.2.2.1 Voltage-based Load Shedding Scheme

Figure 3.10 shows the performance of the voltage-based load shedding scheme with high thresholds. As shown in Figure 3.10(b), adopting the high thresholds leads to shedding 0.31 MW non-critical loads by tripping the CB1 and CB2 at $t = 0.521$ s and 0.635 s, respectively.

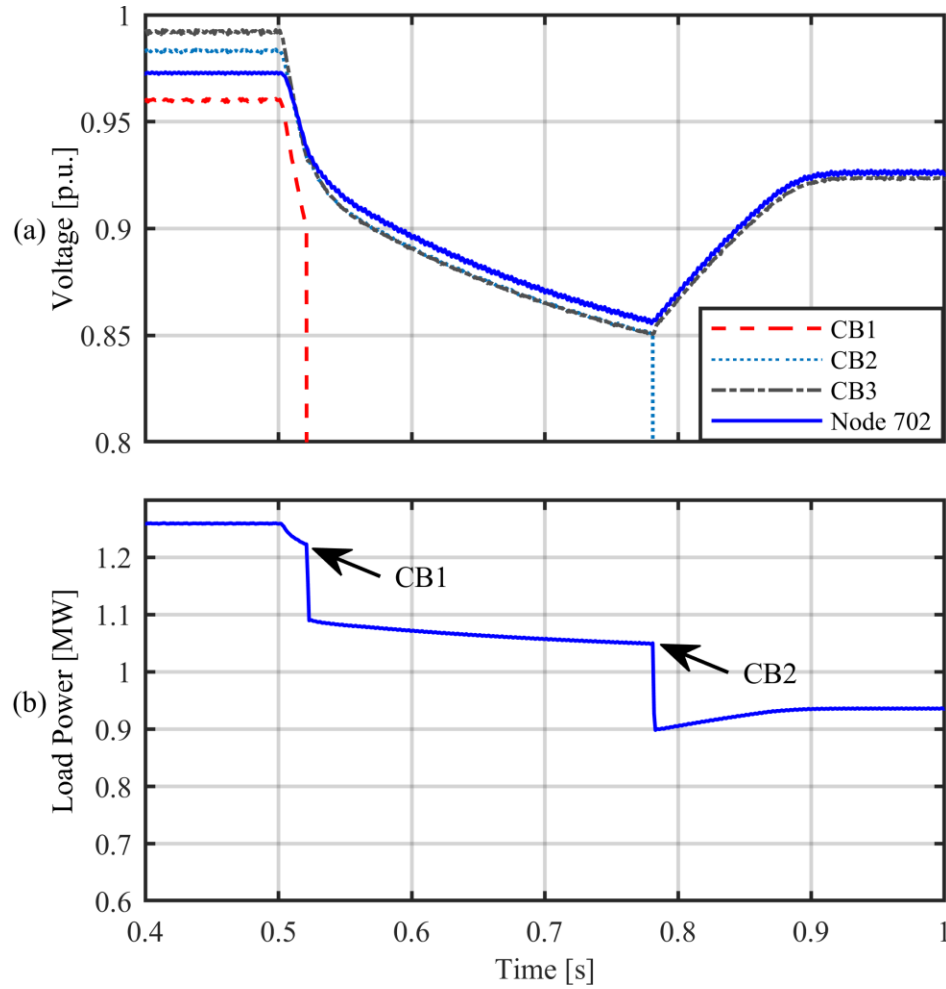


Figure 3.11: Performance of the voltage-based load shedding scheme with low thresholds in the *Case Study 2*: (a) DC voltages, (b) total load power.

The steady-state voltage seen by the critical loads is regulated at 0.925 p.u. within 0.25 s after the disturbance, as illustrated in Figure 3.10(a). Besides, the minimum instantaneous voltage experienced by the critical loads is 0.88 p.u. Figure 3.10 shows that shedding the first two groups of the non-critical loads is sufficient to restore the bus voltages to acceptable values, after the disturbance of the *Case Study 2*.

Figure 3.11 shows the performance of the voltage-based scheme with low thresholds. Figure 3.11(b) illustrates that 0.31 MW non-critical loads are shed by tripping the CB1 and CB2 at $t = 0.521$ s and 0.781 s, respectively. The voltage seen by the critical loads temporarily falls to 0.86 p.u. and is regulated at 0.925 p.u. within about 0.4 s after the disturbance.

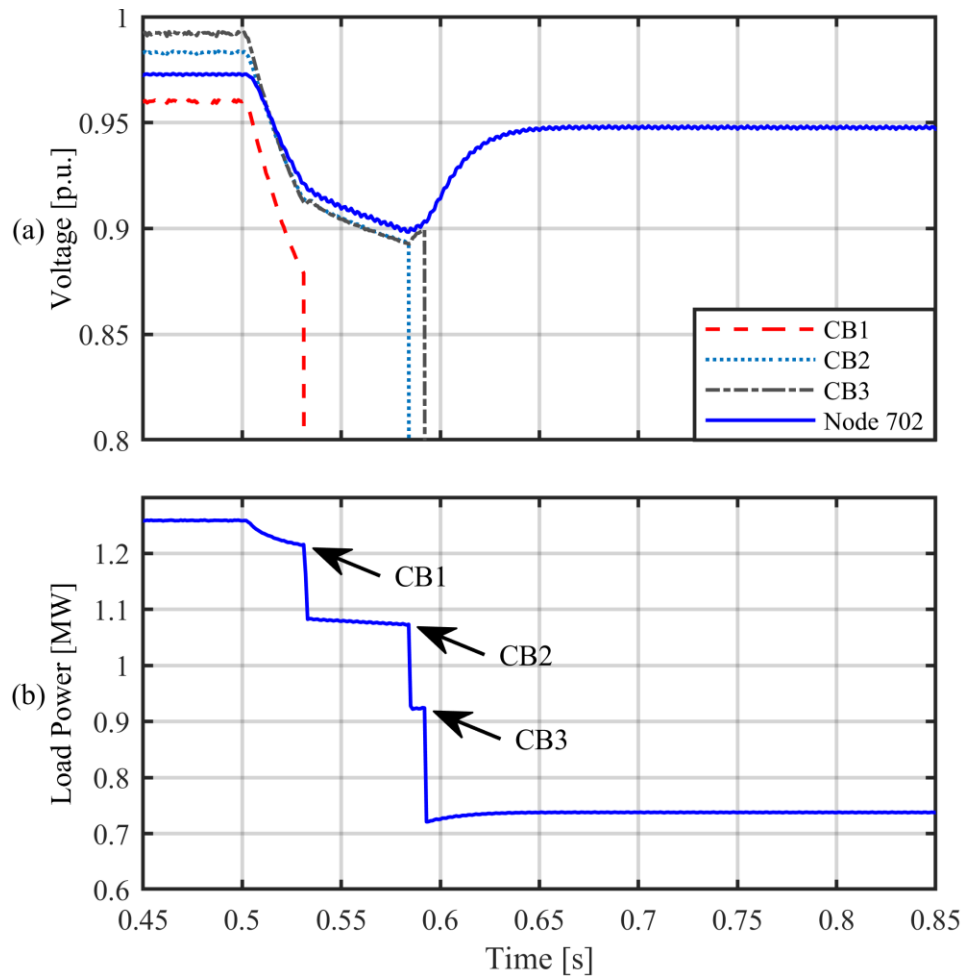


Figure 3.12: Performance of the timer-based load shedding scheme with short delays in the *Case Study 2*: (a) DC voltages, (b) total load power.

The study results shown in Figures 3.5, 3.6, 3.10, and 3.11 indicate that, even with high thresholds, the voltage-based load shedding scheme results in delayed voltage restoration.

3.2.2.2 Timer-based Load Shedding Scheme

Figure 3.12 shows the performance of the timer-based load shedding scheme with short delays. The short delays cause shedding 0.51 MW non-critical loads by tripping the CB1, CB2 and CB3 at $t = 0.531$ s, 0.584 s, and 0.592 s, respectively. Consequently, the voltage seen by the critical loads is regulated at 0.95 p.u. within 0.15 s after the disturbance, Figure 3.12(a).

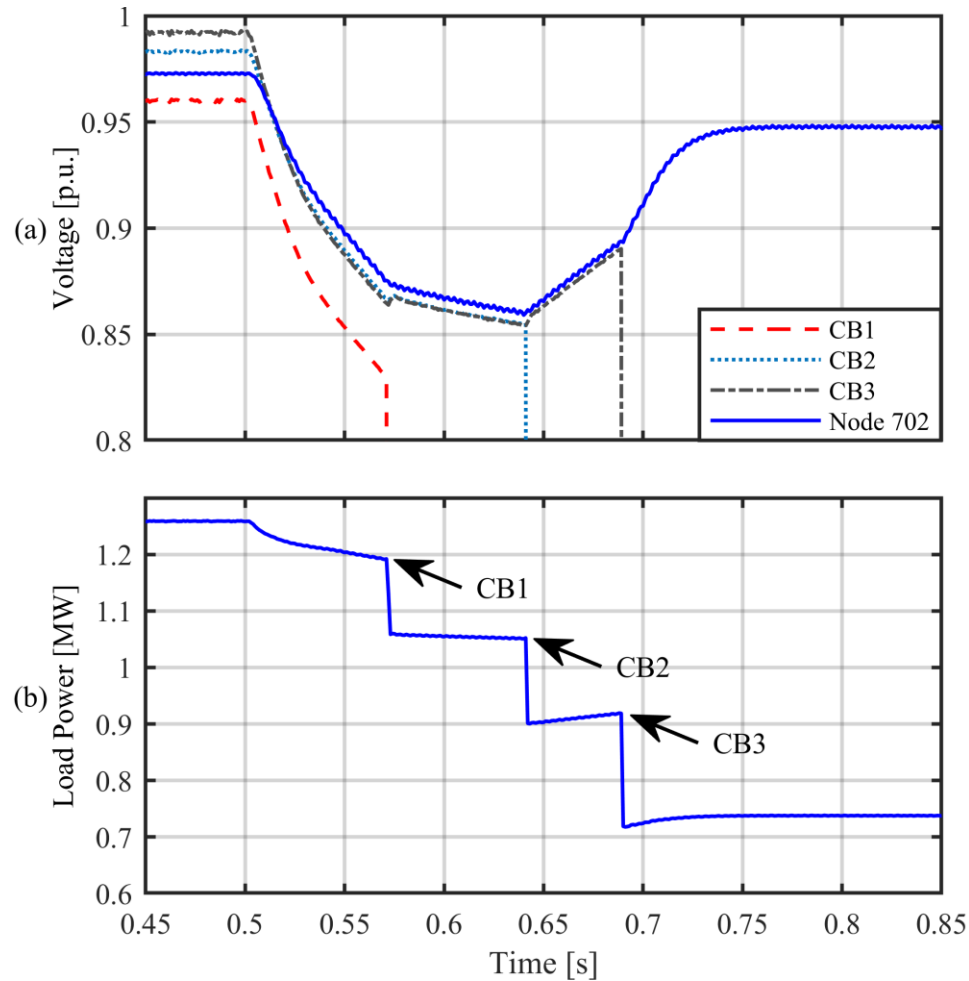


Figure 3.13: Performance of the timer-based load shedding scheme with long delays in the *Case Study 2*: (a) DC voltages, (b) total load power.

Figure 3.13 illustrates the performance of the timer-based load shedding scheme with long delays. Figure 3.13(b) shows that the non-critical loads are shed by tripping the CB1, CB2 and CB3 at $t = 0.571$ s, 0.641 s, and 0.689 s, respectively. Figure 3.13(a) shows that longer delays cause the critical loads to experience a considerably larger voltage sag for a longer time period.

Figures 3.7, 3.8, 3.12, and 3.13 illustrate that shorter time delays generally improve the voltage regulation performance of the timer-based scheme. In addition, comparing the results shown in Figures 3.10 and 3.11 with those shown in Figures 3.12 and 3.13 indicates that the third step of load shedding performed by the timer-based scheme in the *Case Study 2* is not necessary. It is also evident from the results that utilizing longer time delays does

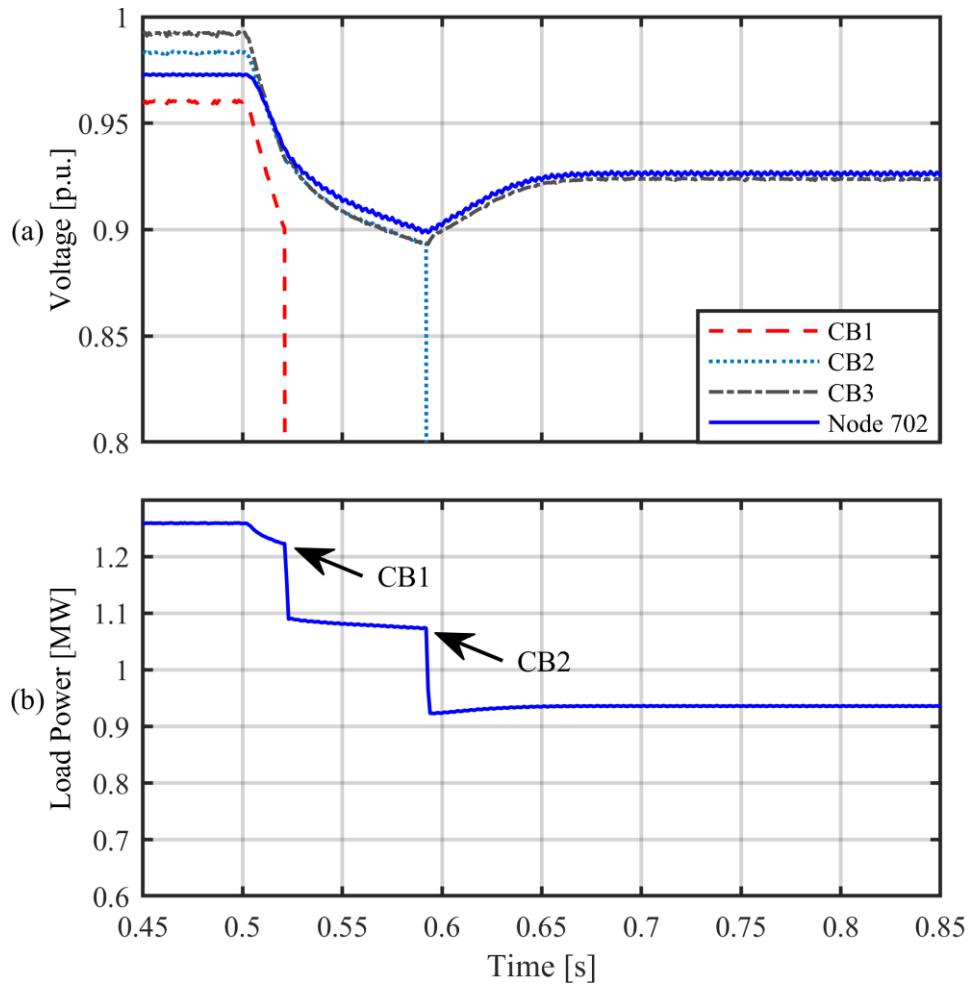


Figure 3.14: Performance of the combined load shedding scheme in the *Case Study 2*: (a) DC voltages, (b) total load power.

not necessarily prevent the potential over-shedding issue of the timer-based scheme.

3.2.2.3 Combined Load Shedding Scheme

Figure 3.14 shows the performance of the combined load shedding scheme. As shown in Figure 3.14(b), the combined scheme sheds 0.31 MW non-critical loads by tripping the CB1 and CB2 at $t = 0.521$ s, and 0.592 s, respectively. The voltage seen by the critical loads is regulated at 0.925 p.u. within a relatively short time (0.15 s) after the disturbance, as illustrated in Figure 3.14(a). In addition, the voltage seen by the critical loads does not fall below 0.9 p.u. in this case study. Figure 3.14 illustrates that the combined load shedding scheme does not suffer from the over-shedding issue of the timer-based scheme, i.e., prevents the unnecessary third load shedding.

Table 3.1: Comparison of the non-communication based load shedding schemes

Case Study	Load Shedding Scheme	V_{min} (p.u.)	Voltage sag duration (s)	Restored voltage (p.u.)	Trip Time (s)			Issue
					CB1	CB2	CB3	
1	Voltage-based scheme with high thresholds	0.87	0.5	0.94	0.517	0.559	1.035	Delayed restoration
	Voltage-based scheme with low thresholds	0.86	Indefinite	0.86	0.517	0.59	-	Under-shedding
	Timer-based scheme with short delays	0.885	0.15	0.94	0.527	0.556	0.564	-
	Timer-based scheme with long delays	0.79	0.3	0.94	0.567	0.632	0.68	Large voltage sag
	Combined scheme	0.885	0.15	0.94	0.517	0.559	0.569	-
2	Voltage-based scheme with high thresholds	0.885	0.25	0.925	0.521	0.635	-	-
	Voltage-based scheme with low thresholds	0.86	0.4	0.925	0.521	0.781	-	Delayed restoration
	Timer-based scheme with short delays	0.9	0.15	0.95	0.531	0.584	0.592	Over-shedding
	Timer-based scheme with long delays	0.86	0.25	0.95	0.571	0.641	0.689	Over-shedding
	Combined scheme	0.9	0.15	0.925	0.521	0.592	-	-

The results of the *Case Studies 1* and *2* are summarized in Table 3.1, where V_{min} denotes the minimum value of the critical load voltage.

3.3 Conclusions

In this chapter, the performances of the existing non-communication based load shedding schemes are investigated and compared in DC microgrid. The study results indicate that:

- The voltage-based scheme provides higher power supply reliability as compared with the timer-based scheme, but suffers from poor voltage regulation performance.
- The timer-based load shedding scheme may cause over-shedding of the loads, which degrades the power supply reliability, but provides desirable voltage regulation performance if short delays are utilized.
- In terms of steady-state voltage restoration, i.e., preventing under-shedding, the timer-based scheme is more effective than the voltage-based scheme.
- Determining the parameters, i.e., voltage thresholds and time delays, of the voltage-based and timer-based schemes necessitates a compromise between the voltage regulation performance and the power supply reliability.
- The combined scheme improves the voltage regulation performance by reducing the magnitudes and time durations of the voltage sags experienced by the critical loads.
- The combined load shedding scheme increases the reliability of the power supplied to the loads by preventing over-shedding.

Chapter 4

4 Proposed Load Shedding Schemes

4.1 Introduction

This chapter proposes adaptive voltage- and timer-based load shedding schemes utilizing voltage thresholds and time delays that are automatically adjusted depending on the rate of change of locally measured bus voltages. The performance of the proposed load shedding schemes are investigated and compared with those of the conventional voltage- and timer-based load shedding schemes, under various disturbances. Comprehensive time-domain simulation studies are conducted using the DC microgrid study system of Figure 3.4 in the PSCAD/EMTDC software.

4.2 Adaptive Voltage-based Load Shedding Scheme

4.2.1 Introduction

In this section, an adaptive voltage-based load shedding scheme is proposed for the DC microgrid. The proposed load shedding scheme utilizes an adaptive voltage threshold V_{th} that depends on the ROCOV, as defined by:

$$V_{th} = \begin{cases} V_{min} & , \quad -k_1 < \frac{dV_{dc}}{dt} \leq 0 \\ V_{min} + m \left(\frac{dV_{dc}}{dt} + k_1 \right) & , \quad -k_2 \leq \frac{dV_{dc}}{dt} \leq -k_1 \\ V_{max} & , \quad -\infty < \frac{dV_{dc}}{dt} < -k_2 \end{cases} \quad (4.1)$$

where

$$m = \frac{V_{max} - V_{min}}{k_1 - k_2} \quad (4.2)$$

and V_{min} and V_{max} are the minimum and maximum values of the adaptive voltage threshold. The constants $-k_1$ and $-k_2$ identify the values of the ROCOV at which V_{th} reaches the

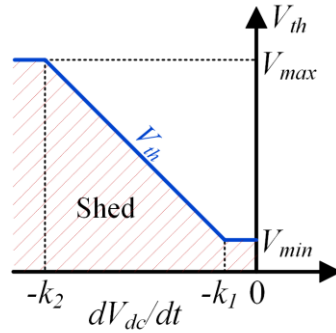


Figure 4.1: Adaptive voltage threshold that depends on the ROCOV.

aforementioned minimum and maximum values, respectively. Figure 4.1 shows the variations of the adaptive voltage threshold with respect to the ROCOV. A non-critical load is instantaneously shed whenever the following two conditions are met:

- the corresponding, i.e., locally measured, bus voltage falls below the adaptive voltage threshold V_{th} ;
- the corresponding ROCOV is negative.

The first condition enables the load shedding scheme to adapt to the prevailing system conditions. Under large disturbances, where the ROCOV is significant, the adaptive voltage threshold V_{th} becomes large and causes faster load shedding in order to limit the voltage drop. When the ROCOV is insignificant, there is no need for fast load shedding, and thus V_{th} is automatically set at a lower value in order to prevent over-shedding. The second condition prevents load shedding when the voltage is rising.

The load shedding steps must be coordinated with each other. The operating characteristics of different non-critical loads are defined such that the adaptive voltage threshold values corresponding to lower priority loads are always higher than those of higher-priority loads. This is achieved by appropriately setting the parameters of the operating characteristics, i.e., k_1 , k_2 , V_{min} , and V_{max} , as described in the next section. The flowchart and block diagram of the proposed adaptive voltage-based load shedding scheme are shown in Figures 4.2 and 4.3. As shown in Figure 4.3, a fourth-order Butterworth low-

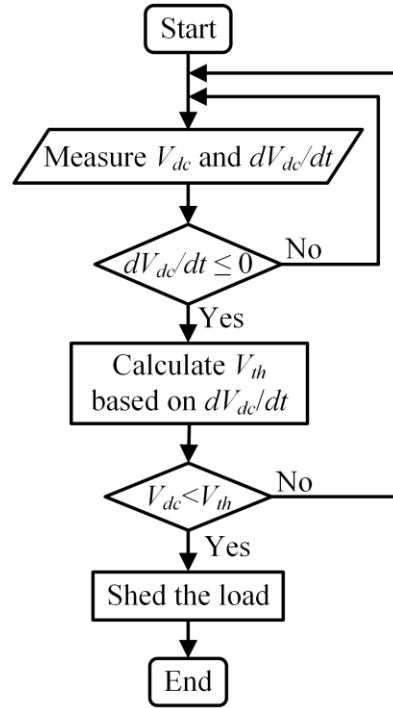


Figure 4.2: Flowchart of the adaptive voltage-based load shedding scheme.

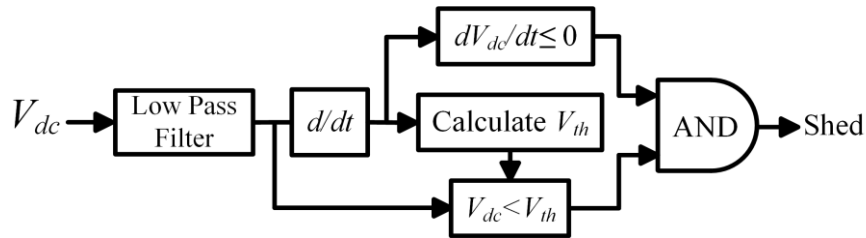


Figure 4.3: Block diagram of the adaptive voltage-based load shedding scheme.

pass filter with the cut-off frequency of 500 Hz is applied to the voltage signal to reduce the adverse effects of noise and switching ripples. The sampling time of the voltage signal is 1 ms. The first backward difference is used to compute the ROCOV as follows:

$$\text{ROCOV} = \frac{V_f(t) - V_f(t - \Delta t)}{\Delta t} \quad (4.3)$$

where V_f is the filtered voltage signal and Δt is the difference step (sampling time).

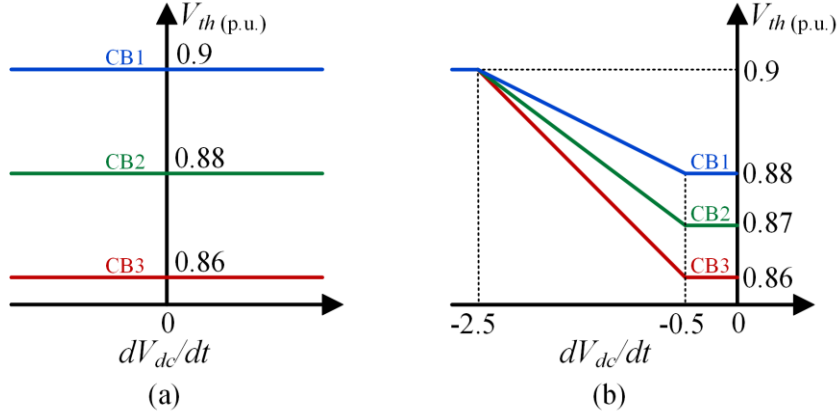


Figure 4.4: Operating characteristics of (a) the conventional load shedding scheme, (b) proposed adaptive load shedding scheme.

4.2.2 Performance Evaluation

This section investigates and compares the performances of the conventional and adaptive voltage-based load shedding schemes in the DC microgrid. Comprehensive time-domain simulation studies are conducted in the PSCAD software environment using the DC microgrid study system of Figure 3.4. In this study, the microgrid is considered to be in normal operating conditions when the bus voltages are above 0.92 p.u. Thus, the highest load shedding voltage threshold for all non-critical loads is set at 0.9 p.u., to prevent load shedding under normal operating conditions. To limit the magnitudes of the voltage sags caused by power imbalance, the lowest voltage threshold, which is used for the last shedding step in both schemes, is set at 0.86 p.u.

Figure 4.4(a) illustrates the operating characteristics of the conventional voltage-based load shedding scheme. This characteristic utilizes voltage thresholds that are uniformly distributed between the aforementioned highest and lowest values. Thus, the conventional voltage-based scheme respectively trips the CBs 1-3 whenever the corresponding bus voltages fall below the thresholds $V_{th1} = 0.9$ p.u., $V_{th2} = 0.88$ p.u. and $V_{th3} = 0.86$ p.u. The operating characteristics of the conventional voltage-based load shedding scheme does not depend on, i.e., is not sensitive to, the magnitude and polarity of the ROCOV.

The proposed adaptive voltage-based load shedding scheme utilizes the voltage threshold defined by (4.1) and shown in Figure 4.4(b), to trip the CBs 1-3. It is assumed that a power

imbalance causing $\text{ROCOV} < -2.5$ p.u./s is extreme and necessitates simultaneous shedding of all non-critical loads as soon as the corresponding bus voltages fall below the abnormal voltage of 0.9 p.u. The reason is that such a disturbance would cause the bus voltages to drop from 0.9 p.u. to 0.8 p.u. within a relatively short time (shorter than 40 ms). On the other hand, a power imbalance causing -0.5 p.u./s $< \text{ROCOV} < 0$ p.u./s can be mitigated by shedding the non-critical loads using lower and selective voltage thresholds, because such a disturbance would take a relatively long time (longer than 200 ms) to decrease the bus voltages by 0.1 p.u. Therefore, the ROCOV thresholds are set at $k_1 = 0.5$ and $k_2 = 2.5$ p.u./s.

Figure 4.4(b) shows that the proposed scheme utilizes an equal maximum load shedding threshold for shedding all three non-critical loads when the voltage drops at a significant rate, i.e., $V_{max1} = V_{max2} = V_{max3} = 0.9$ p.u. To achieve selective load shedding under less severe power imbalance conditions, the non-critical loads are prioritized by utilizing different load shedding voltage thresholds. This is accomplished by utilizing different minimum voltage thresholds, that is, $V_{min1} = 0.88$ p.u., $V_{min2} = 0.87$ p.u., and $V_{min3} = 0.86$ p.u. These values are determined based on the results of comprehensive simulation studies.

4.2.2.1 Case Study 1: Large Disturbance

The first case study investigates the DC microgrid behavior under a large generation disturbance. Before the disturbance ($t < 0.5$ s), the microgrid is islanded. The WT operates in the MPPT mode and generates 1 MW power, the PV units do not generate power (at night), and the total power demand of the loads is 1.25 MW. Thus, the BESSs inject 0.3 MW into the microgrid to maintain the power balance and regulate the bus voltages. The voltages at the node 702 and at the terminals of CBs 1-3 are between 0.96 and 0.99 p.u. At $t = 0.5$ s, the power generation of the WT becomes zero due to an unscheduled shut down. Thus, the BESSs inject their maximum power of 0.8 MW into the microgrid to maintain the power balance. As the total power capacity of the BESSs is smaller than the power demand of the loads, the bus voltages start to fall at a significant rate. The performances of the conventional and adaptive voltage-based load shedding schemes under this large disturbance are investigated and compared in this sub-section.

4.2.2.1.1 Conventional Voltage-based Load Shedding Scheme

Figure 4.5 illustrates the performance of the conventional voltage-based load shedding scheme under the aforementioned large disturbance. Figure 4.5(a) shows the voltage of the node 702, that is at the center of the critical load area, and the voltages at the load-side terminals of the CBs 1-3 (seen by the non-critical loads). Figure 4.5(b) shows the ROCOV seen by the non-critical loads, which is not used by the conventional load shedding scheme. Figure 4.5(c) shows the total power demand of the loads in the microgrid. As shown in Figure 4.5(c), the conventional scheme is able to maintain the power balance after the disturbance by shedding all three groups of the non-critical loads at $t = 0.515$ s, 0.541 s, and 0.564 s, respectively. However, this scheme is not sufficiently fast. The voltage seen by the critical loads remains below 0.9 p.u for more than 0.1 s and is eventually regulated at an acceptable level (0.92 p.u.) within about 0.25 s after the disturbance.

The performance of the conventional voltage-based load shedding scheme depends on its predetermined fixed voltage thresholds. The thresholds are determined such that acceptable performance is achieved under specific operating conditions. The performance is degraded as the operating conditions change. In addition, using voltage thresholds that are closer to 1 p.u. leads to more desirable steady-state voltage regulation and smaller voltage sags, but may result in shedding an unnecessarily large amount of loads, and vice versa. Hence, utilizing the conventional load shedding scheme necessitates a compromise between the voltage regulation performance and the power supply reliability.

4.2.2.1.2 Adaptive Voltage-based Load Shedding Scheme

Figure 4.6 illustrates the performance of the adaptive voltage-based load shedding scheme under the disturbance of Figure 4.5. Figure 4.6(b) shows that the magnitude of the ROCOV caused by the large power deficit is considerably large. Consequently, the adaptive voltage thresholds used for all three steps of load shedding are automatically set at or slightly below 0.9 p.u., based on the characteristics of Figure 4.4(b). This results in shedding all three groups of the non-critical loads as soon as the corresponding bus voltages fall below 0.9 p.u., as illustrated in Figure 4.6(c). Hence, the adaptive load shedding scheme trips the CBs 1-3 at $t = 0.515$ s, 0.533 s, and 0.533 s, respectively. Due to the faster reaction of the proposed

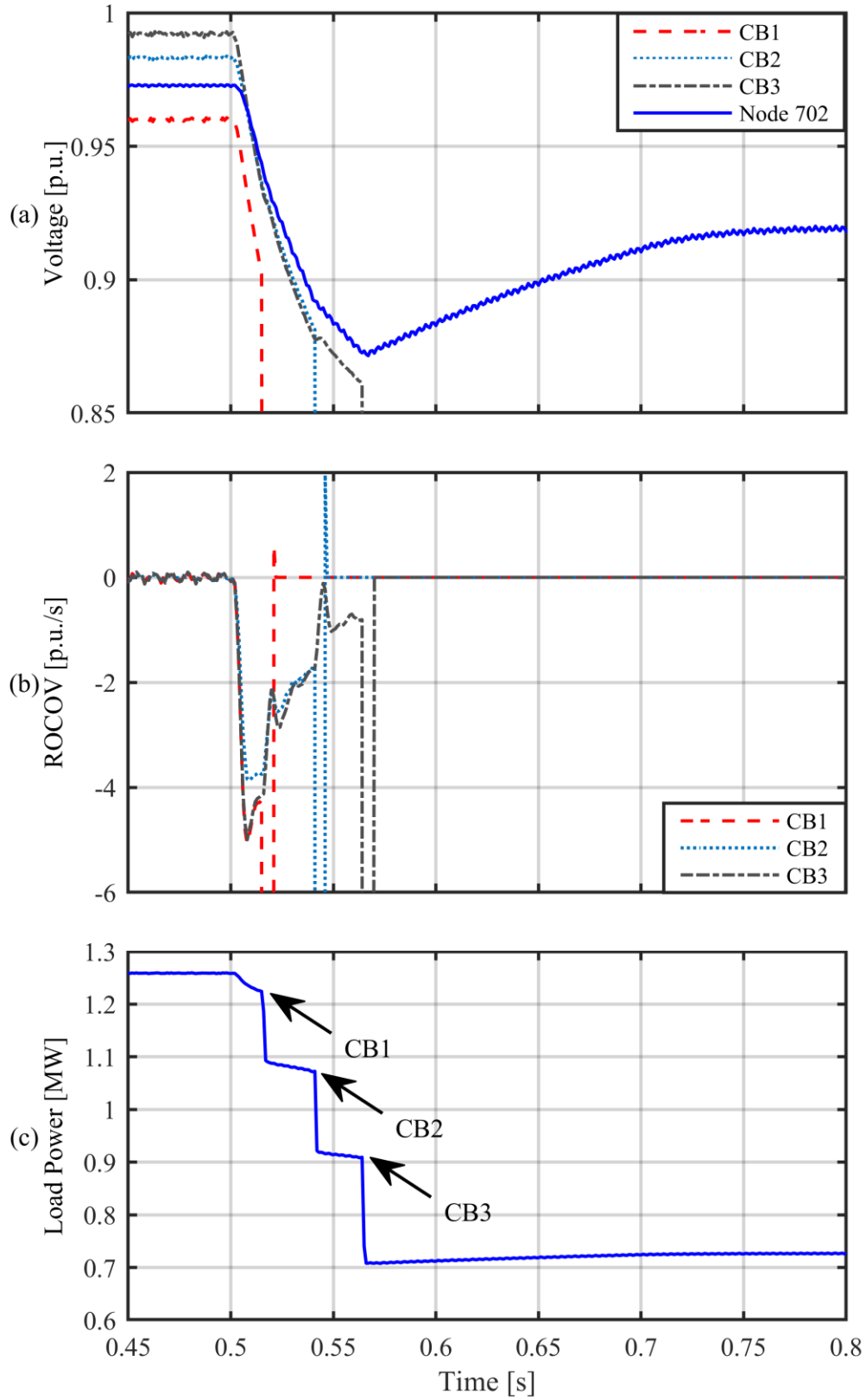


Figure 4.5: Performance of the conventional voltage-based load shedding scheme in the *Case Study 1*: (a) DC voltages, (b) ROCOV, (c) total load power.

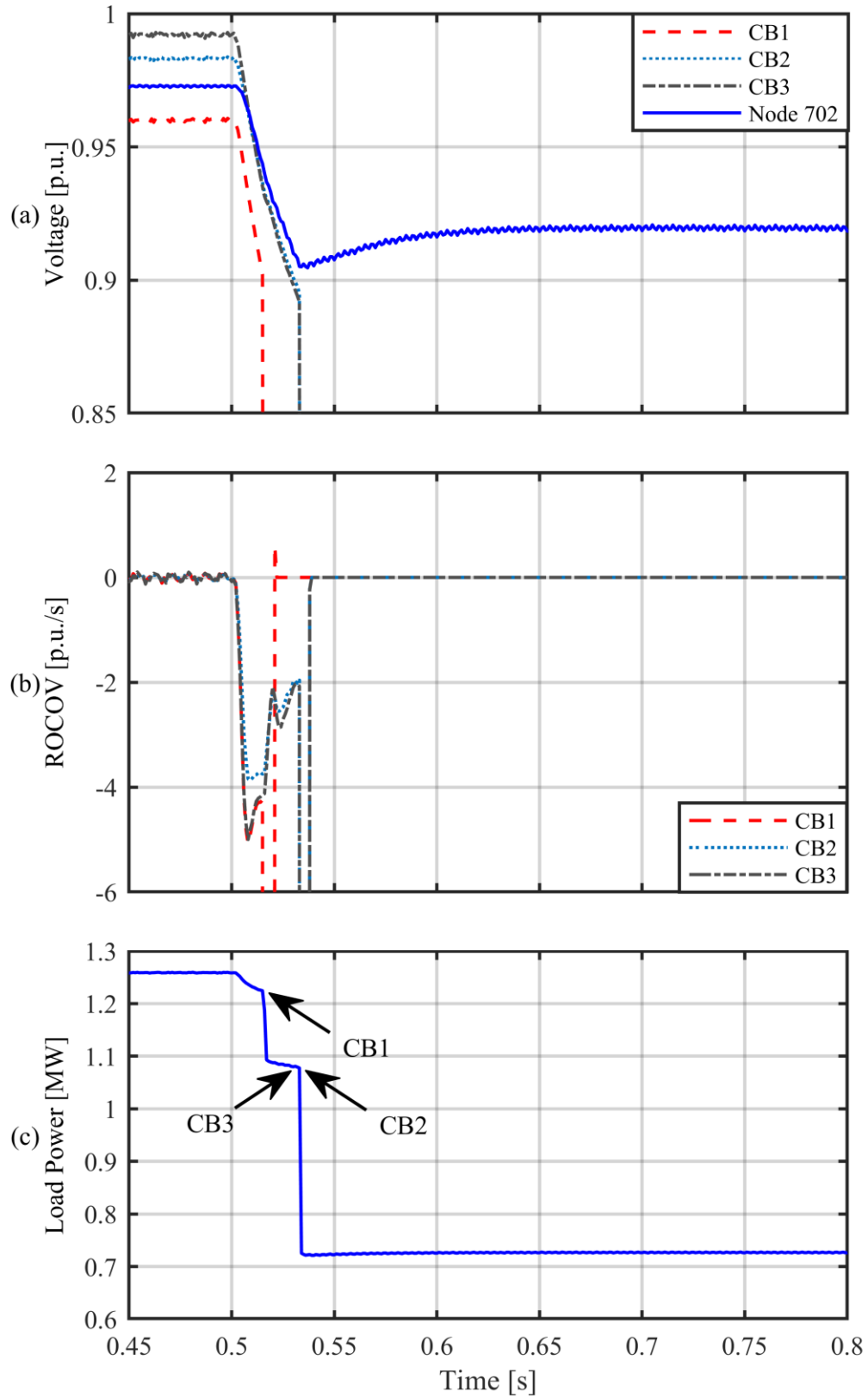


Figure 4.6: Performance of the adaptive voltage-based load shedding scheme in the *Case Study 1*: (a) DC voltages, (b) ROCOV, (c) total load power.

adaptive scheme, the voltage seen by the critical loads (voltage of the node 702) does not fall below 0.9 p.u., and is regulated at the acceptable level of 0.92 p.u., within a relatively short time (less than 0.1 s) after the disturbance, as shown in Figure 4.6(a). The results of Figure 4.6 indicate that the proposed scheme reduces the load shedding delay when a large disturbance causes the bus voltages to fall at a significant rate.

4.2.2.2 Case Study 2: Small Disturbance

The second case study investigates the performances of the conventional and adaptive voltage-based load shedding schemes under a less severe disturbance. Before the disturbance is applied ($t < 0.5$ s), the microgrid is islanded. The WT operates in the MPPT mode and generates 0.7 MW power, the PV units are out of service, and the total power demand of the loads is 1.21 MW. Thus, the BESSs inject 0.55 MW into the microgrid to maintain the power balance and regulate the DC bus voltages. The voltages at the node 702 and at the terminals of the CBs 1-3 are between 0.92 and 0.96 p.u. The disturbance in this case study is a slower change of the WT power output caused by the variations of wind speed. The power generation of the WT gradually changes from 0.7 MW to 0.5 MW during the time period of $0.5 \text{ s} < t < 0.8 \text{ s}$, and from 0.5 MW to 0.8 MW during the time period of $0.8 \text{ s} < t < 1.1 \text{ s}$. This power disturbance causes relatively slow variations of the bus voltages within the microgrid. The performances of the conventional and adaptive load shedding schemes under this disturbance are investigated and the results are shown in Figures 4.7 and 4.8.

4.2.2.2.1 Conventional Voltage-based Load Shedding Scheme

Figure 4.7 illustrates the performance of the conventional voltage-based load shedding scheme under the aforementioned wind speed disturbance. Figure 4.7(a) shows that the wind speed drop causes the voltage at the terminal of CB1, i.e., seen by the first group of non-critical loads, to fall below 0.9 p.u., i.e., the highest voltage threshold in Figure 4.5(a). Hence, the conventional load shedding scheme sheds the first group of non-critical loads by tripping the CB1 at $t = 0.725$ s, as shown in Figure 4.7(c). Consequently, the voltages seen by the rest of the loads are increased, as illustrated in Figure 4.7(a). It should be noted that the ROCOV shown in Figure 4.7(b) is not used by the conventional load shedding scheme.

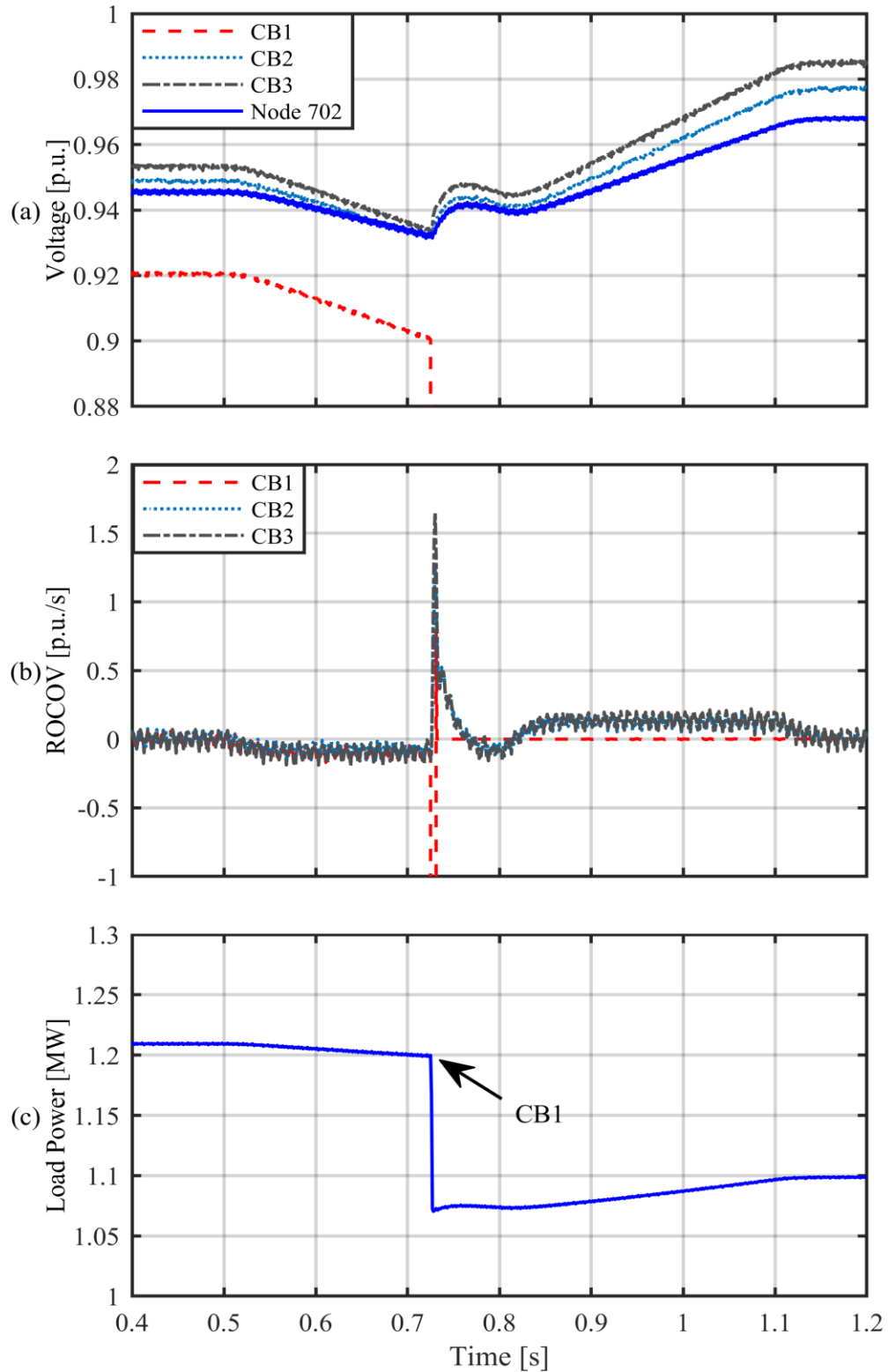


Figure 4.7: Performance of the conventional voltage-based load shedding scheme in the *Case Study 2*: (a) DC voltages, (b) ROCOV, (c) total load power.

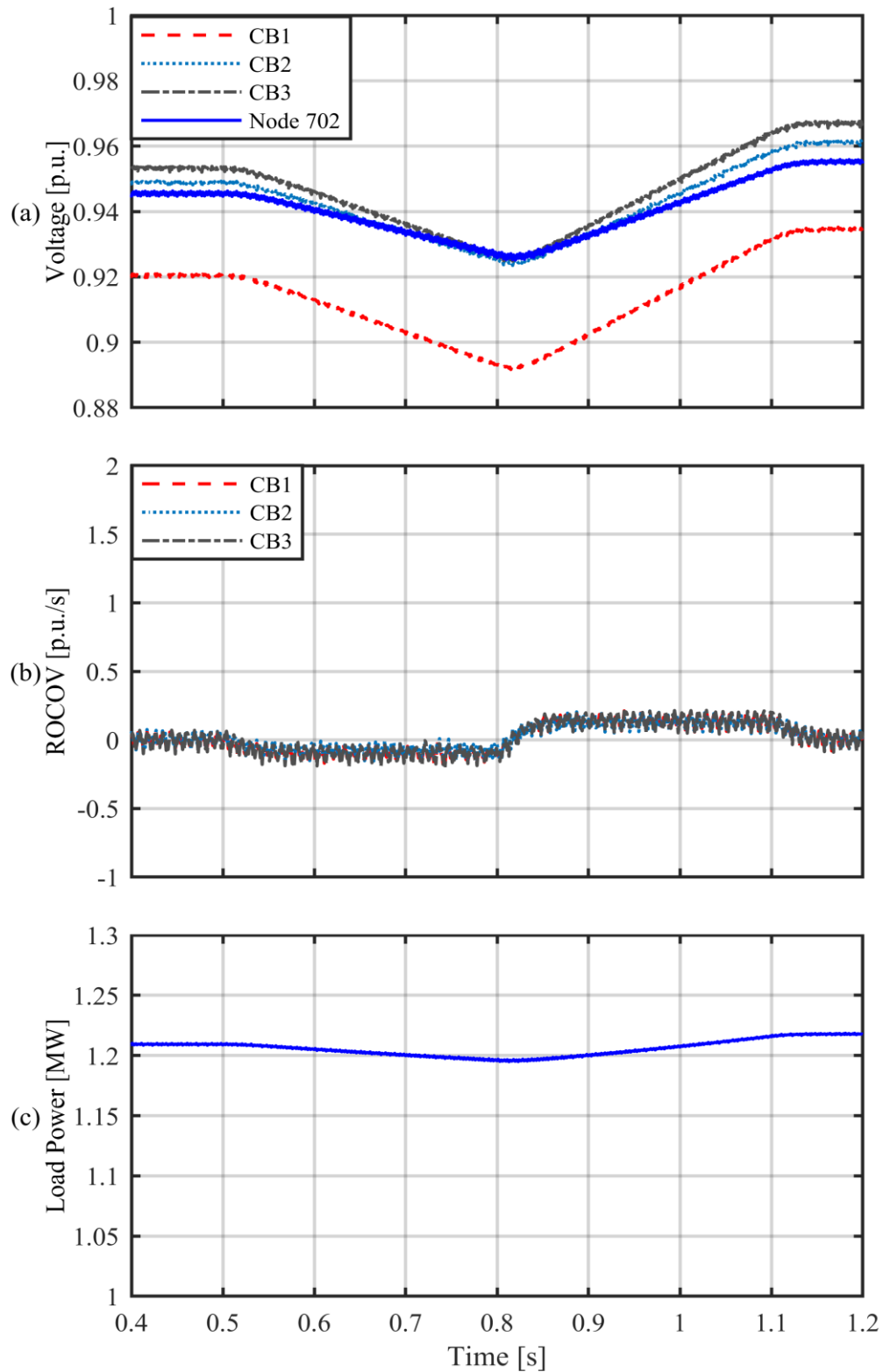


Figure 4.8: Performance of the adaptive voltage-based load shedding scheme in the *Case Study 2*: (a) DC voltages, (b) ROCOV, (c) total load power.

4.2.2.2.2 Adaptive Voltage-based Load Shedding Scheme

Figure 4.8 illustrates the performance of the adaptive voltage-based load shedding scheme under the wind speed disturbance of Figure 4.7. As shown in Figure 4.8(c), the proposed adaptive scheme does not shed any loads. The reason is that the magnitude of the ROCOV caused by the slow wind speed variations is less than 0.5 p.u./s, Figure 4.8(b). Hence, the adaptive voltage thresholds used for load shedding by CBs 1-3 become 0.88 p.u., 0.87 p.u., and 0.86 p.u., respectively, based on the characteristics of Figure 4.4(b). The load voltages of Figure 4.8(a) do not fall below any of the aforementioned adaptive thresholds. Comparing the results of Figures 4.7 and 4.8 indicates that the load shedding performed by the conventional scheme was not necessary. In other words, the conventional scheme unnecessarily degraded the power supply reliability. The proposed adaptive load shedding scheme becomes more secure, i.e., utilizes lower voltage thresholds, whenever the load voltages do not fall at a high rate. This prevents unnecessary shedding of non-critical loads.

4.2.2.3 Case Study 3: Islanding

The third case study represents an unscheduled islanding scenario. Before $t = 0.5$ s, the DC microgrid is grid-connected, but the generation levels are low. The WT generates 0.2 MW in the MPPT mode, the PV systems are out of service (at night). The BESSs inject 0.17 MW power, and the total power demand of the loads is 1.22 MW. The GTC imports 0.91 MW from the AC grid to maintain the power balance and regulate the DC bus voltages. The voltages at the node 702 and at the terminals of CBs 1-3 are between 0.92 and 0.97 p.u. At $t = 0.5$ s, the DC microgrid is islanded and the GTC becomes unable to exchange power with the AC grid. The BESSs inject their maximum power of 0.8 MW into the microgrid, which is not sufficient to fully mitigate the power imbalance. As a result, the bus voltages start to fall at a moderate rate. The performances of the conventional and adaptive voltage-based load shedding schemes under the aforementioned disturbance are investigated and the results are shown in Figures 4.9 and 4.10.

4.2.2.3.1 Conventional Voltage-based Load Shedding Scheme

Figure 4.9 illustrates the performance of the conventional load shedding scheme under the aforementioned islanding disturbance. Figure 4.9(a) shows that the unscheduled islanding

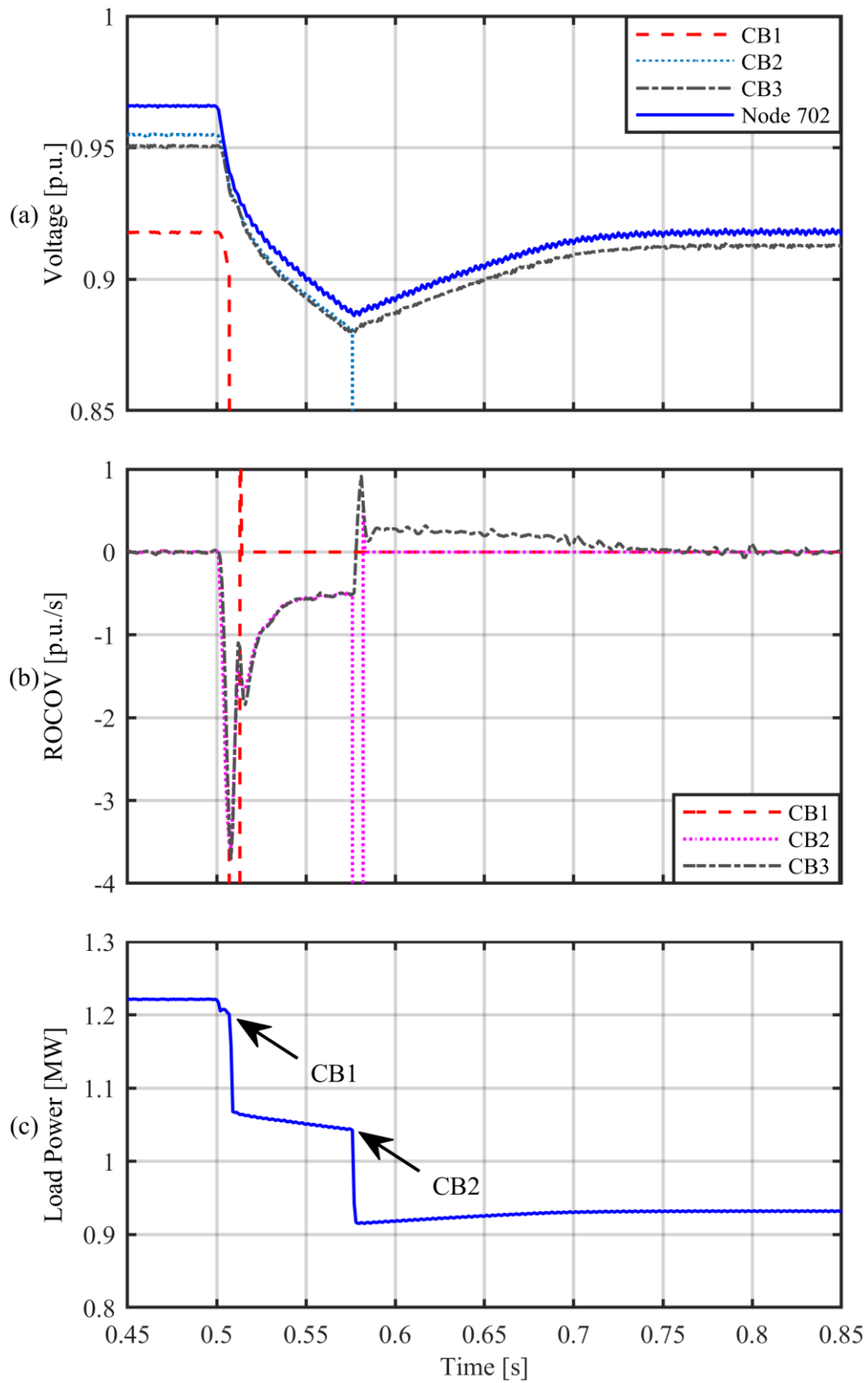


Figure 4.9: Performance of the conventional voltage-based load shedding scheme in the *Case Study 3*: (a) DC voltages, (b) ROCOV, (c) total load power.

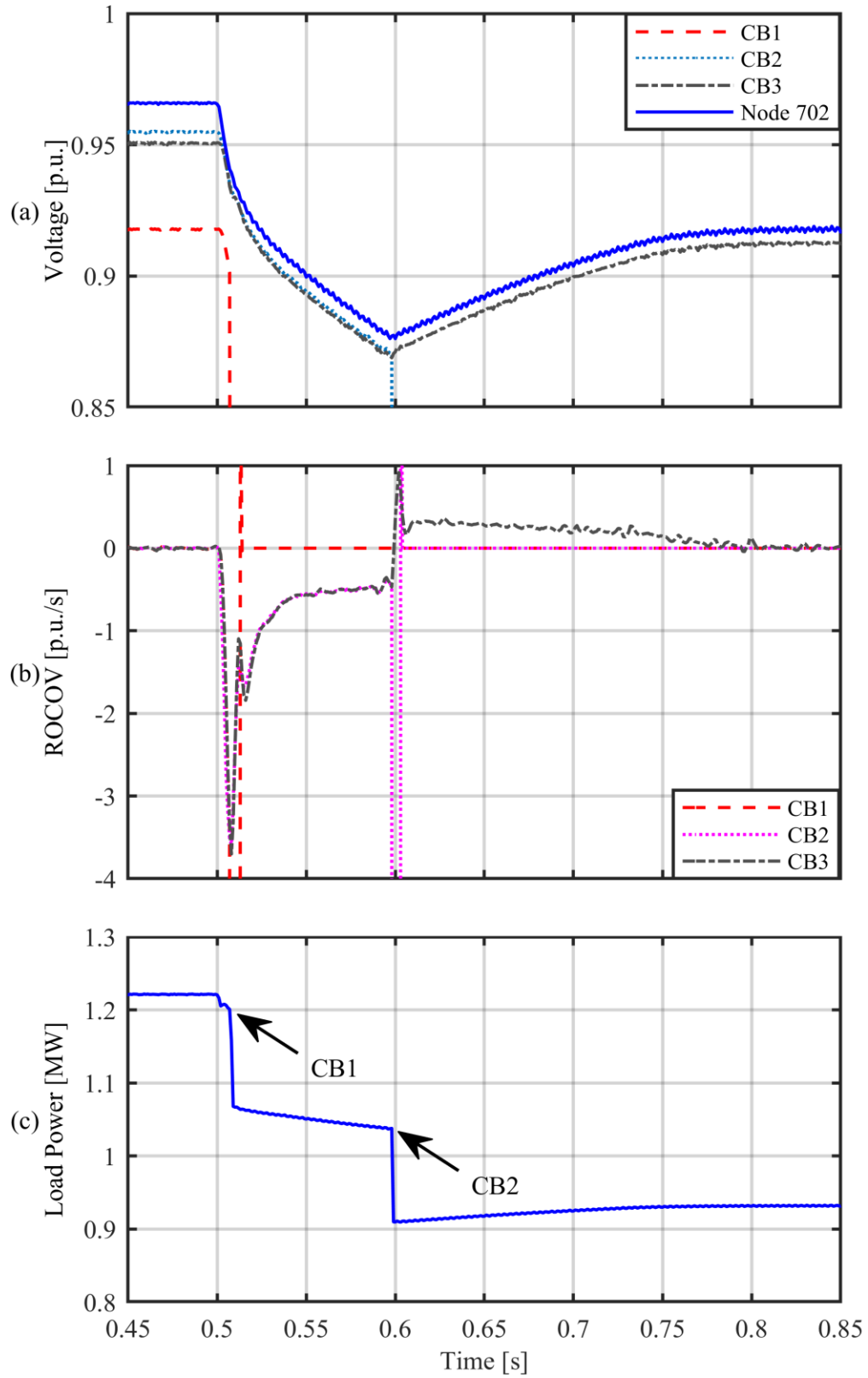


Figure 4.10: Performance of the adaptive voltage-based load shedding scheme in the *Case Study 3*: (a) DC voltages, (b) ROCOV, (c) total load power.

causes the bus voltages in the microgrid to fall below 0.88 p.u. Thus, the conventional scheme sheds two groups of non-critical loads by tripping the CBs 1 and 2 at $t = 0.507$ s, and 0.576 s, respectively. Hence, the total power demand is decreased to 0.93 MW, Figure 4.9(c). The voltage seen by the critical loads (voltage of the node 702) is regulated at an acceptable level (0.92 p.u.) within about 0.2 s after the disturbance.

4.2.2.3.2 Adaptive Voltage-based Load Shedding Scheme

Figure 4.10 illustrates the performance of the proposed adaptive load shedding scheme under the disturbance of Figure 4.9. Figure 4.10(b) shows that the magnitude of the ROCOV caused by the unscheduled islanding is not too large, especially after the first load shedding step. Hence, the adaptive voltage thresholds are set at values slightly lower than those of the conventional scheme, based on the characteristics of Figure 4.4(b). The adaptive load shedding scheme trips the CBs 1 and 2 at $t = 0.507$ s, and 0.598 s, respectively. As a result, the total power demand of loads reduces to 0.93 MW, and the voltage seen by the critical loads is regulated at an acceptable level (0.92 p.u.) within about 0.25 s after the disturbance.

The results of Figures 4.9 and 4.10 indicate that the adaptive and conventional voltage-based load shedding schemes have similar performances when a disturbance causes the bus voltages to fall at a moderate rate. Although the proposed scheme slightly increases the load shedding delay in this case study (50 ms), this does not considerably increase the voltage drop, as illustrated in Figures 4.9(a) and 4.10(a). The significant benefits of the proposed scheme, which are highlighted by the *Case Studies 1* and 2, justify the aforementioned short delay under moderate disturbances.

4.3 Adaptive Timer-based Load Shedding Scheme

4.3.1 Introduction

In this section, an adaptive timer-based load shedding scheme is proposed for the DC microgrid. The proposed load shedding scheme utilizes an adaptive time delay T that depends on the ROCOV, as determined by:

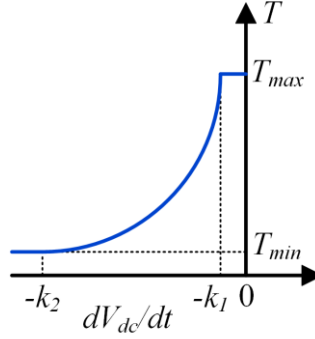


Figure 4.11: Adaptive time delay that depends on the ROCOV.

$$T = \begin{cases} T_{max} & , \quad -k_1 < \frac{dV_{dc}}{dt} \leq 0 \\ \frac{T_{max}k_1}{|dV/dt|} & , \quad -k_2 \leq \frac{dV_{dc}}{dt} \leq -k_1 \\ T_{min} & , \quad -\infty < \frac{dV_{dc}}{dt} < -k_2 \end{cases} \quad (4.4)$$

$$\frac{T_{min}}{T_{max}} = \frac{k_1}{k_2} \quad (4.5)$$

where T_{min} and T_{max} are the minimum and maximum values of the adaptive time delay. The constants $-k_1$ and $-k_2$ identify the values of the ROCOV at which the adaptive time delay reaches the aforementioned minimum and maximum values, respectively. Figure 4.11 shows the variations of the adaptive time delay with respect to the ROCOV. A non-critical load is instantaneously shed whenever the following two conditions are met.

- The corresponding bus voltage remains below a common voltage threshold V_{th} (shared by all non-critical loads) for a time period longer than the corresponding adaptive delay;
- The under-voltage condition is not improving, i.e., the corresponding ROCOV is not positive.

The first condition enables the load shedding scheme to adapt to the prevailing system conditions by using a time delay that depends on the ROCOV. Under large disturbances, where the magnitude of the ROCOV is significant, the adaptive time delay T becomes shorter and causes faster load shedding in order to limit the voltage drop. When the ROCOV is insignificant, there is no need for fast load shedding, and thus the delay becomes

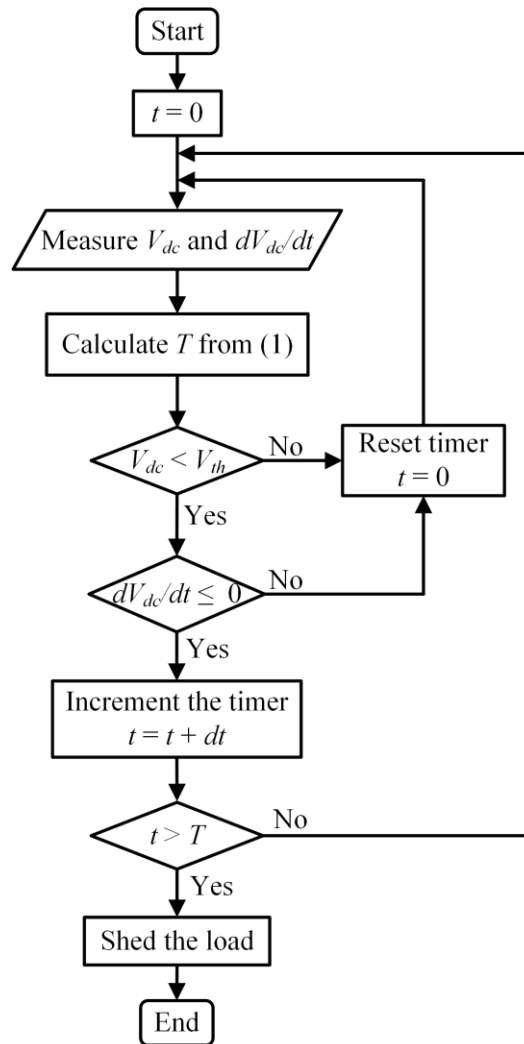


Figure 4.12: Flowchart of the adaptive timer-based load shedding scheme.

longer in order to prevent over-shedding. The second condition prevents load shedding when the voltage is rising, even if it is below the threshold V_{th} .

The time delay characteristics of different load shedding steps are defined such that, under any operating conditions, the time delay corresponding to a lower priority load is shorter than that of a higher-priority load. This is achieved by appropriately setting the parameters of (4.4), i.e., k_1 , k_2 , T_{min} , and T_{max} , as described in the next section. The flowchart and block diagram of the proposed load shedding scheme are shown in Figures 4.12 and 4.13.

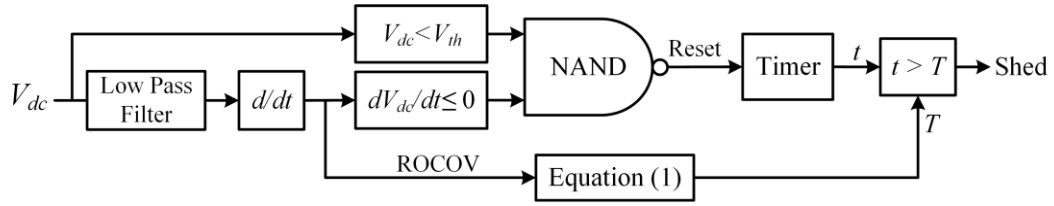


Figure 4.13: Block diagram of the adaptive timer-based load shedding scheme.

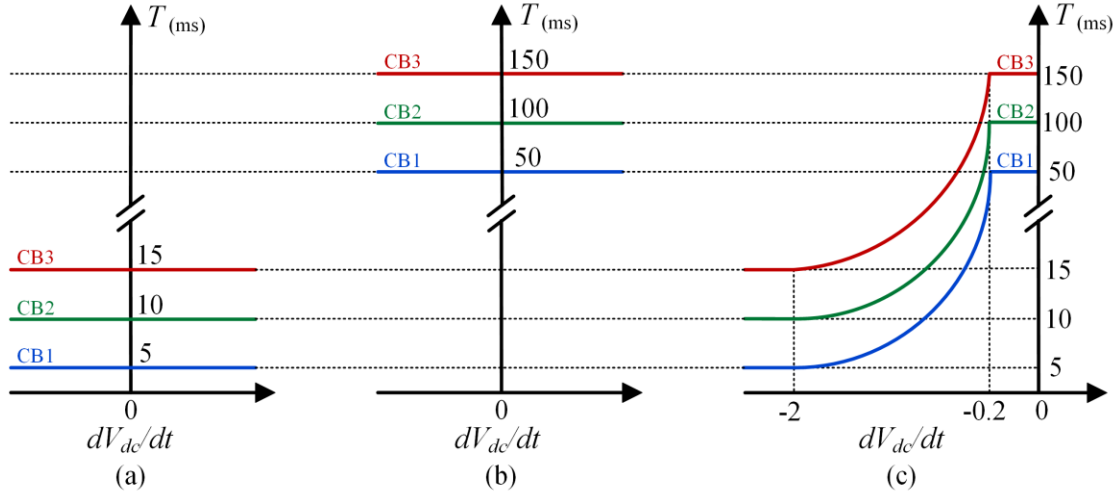


Figure 4.14: Operating characteristics of different load shedding schemes: (a) conventional scheme with short delays, (b) conventional scheme with long delays, (c) adaptive scheme.

4.3.2 Performance Evaluation

This section investigates and compares the performances of the conventional and adaptive timer-based load shedding schemes in the DC microgrid. The conventional scheme trips the CBs 1-3 whenever the corresponding bus voltages remain below the voltage threshold $V_{th} = 0.9$ p.u. for time periods longer than T_1 , T_2 , and T_3 , respectively. Figure 4.14 (a) shows the operating characteristics of the conventional scheme with the short delays of $T_1 = 5$ ms, $T_2 = 10$ ms and $T_3 = 15$ ms. Figure 4.14 (b) shows the operating characteristics of the conventional scheme with the longer delays of $T_1 = 50$ ms, $T_2 = 100$ ms and $T_3 = 150$ ms. As illustrated in Figure 4.14 (a) and (b), the operating characteristics of the conventional load shedding scheme does not depend on, i.e., is not sensitive to, the magnitude and polarity of the ROCOV.

The proposed load shedding scheme utilizes the adaptive time delay defined by (4.4) and shown in Figure 4.14 (c), to trip the CBs 1-3. A power imbalance causing $\text{ROCOV} < -2$ p.u./s is extreme and necessitates fast shedding of all non-critical loads as soon as the bus voltages fall below $V_{th} = 0.9$ p.u. The reason is that such a disturbance would cause the bus voltages to drop from 0.9 p.u. to 0.8 p.u. within a relatively short time (shorter than 40 ms). On the other hand, a power imbalance causing -0.2 p.u./s $< \text{ROCOV} < 0$ p.u./s can be mitigated by further delayed load shedding, because such a disturbance would take a relatively long time (longer than 200 ms) to decrease the bus voltages by 0.1 p.u. Thus, the ROCOV thresholds are set at $k_1 = 0.2$ and $k_2 = 2$ p.u./s for all three CBs. The minimum delays associated with the CBs 1-3 are $T_{min1}=5$ ms, $T_{min2}=10$ ms, and $T_{min3}=15$ ms, respectively. The maximum delays associated with the CBs 1-3 are $T_{max1}=50$ ms, $T_{max2}=100$ ms, and $T_{max3}=150$ ms, respectively. These values are determined based on the results of comprehensive simulation studies.

4.3.2.1 Case Study 1: Large Disturbance

The first case study investigates the DC microgrid response to a large generation disturbance. Initially, i.e., at $t < 0.5$ s, the microgrid is islanded, the WT generates 1 MW power in the MPPT mode, the PV systems do not generate power (at night), and the total power demand of the loads is 1.24 MW. The BESSs regulate the DC bus voltages in the range of 0.96 p.u. to 1.0 p.u., by injecting 0.27 MW into the microgrid. Due to an unscheduled shut down at $t = 0.5$ s, the power generation of the WT becomes zero. Subsequently, each BESS injects its maximum power of 0.4 MW into the microgrid, to maintain the power balance. As the total power rating of the BESSs is smaller than the power demand, the bus voltages start to fall. This sub-section investigates and compares the performances of the conventional timer-based load shedding scheme (with short and long delays) and the proposed adaptive timer-based load shedding scheme, under the aforementioned disturbance.

4.3.2.1.1 Conventional Timer-based Load Shedding Scheme

Figure 4.15 illustrates the performance of the conventional timer-based load shedding scheme with short delays. Figure 4.15(a) shows the critical load voltage (node 702), and the

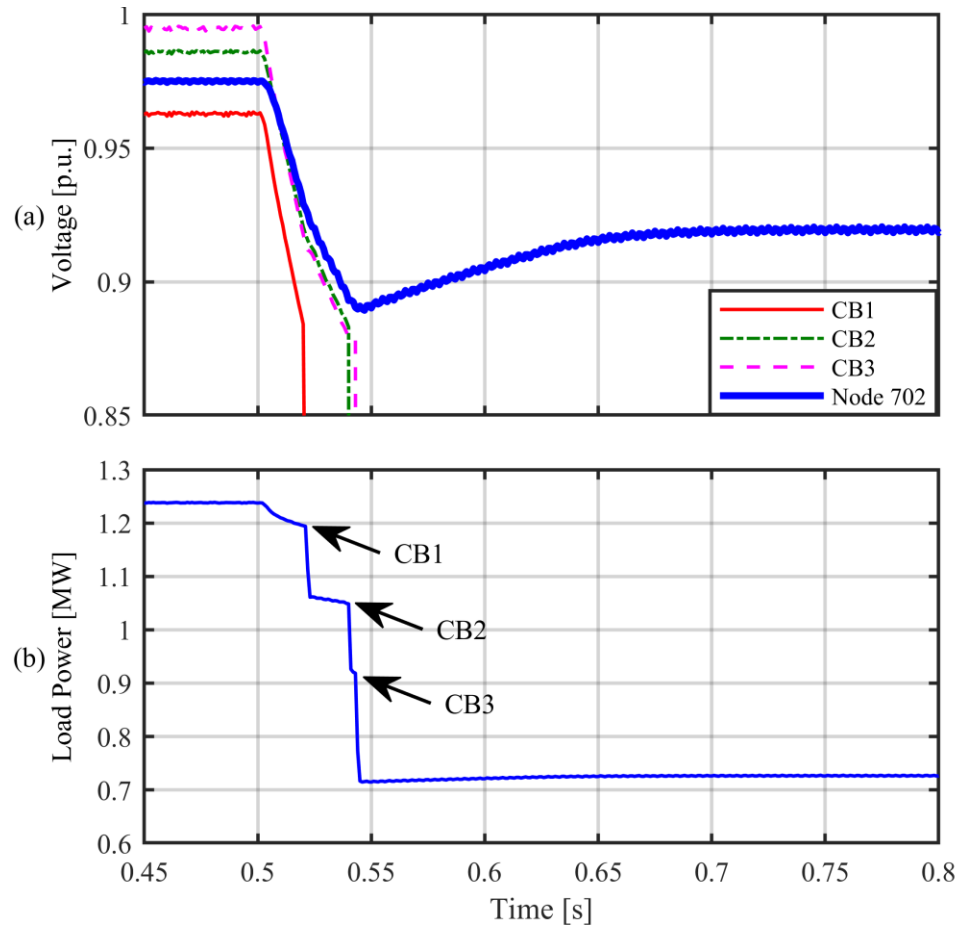


Figure 4.15: Performance of the conventional timer-based load shedding scheme with short delays, in the *Case Study I*: (a) bus voltages, (b) total power demand of the loads.

non-critical load voltages (voltages at the load-side terminals of the CBs 1-3). Figure 4.15(b) shows the total power demand of the loads in the microgrid. The conventional load shedding scheme with short delays quickly sheds all three groups of the non-critical loads by tripping the CBs 1-3 at $t = 0.52$ s, 0.54 s, and 0.543 s, respectively. Consequently, the voltage seen by the critical loads does not fall below 0.89 p.u., and is regulated at 0.92 p.u. within about 0.15 s after the disturbance.

Figure 4.16 shows the performance of the conventional timer-based load shedding scheme with long delays, under the same disturbance scenario as that of Figure 4.15. As shown in Figure 4.16(b), the non-critical loads are shed by tripping the CBs 1-3 at $t = 0.565$ s, 0.626 s, and 0.675 s, respectively. Due to the increased load shedding delay, the voltage seen by the critical loads drops to 0.72 p.u. and remains below 0.9 p.u. for more than 0.5 s.

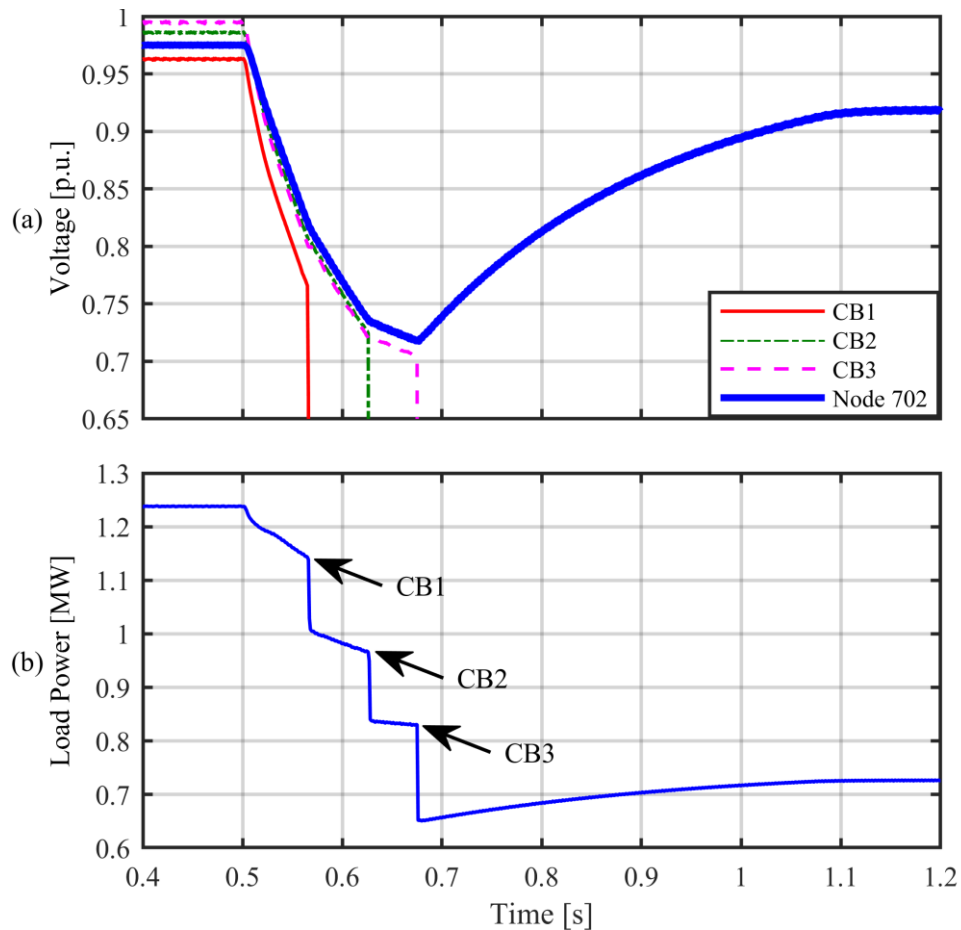


Figure 4.16: Performance of the conventional timer-based load shedding scheme with long delays, in the *Case Study I*: (a) bus voltages, (b) total power demand of the loads.

The critical load voltage is eventually regulated at 0.92 p.u. within about 0.6 s after the disturbance. The performance of the conventional timer-based load shedding scheme depends on the predetermined fixed time delays. The results of Figures 4.15 and 4.16 indicate that more desirable voltage regulation can be achieved by using shorter delays. However, it is shown in section 4.3.1.2.1 that short delays may cause unnecessary load shedding by the conventional timer-based scheme.

4.3.2.1.2 Adaptive Timer-based Load Shedding Scheme

Figure 4.17 illustrates the performance of the proposed adaptive timer-based load shedding scheme under the disturbance of Figure 4.15. The proposed scheme quickly sheds the non-critical loads by tripping the CBs 1-3 at $t = 0.521$ s, 0.542 s, and 0.568 s, respectively. These results are close to the performance of the conventional timer-based load shedding

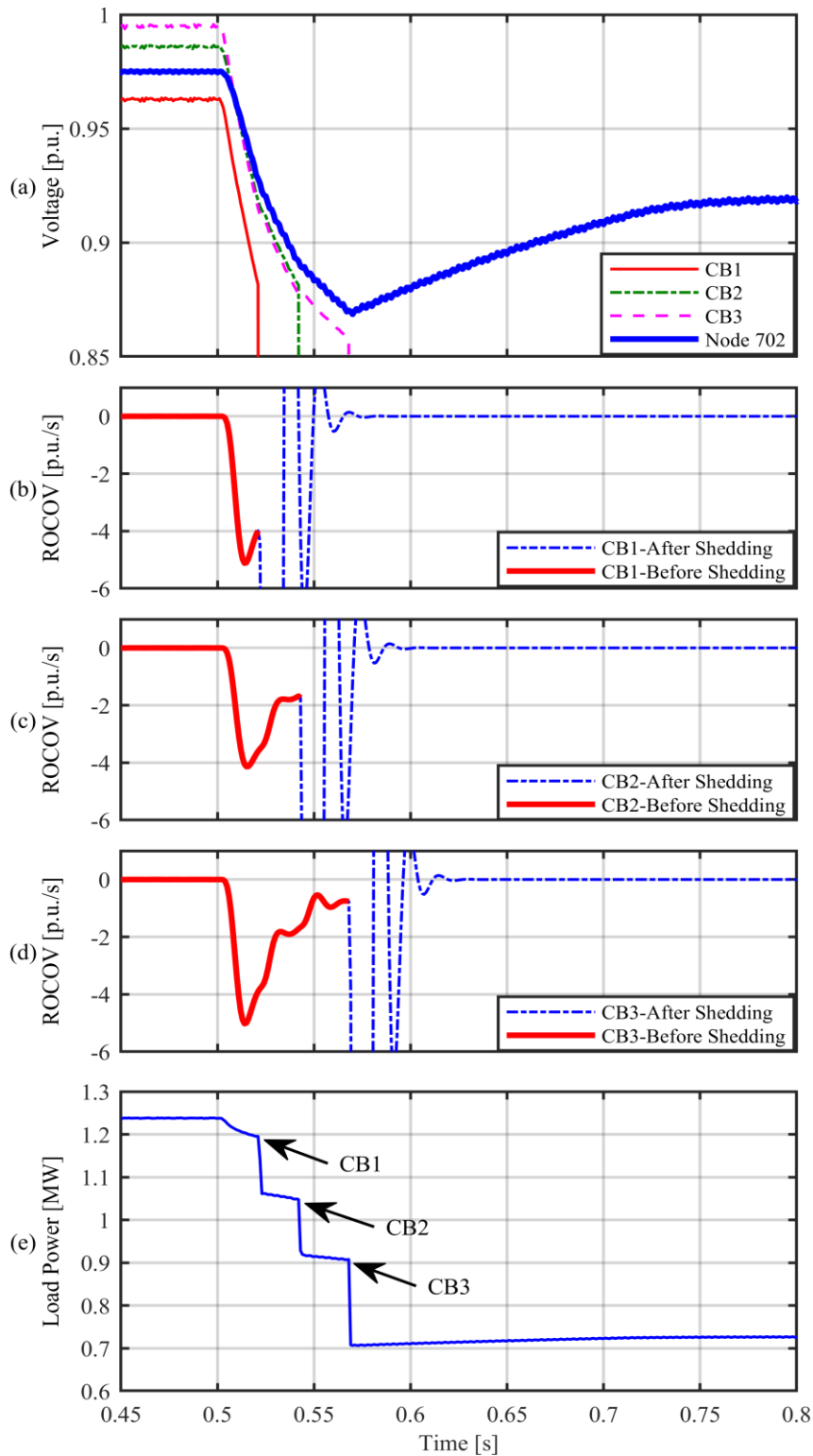


Figure 4.17: Performance of the adaptive timer-based load shedding scheme in the *Case Study 1*: (a) bus voltages, (b) ROCOV at the load-side terminal of CB1, (c) ROCOV at the load-side terminal of CB2, (d) ROCOV at the load-side terminal of CB3 (e) total power demand of the loads.

scheme with short delays. The reason is that the magnitude of the ROCOV caused by the disturbance in the *Case Study 1* is considerably large, as shown in Figures 4.17(b)-(d). Hence, based on the characteristics of Figure 4.14(c), the adaptive load shedding time delay of each CB is automatically set at or slightly above the corresponding minimum delay T_{min} .

Due to the fast reaction of the proposed load shedding scheme, the critical load voltage (node 702) does not fall below 0.875 p.u., and is regulated at 0.92 p.u. within a relatively short time (about 0.2 s) after the disturbance. Figure 4.18 illustrates how the adaptive delay T is compared with the time duration of the under-voltage condition ($V_{dc} < 0.9$ p.u.), i.e., the output of the timer in Figure 4.13, to determine whether the loads downstream of the CBs 1-3 must be shed. Figures 4.18 (a)-(c) show the adaptive time-delay characteristics (solid red line) and the operating point trajectory (dotted blue line) of the load shedding algorithms utilized to trip the CBs 1-3, respectively. The vertical axis in each of the Figures 4.18 (a)-(c) represents the time duration of the under-voltage condition. The horizontal axis represents the instantaneous value of the ROCOV.

The results of Figures 4.17 and 4.18 indicate that the proposed adaptive load shedding scheme effectively limits the magnitude and duration of the voltage sag by taking fast action when the magnitude of the ROCOV is large. In other words, Figure 4.17 shows that the performance of the proposed adaptive load shedding scheme is almost equivalent to that of the conventional timer-based scheme with short delays, when the power deficit is significant.

4.3.2.2 Case Study 2: Islanding

The second case study investigates the performances of the conventional and adaptive timer-based load shedding schemes in an unscheduled islanding scenario. Before $t = 0.5$ s, the DC microgrid is connected to the AC grid, but the generation levels are low. The WT generates 0.25 MW in the MPPT mode, the PV systems are out of service (at night), the BESSs inject 0.16 MW power, and the total power demand of the loads is 1.22 MW. The GTC imports 0.88 MW from the AC grid to maintain the power balance and regulate the DC bus voltages.

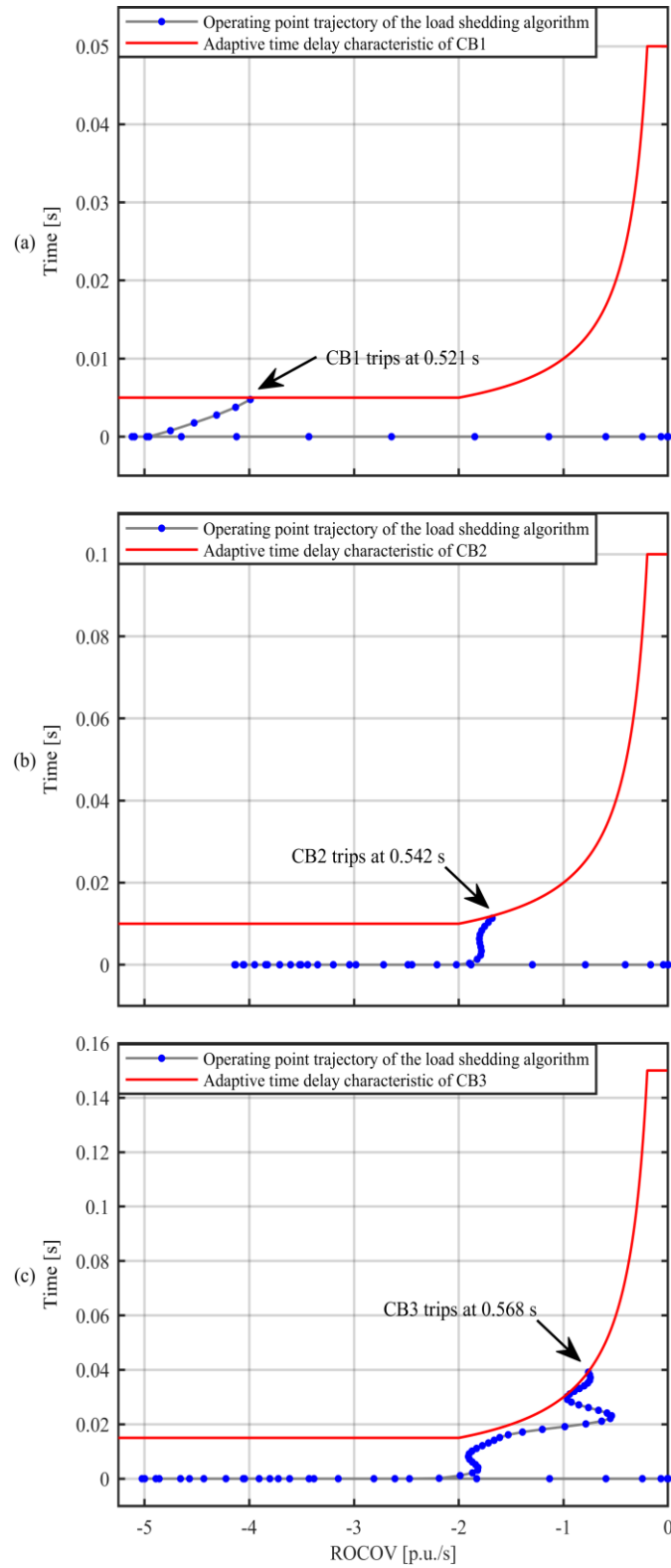


Figure 4.18: Adaptive time-delay characteristics (solid red line) and the operating point trajectory (dotted blue line) of the load shedding algorithms utilized to trip (a) CB1, (b) CB2, and (c) CB3, in the *Case Study 1*.

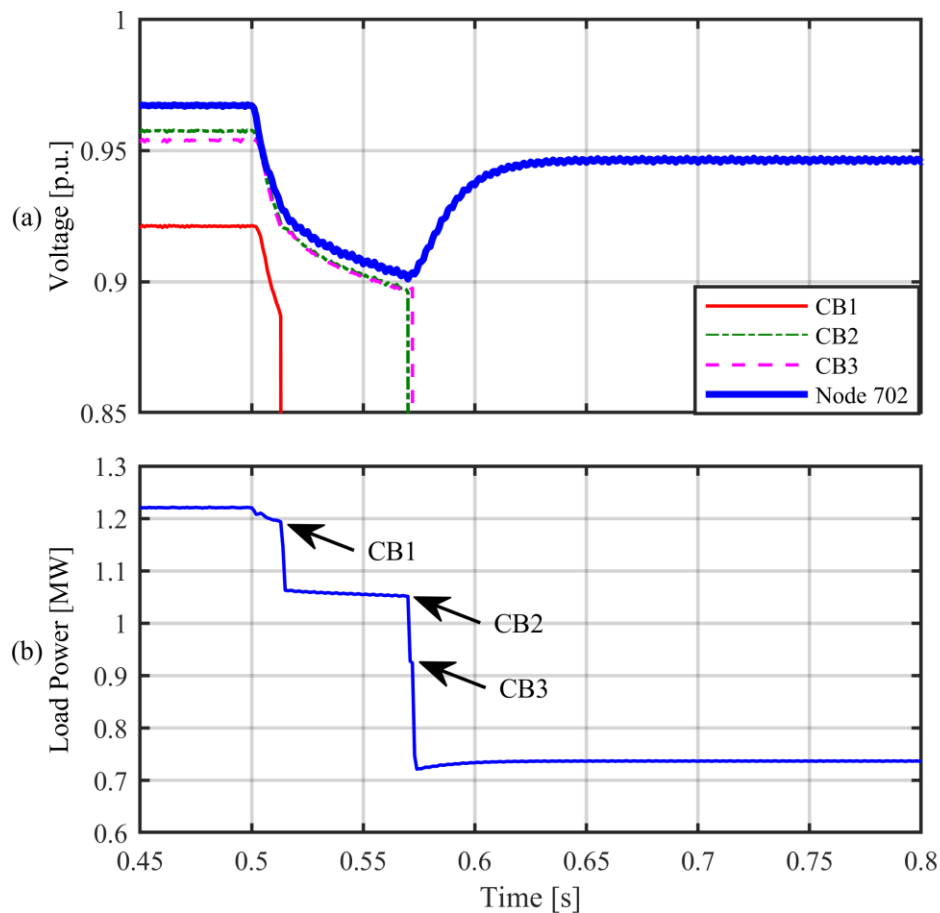


Figure 4.19: Performance of the conventional timer-based load shedding scheme with short delays, in the *Case Study 2*: (a) bus voltages, (b) total power demand of the loads.

At $t = 0.5$ s, the DC microgrid is islanded and the GTC power exchange with the AC grid becomes zero. Subsequently, each BESS injects its maximum power of 0.4 MW into the microgrid, to maintain the power balance. However, as the total power received from the DERs is smaller than the power demand of the loads, the bus voltages start to fall. This sub-section investigates and compares the performances of the conventional load shedding scheme (with short and long delays) and the proposed adaptive load shedding scheme, under the aforementioned disturbance.

4.3.2.2.1 Conventional Timer-based Load Shedding Scheme

Figure 4.19 illustrates the performance of the conventional load shedding scheme with short delays, in minimizing the adverse effects of the islanding incident. The conventional scheme with short delays sheds all three groups of the non-critical loads by tripping the

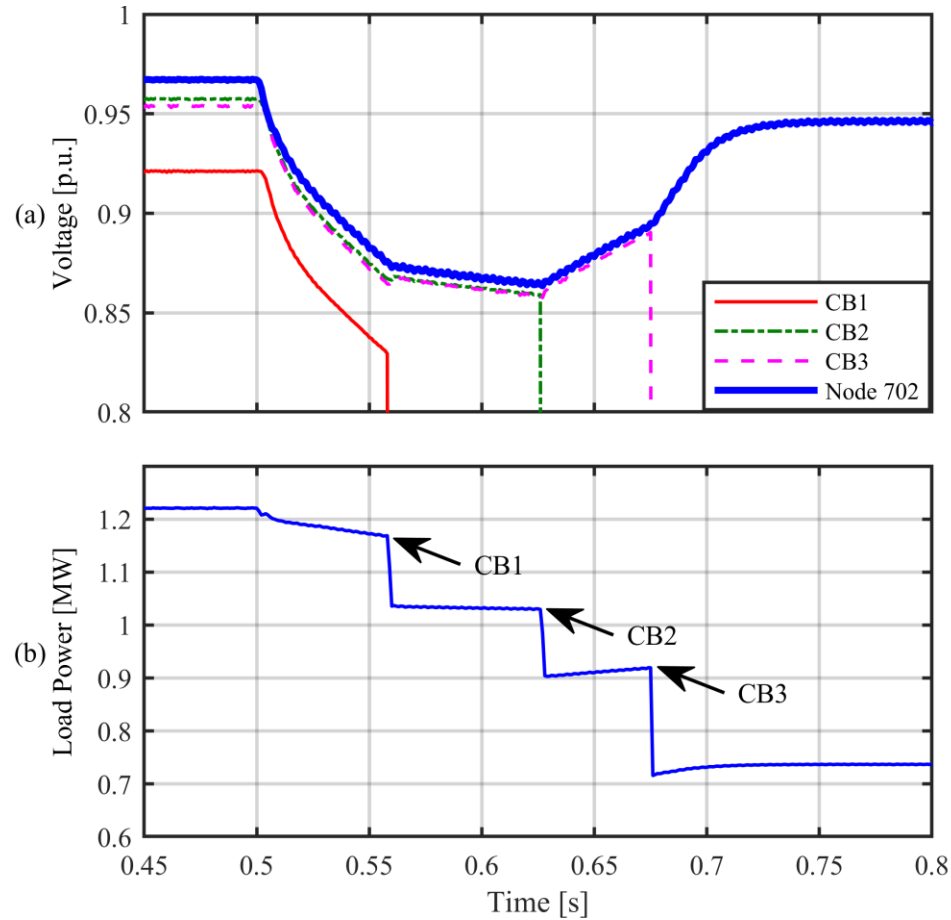


Figure 4.20: Performance of the conventional timer-based load shedding scheme with long delays, in the *Case Study 2*: (a) bus voltages, (b) total power demand of the loads.

CBs 1-3 at $t = 0.513$ s, 0.57 s, and 0.572 s, respectively. Consequently, the voltage seen by the critical loads does not fall below 0.9 p.u., and is regulated at about 0.95 p.u. within a time period of about 0.12 s after the islanding. The study results also indicate that the conventional load shedding scheme with short delays does not provide sufficient time for the bus voltages to reach the acceptable levels, before shedding the next group of loads. This is illustrated in Figure 4.19, at $0.55 < t < 0.6$ s, where the CBs 2 and 3 are tripped almost simultaneously. It is shown in the next part that tripping the CB3 in the *Case Study 2* could be avoided.

Figure 4.20 shows the performance of the conventional load shedding scheme with long delays, under the same disturbance scenario as that of Figure 4.19. As shown in Figure 4.20(b), the non-critical loads are shed by tripping the CBs 1-3 at $t = 0.558$ s, 0.626 s, and

0.675 s, respectively. The conventional load shedding scheme with long delays fails to shed the first group of non-critical loads in a timely manner, and thus causes a larger voltage drop before any loads are shed. This is illustrated in Figure 4.20, at $0.5 < t < 0.55$ s. As a result, the voltage seen by the critical loads drops to 0.86 p.u., and is eventually regulated at about 0.95 p.u. within 0.22 s after the disturbance. Figure 4.20 (a) also shows that the third load shedding step was not necessary, because the voltage seen by the critical loads starts to rise at a considerable rate after the second group of loads is shed. The critical load voltage would reach about 0.925 p.u., if CB3 was not tripped.

The results of Figures 4.19 and 4.20 indicate that utilizing fixed time delays for the conventional timer-based load shedding scheme may lead to over-shedding of non-critical loads under less severe disturbances. This may take place regardless of whether short or long fixed delays are utilized.

4.3.2.2 Adaptive Timer-based Load Shedding Scheme

Figure 4.21 illustrates the performance of the proposed adaptive load shedding scheme under the disturbance of Figure 4.19. The proposed scheme sheds two groups of the non-critical loads by tripping the CB1 and CB2 at $t = 0.513$ s, and 0.665 s, respectively. The CB1 is tripped fast, because the magnitude of the corresponding ROCOV is large at around $t = 0.52$ s. Consequently, the voltage seen by the critical loads does not fall below 0.885 p.u., and is regulated at 0.92 p.u. within 0.25 s after the disturbance, as illustrated in Figure 4.21(a). The CB3 is not tripped. The reason is that the adaptive scheme prevents unnecessary tripping of the CB3 when the ROCOV becomes positive after the second load shedding step, as shown in Figure 4.21(d) at $t > 0.67$ s.

The results of Figure 4.21 indicate that the adaptive timer-based load shedding scheme (i) reduces the magnitude of the voltage sag by shortening the first load shedding delay when the ROCOV is large, and (ii) prevents over-shedding when the ROCOV is positive or has a small magnitude. Figure 4.22 shows the adaptive time delay characteristics (solid red line) and the operating point trajectory (dotted blue line) of the load shedding algorithms utilized to trip the CBs 1-3, in the *Case Study 2*. Figure 4.22 (c) illustrates that the operating point trajectory of the CB3 load shedding scheme does not cross the

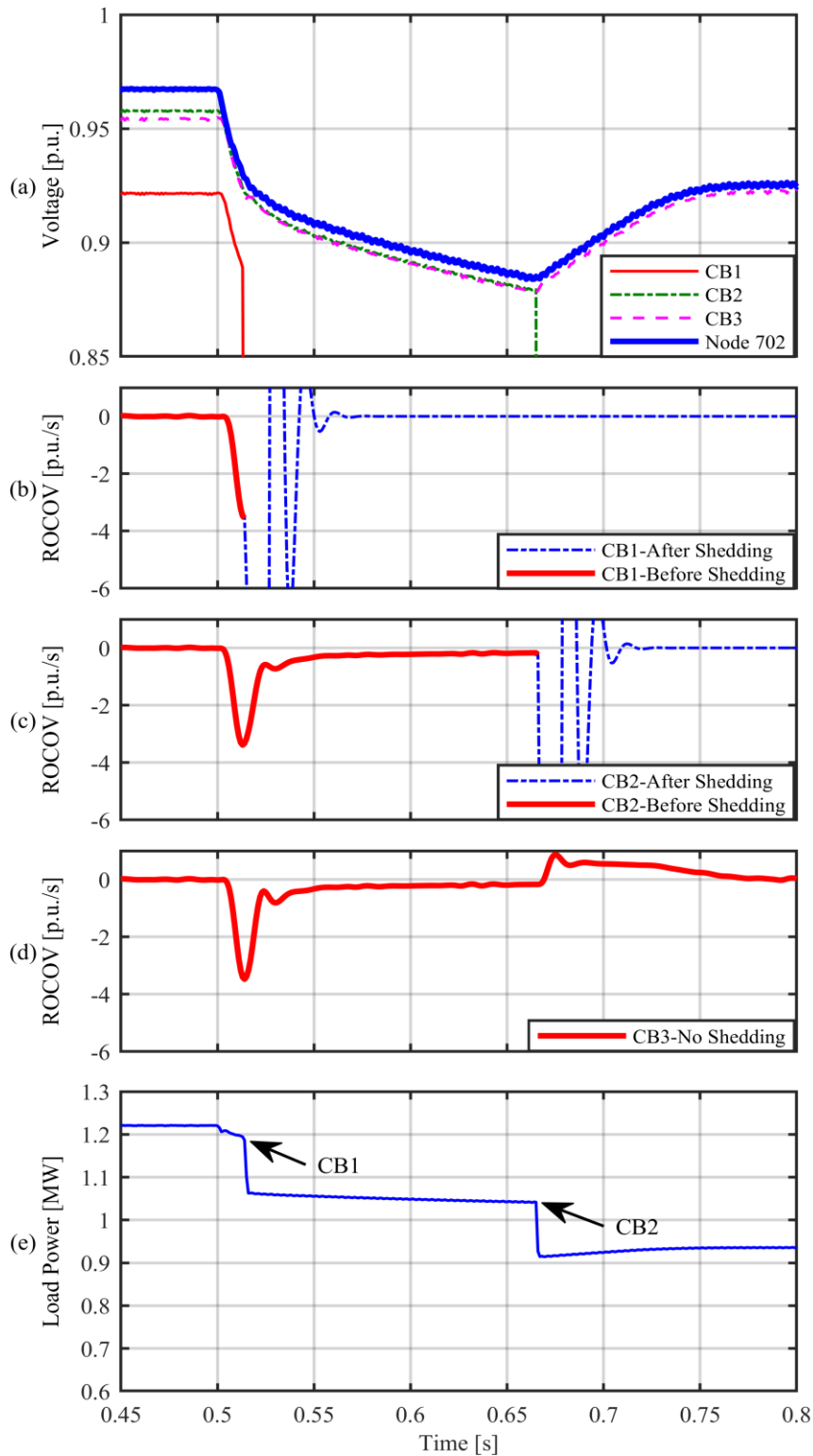


Figure 4.21: Performance of the adaptive timer-based load shedding scheme in the *Case Study 2*: (a) bus voltages, (b) ROCOV at the load-side terminal of CB1, (c) ROCOV at the load-side terminal of CB2, (d) ROCOV at the load-side terminal of CB3 (e) total power demand of the loads.

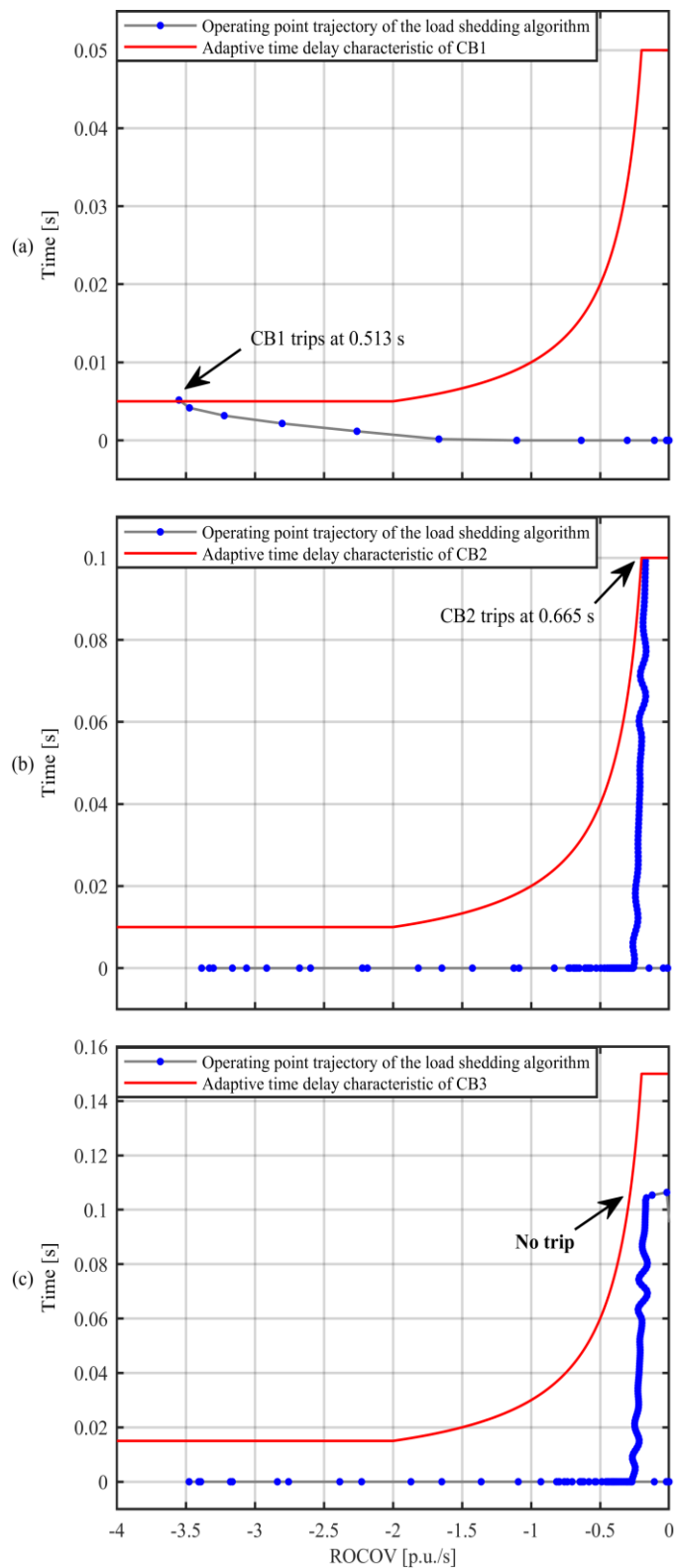


Figure 4.22: Adaptive time-delay characteristics (solid red line) and the operating point trajectory (dotted blue line) of the load shedding algorithms utilized to trip (a) CB1, (b) CB2, and (c) CB3, in the *Case Study 2*.

Table 4.1: Comparison of the conventional and adaptive load shedding schemes.

Case Study	Load Shedding Scheme	V_{min} (p.u.)	V_{final} (p.u.)	Trip Time (s)		
				CB1	CB2	CB3
1	Conventional scheme with short delays	0.89	0.92	0.52	0.54	0.543
	Conventional scheme with long delays	0.72	0.92	0.565	0.626	0.675
	Adaptive scheme	0.875	0.92	0.521	0.542	0.568
2	Conventional scheme with short delays	0.9	0.95	0.513	0.57	0.572
	Conventional scheme with long delays	0.86	0.95	0.558	0.626	0.675
	Adaptive scheme	0.885	0.92	0.513	0.665	-

corresponding adaptive time delay characteristics, which is the reason CB3 is not tripped in this case study.

Table 4.1 compares the performances of the conventional and adaptive timer-based load shedding schemes under the *Case Studies 1* and *2*. In Table 4.1, V_{min} and V_{final} are the minimum and final values of the critical load voltage after the disturbances.

4.4 Conclusions

In this chapter, adaptive voltage and timer-based load shedding schemes are proposed for the DC microgrid. The performance of the proposed load shedding schemes are investigated and compared with those of the conventional voltage and timer-based load shedding schemes, under different disturbances. The study results indicate that the proposed adaptive load shedding schemes:

- utilize the ROCOV to achieve a more reliable assessment of the microgrid operating conditions and determine the appropriate load shedding voltage thresholds and time delays.
- effectively maintain the power balance in the DC microgrid through coordinated shedding of non-critical loads, using locally measured voltages.
- ensure that the bus voltages do not fall below predetermined lower limits, through fast load shedding under high ROCOV conditions.
- more effectively protect the integrity of the DC microgrid, i.e., prevents unnecessary shedding of loads by using more secure, i.e., lower voltage thresholds or longer time delays when the ROCOV is not significant.

- do not suffer from the high cost and potential failures associated with the communication-based schemes.
- limit the magnitude and duration of the voltage sag caused by power deficit in the DC microgrid.
- increase the reliability of the power supplied to the loads by preventing over-shedding.

Chapter 5

5 Conclusions, Contributions, and Future Work

5.1 Summary

The development of the DC microgrid technology requires effective strategies to protect the integrity of the DC microgrid under large disturbances. The main objective of this thesis is to develop advanced control and load shedding strategies to protect the DC microgrid integrity without relying on costly communication systems that may compromise the system reliability.

Chapter 1 presents background information on the DC microgrid, the thesis objectives, literature review and the study system.

In Chapter 2, improved DBS and MADC strategies are proposed to achieve coordinated control of the DERs and GTC in the DC microgrid without utilizing costly high-bandwidth communication systems.

Chapter 3 investigates and compares the performances of the existing non-communication based load shedding schemes in the DC microgrid.

In Chapter 4, adaptive voltage-based and timer-based load shedding schemes are proposed utilizing voltage thresholds and time delays that are automatically adjusted depending on the rate of change of locally measured bus voltages.

Chapter 5 summarizes the thesis contributions and provides concluding remarks.

5.2 Conclusions

The conclusions drawn from this thesis are aligned with the objectives of the research to develop advanced control and load shedding strategies to protect the integrity of the DC microgrid under large disturbances. The conclusions are as follows:

- The proposed DBS control strategy: (i) effectively maintains the power balance in the DC microgrid by properly and quickly changing the voltage-power characteristics of the DERs and the GTC, (ii) effectively limits the DC bus voltage deviations to 0.1 p.u. under large disturbances, (iii) realizes smooth transitions between different operation states, (iv) improves the DC microgrid dynamic response to disturbances, (v) does not require an excessively large GTC or BESSs, and (vi) enhances the DC microgrid reliability, flexibility, modularity, and expandability.
- The proposed MADC strategy: (i) effectively maintains the power balance in the DC microgrid, (ii) effectively regulates the DC bus voltages under various operating conditions, by properly switching the operation modes of the DERs, (iii) improves power sharing between the DERs, (iv) significantly reduces the circulating currents between the DERs in the islanded microgrid, and (v) enables reliable and coordinated operation of the DERs, regardless of how fast the bus voltages change in response to disturbances.
- The proposed DBS control strategy provides better dynamic response to disturbances, since it does not cause extra delay in the DER mode. Thus, it is more suitable for application in relatively small-scale microgrids, where the voltage drops caused by the line resistances are negligible and all the DERs and the GTC measure equal bus voltages. On the other hand, the MADC provides better power sharing performance, and is more suitable for application in large-scale DC microgrids with multiple geographically dispersed DERs, where the voltage drops caused by the line resistances are not negligible.
- The proposed adaptive voltage- and timer-based load shedding schemes: (i) effectively maintain the power balance in the DC microgrid through fast and coordinated shedding of non-critical loads, (ii) ensure that the bus voltages do not fall below predetermined lower limits, through fast load shedding under high ROCOV conditions, (iii) more effectively protect the integrity of the DC microgrid, i.e., prevents unnecessary shedding of loads by using more secure, i.e., lower voltage thresholds or longer time

delays when the ROCOV is not significant, (iv) do not suffer from the high cost and potential failures associated with the communication-based load shedding schemes, (v) minimize the magnitudes and durations of temporary voltage sags caused by sudden disturbances, and (vi) increase the reliability of the power supplied to the loads, by preventing over-shedding.

5.3 Contributions

The thesis presents the following contributions.

- An improved DBS control strategy is proposed to achieve coordinated decentralized control of the DERs and GTC in the DC microgrid without utilizing costly high-bandwidth communication systems. The proposed DBS control strategy utilizes multiple predefined DC voltage ranges to determine the operation modes of the DERs and the GTC. The operation mode of each component changes instantaneously whenever the corresponding bus voltage enters any of the aforementioned ranges.
- An improved MADC strategy is proposed for the DC microgrid to minimize the adverse effects of unequal bus voltages on the coordinated participation of the DERs in regulating bus voltages and maintaining the power balance in the DC microgrid. The proposed MADC strategy delays all mode change actions such that none of the DERs attempts to change its operation mode in response to a voltage disturbance, before all other DERs detect the disturbance.
- An adaptive voltage-based load shedding scheme is proposed utilizing voltage thresholds that are automatically adjusted depending on the rate of change of locally measured bus voltages. It instantaneously sheds a non-critical load whenever its bus voltage falls below the adaptive voltage threshold and its rate of change of voltage is negative.
- An adaptive timer-based load shedding scheme is proposed utilizing time delays that are automatically adjusted depending on the rate of change of locally measured bus voltages. It sheds a non-critical load whenever its bus voltage remains below the common voltage threshold for a time period longer than the corresponding adaptive delay, and its rate of change of voltage is negative.

5.4 Future Work

The study results presented in this thesis provide a platform for future work on integrity protection of the DC microgrid using adaptive control and load shedding strategies. The expected future work that can complement this research includes hardware implementation of the proposed control and load shedding strategies and testing them in a real DC microgrid platform. Adaptive control and load shedding strategies can be also utilized in hybrid microgrids. Developing effective strategies for coordinated control of DERs and shedding of loads in a hybrid microgrid is considered as future work.

Appendix A: Study System Parameters

Table A.1: Parameters of the DC Microgrid

GTC	$S_{Trans} = 1 \text{ MVA}$	Transformer: 0.75kV/4.8 kV
	$S_{GTC} = 1 \text{ MVA}$	$C_{dc} = 20 \text{ mF}$
	$V_{rated} = 750 \text{ V}$	$f_{sw} = 2.7 \text{ kHz}$
	$R_{f-series} = 1 \text{ m}\Omega$	$L_{f-series} = 0.224 \text{ mH}$
	$R_{f-parallel} = 100 \text{ m}\Omega$	$C_{f-parallel} = 500 \text{ }\mu\text{F}$
WT	$P_{WT} = 1 \text{ MW}$	$V_{rated} = 690 \text{ V}$
	$S_{PMSG} = 1.1 \text{ MVA}$	$S_{VSC} = 1.1 \text{ MVA}$
	$\omega_b = 377 \text{ rad/s}$	$f_{rated} = 60 \text{ Hz}$
	$R_s = 0.017 \text{ pu}$	$X_l = 0.064 \text{ pu}$
	$X_d = 0.55 \text{ pu}$	$X_q = 1.1 \text{ pu}$
	$R_{kd} = 0.055 \text{ pu}$	$R_{kq} = 0.183 \text{ pu}$
	$X_{kd} = 0.62 \text{ pu}$	$X_{kq} = 1.175 \text{ pu}$
	$\Psi_f = 1 \text{ pu}$	$C_{dc} = 20 \text{ mF}$
	$H_g = 0.62 \text{ s}$	$H_t = 2.16 \text{ s}$
	$C_{p-nom} = 0.48 \text{ pu}$	$\lambda_{opt} = 8.1$
	$\beta_{min} = 0 \text{ degree}$	$\beta_{max} = 16 \text{ degree}$
	$v_{w-cut-in} = 3 \text{ m/s}$	$v_{w-cut-out} = 25 \text{ m/s}$
	$\rho_{air} = 1.225 \text{ kg/m}^3$	$v_{w-rated} = 12 \text{ m/s}$
PV	$P_{PV} = 2*0.5 \text{ MW} = 1 \text{ MW}$	Irradiation = 0-1000 w/m ²
	$V_{oc} = 973.7 \text{ V}$	$I_{sc} = 714 \text{ A}$
	$T = 25 \text{ C}$	$n = 1.42$
	$k = 1.38 * 10^{-23} \text{ J/K}$	$q = 1.6 * 10^{-19} \text{ C}$
	Cells $N_s = 72$	Modules $N_s = 21$
	Cells $N_p = 1$	Modules $N_p = 70$
	$C_{in} = 300 \text{ }\mu\text{F}$	$L_{in} = 1 \text{ mH}$
	$C_{dc} = 10 \text{ mF}$	$f_{sw} = 2.7 \text{ kHz}$
BESS	$P_{BESS} = 2*0.4 \text{ MW} = 0.8 \text{ MW}$	$V_{rated} = 0.7 \text{ kV}$
	$Q = 0.57 \text{ kAh}$	$L_{in} = 1 \text{ mH}$
	$C_{dc} = 10 \text{ mF}$	$f_{sw} = 2.7 \text{ kHz}$
Load	Total	$P_{Load} = 1228.5 \text{ kW}$
	Critical	$P_{Load} = 758 \text{ kW}$
	Non-critical	$P_{Load} = 470.5 \text{ kW}$
	Constant Power	$P_{CPL} = 758.5 \text{ kW}$
	Constant Current	$P_{CCL} = 254 \text{ kW}$
	Constant Resistance	$P_{CRL} = 216 \text{ kW}$

Table A.2: DC Microgrid Load Data

Node	Type	Power (kW)
701	Constant Power	315
712	Constant Power	42.5
713	Constant Power	42.5
714	Constant Current	19
718	Constant Resistance	42.5
720	Constant Power	42.5
722	Constant Current	80.5
724	Constant Resistance	21
725	Constant Power	21
727	Constant Power	21
728	Constant Power	63
729	Constant Current	21
730	Constant Resistance	42.5
731	Constant Resistance	42.5
732	Constant Power	21
733	Constant Current	42.5
734	Constant Power	21
735	Constant Power	42.5
736	Constant Resistance	21
737	Constant Current	70
738	Constant Power	63
740	Constant Power	42.5
741	Constant Current	21
742	Constant Resistance	46.5
744	Constant Power	21

Table A.3: Cable Lengths and Types

Node A	Node B	Length (m)	Type
701	702	292.6	1
702	705	121.9	1
702	713	109.7	1
702	703	402.3	1
703	727	73.2	4
703	730	182.9	1
704	714	24.4	4
704	720	243.8	1
705	742	97.5	4
705	712	73.2	2
706	725	85.3	4
707	724	231.6	4
707	722	36.6	2
708	733	97.5	2
708	732	97.5	4
709	731	182.9	4
709	708	97.5	2
710	735	61	4
710	736	390.1	4
711	741	121.9	4
711	740	61	4
713	704	158.5	1
714	718	158.5	4
720	707	280.4	1
720	706	182.9	4
727	744	85.3	4
730	709	61	1
733	734	170.7	2
734	737	195.1	2
734	710	158.5	3
737	738	122	3
738	711	122	3
744	728	61	4
744	729	85.3	4
775	709	0	XFM-1

Table A.4: Underground Cable Parameters Per-Unit Length

Type	1	2	3	4
Size	1000 kcmil	250 kcmil	1 AWG	6 AWG
R (m Ω /m)	0.075	0.232	0.599	1.701
L (μ H/m)	0.118	0.181	0.262	0.366
C (nF/m)	0.402	0.216	0.152	0.120

Table A.5: Underground Cable Dimensions

Type	Size	Dimensions (mm)					
		r_1	r_2	r_3	r_4	r_5	r_6
1	1000 kcmil	12.7	14.99	18.1	19.62	24.08	25.54
2	250 kcmil	6.35	8.64	10.635	12.155	15.645	16.99
3	1 AWG	3.674	5.704	7.21	8.35	11.405	12.65
4	6 AWG	2.057	3.577	4.99	5.75	8.8	10.045

Table A.6: Parameters of the PI Controllers [p.u.]

DER	PI-Controlled Variable	K_P	T_I	Output Limits
WT	Stator Currents I_{sq} and I_{sd}	0.5	0.01	-1.3 to 1.3
	Active Power P_{PMSG}	0.2	0.01	0 to 1
	Stator Voltage V_s	2	0.02	-1 to 1
	DC-Terminal Voltage V_{DC}	5	0.003	0 to 1
PV	PV Voltage V_{PV}	2	0.005	0 to 1
	DC-Terminal Voltage V_{DC}	2	0.005	0 to 1
BESS	Battery Current I_{BESS}	2	0.01	0 to 1
	Battery Voltage V_{BESS}	20	0.001	-1 to 1
	DC-Terminal Current I_{dc}	0.1	0.08	0 to 1
	DC-Terminal Voltage V_{DC}	20	0.002	-1 to 1

References

- [1] J. J. Justo, F. Mwasilu, J. Lee and J. W. Jung, “AC-microgrids versus DC-microgrids with distributed energy resources: a review”, *Renew. Sustain. Energy Rev.*, vol. 24, pp. 387–405, Aug. 2013.
- [2] J. Andreu, J. I. Gárate, I. M. de Alegría and E. Ibarra, “AC and DC technology in microgrids: a review” *Renew. Sustain. Energy Rev.*, vol. 43, pp. 726-749, Mar. 2015.
- [3] A. Hirsch, Y. Parag, J. M Guerrero, “Microgrids: a review of technologies, key drivers, and outstanding issues”, *Renew. Sustain. Energy Rev.*, vol. 90, pp. 402-411, Jul. 2018.
- [4] S. Parhizi, H. Lotfi, A. Khodaei and S. Bahramirad, “State of the art in research on microgrids: a review,” *IEEE Access*, vol. 3, pp. 890-925, 2015.
- [5] A. T. Elsayed, A. A. Mohamed, and O. A. Mohammed, “DC microgrids and distribution systems: an overview,” *Electr. Power Syst. Res.*, vol. 119, pp. 407–417, Feb. 2015.
- [6] D. Kumar, F. Zare and A. Ghosh, “DC microgrid technology: system architectures, AC grid interfaces, grounding schemes, power quality, communication networks, applications, and standardizations aspects,” *IEEE Access*, vol. 5, pp. 12230-12256, 2017.
- [7] T. Dragičević, X. Lu, J. C. Vasquez and J. M. Guerrero, “DC microgrids—part II: a review of power architectures, applications, and standardization issues,” *IEEE Trans. Power Elec.*, vol. 31, no. 5, pp. 3528-3549, May 2016.
- [8] T. Dragicevic, J. C. Vasquez, J. M. Guerrero and D. Skrlec, “Advanced LVDC electrical power architectures and microgrids: a step toward a new generation of power distribution networks,” *IEEE Electrification Magazine*, vol. 2, no. 1, pp. 54-65, Mar. 2014.
- [9] T. Dragičević, X. Lu, J. C. Vasquez and J. M. Guerrero, “DC microgrids—part I: a review of control strategies and stabilization techniques,” *IEEE Trans. Power Electron.*, vol. 31, no. 7, pp. 4876-4891, Jul. 2016.

- [10] L. Meng, Q. Shafiee, G. F. Trecate, H. Karimi, D. Fulwani, X. Lu and J. M. Guerrero, "Review on control of DC microgrids and multiple microgrid clusters," *IEEE Journal of Emerging and Selected Topics in Power Electronics*, vol. 5, no. 3, pp. 928-948, Sept. 2017.
- [11] M. Kumar, S. C. Srivastava and S. N. Singh, "Control strategies of a DC microgrid for grid connected and islanded operations," *IEEE Trans. Smart Grid*, vol. 6, no. 4, pp. 1588-1601, Jul. 2015.
- [12] J. P. Torreglosa, P. G. Triviño, L. M. F. Ramirez and F. Jurado "Control strategies for DC networks: a systematic literature review," *Elsevier, Renew. Sustain. Energy Reviews*, vol. 58, pp. 319-330, May 2016.
- [13] S. K. Sahoo, A. K. Sinha and N. K. Kishore, "Control techniques in AC, DC, and hybrid AC–DC microgrid: a review," *IEEE Journal of Emerging and Selected Topics in Power Electron.*, vol. 6, no. 2, pp. 738-759, Jun. 2018.
- [14] N. N. A. Bakar, M. Y. Hassan, M. F. Sulaima, M. N. M. Nasir and A. Khamis, "Microgrid and load shedding scheme during islanded mode: A review," *Renew. Sustain. Energy Rev.*, vol. 71, pp.161-169, May. 2017.
- [15] N. M. Sapari, H. Mokhlis, J. A. Laghari, A. H. A. Bakar and M. R. M. Dahalan "Application of LS schemes for distribution network connected with distributed generation: A review," *Renew. Sustain. Energy Rev.*, vol. 82, pp.858-867, Feb. 2018.
- [16] M. Sechilariu and F. Locment, Urban DC microgrid: intelligent control and power flow optimization. *Elsevier*, 2016.
- [17] B. Wang, M. Sechilariu and F. Locment, "Intelligent DC microgrid with smart grid communications: control strategy consideration and design," *IEEE Trans. Smart Grid*, vol. 3, no. 4, pp. 2148-2156, Dec. 2012.
- [18] A. G. Tsikalakis, and N. D. Hatziargyriou, "Centralized control for optimizing microgrids operation", *IEEE Trans. Energy Convers.*, vol. 23, no. 1, pp. 241-248, 2008.
- [19] K. T. Tan, X. Y. Peng, P. L. So, Y. C. Chu and M. Z. Q. Chen, "Centralized control for parallel operation of distributed generation inverters in microgrids," *IEEE Trans. Smart Grid*, vol. 3, no. 4, pp. 1977-1987, Dec. 2012.

- [20] J. Rajagopalan, K. Xing, Y. Guo, F. C. Lee and B. Manners, "Modeling and dynamic analysis of paralleled DC/DC converters with master-slave current sharing control," *Proceedings of Applied Power Electronics Conference. APEC '96*, San Jose, CA, USA, 1996, pp. 678-684, vol. 2.
- [21] T. F. Wu, Y. K. Chen and Y. H. Huang, "3C strategy for inverters in parallel operation achieving an equal current distribution," *IEEE Trans. Ind. Electron.*, vol. 47, no. 2, pp. 273-281, Apr. 2000.
- [22] D. Dam and H. Lee, "A power distributed control method for proportional load power sharing and bus voltage restoration in a DC microgrid," *IEEE Trans. Ind. Appl.*, vol. 54, no. 4, pp. 3616-3625, Jul.-Aug. 2018.
- [23] F. Guo, Q. Xu, C. Wen, L. Wang and P. Wang, "Distributed secondary control for power allocation and voltage restoration in islanded DC microgrids," *IEEE Trans. Sust. Energy*, vol. 9, no. 4, pp. 1857-1869, Oct. 2018.
- [24] R. Han, L. Meng, J. M. Guerrero and J. C. Vasquez, "Distributed nonlinear control with event-triggered communication to achieve current-sharing and voltage regulation in DC microgrids," *IEEE Trans. Power Electron.*, vol. 33, no. 7, pp. 6416-6433, Jul. 2018.
- [25] Q. Shafiee, J. M. Guerrero and J. C. Vasquez, "Distributed secondary control for islanded microgrids—a novel approach," *IEEE Trans. Power Electron.*, vol. 29, no. 2, pp. 1018-1031, Feb. 2014.
- [26] V. Nasirian, S. Moayedi, A. Davoudi and F. L. Lewis, "Distributed cooperative control of DC microgrids," *IEEE Trans. Power Electron.*, vol. 30, no. 4, pp. 2288-2303, Apr. 2015.
- [27] Q. Shafiee, T. Dragičević, J. C. Vasquez and J. M. Guerrero, "Hierarchical control for multiple DC-microgrids clusters," *IEEE Trans. Energy Convers.*, vol. 29, no. 4, pp. 922-933, Dec. 2014.
- [28] C. Jin, P. Wang, J. Xiao, Y. Tang and F. H. Choo, "Implementation of hierarchical control in DC microgrids," *IEEE Trans. Ind. Electron.*, vol. 61, no. 8, pp. 4032-4042, Aug. 2014.

- [29] L. Che and M. Shahidehpour, "DC microgrids: economic operation and enhancement of resilience by hierarchical control," *IEEE Trans. Smart Grid*, vol. 5, no. 5, pp. 2517-2526, Sep. 2014.
- [30] C. Wang, J. Duan, B. Fan, Q. Yang and W. Liu, "Decentralized high-performance control of DC microgrids," *IEEE Trans. Smart Grid*, vol. 10, no. 3, pp. 3355-3363, May 2019.
- [31] S. Peyghami, H. Mokhtari, P. Davari, P. C. Loh and F. Blaabjerg, "On secondary control approaches for voltage regulation in DC microgrids," *IEEE Trans. Ind. Appl.*, vol. 53, no. 5, pp. 4855-4862, Sept.-Oct. 2017.
- [32] P. Sanjeev, N. P. Padhy and P. Agarwal, "Autonomous power control and management between standalone DC microgrids," *IEEE Trans. Ind. Inform.*, vol. 14, no. 7, pp. 2941-2950, Jul. 2018.
- [33] P. Prabhakaran, Y. Goyal and V. Agarwal, "Novel nonlinear droop control techniques to overcome the load sharing and voltage regulation issues in DC microgrid," *IEEE Trans. Power Electron.*, vol. 33, no. 5, pp. 4477-4487, May 2018.
- [34] X. Lu, K. Sun, J. M. Guerrero, J. C. Vasquez and L. Huang, "State-of-charge balance using adaptive droop control for distributed energy storage systems in DC microgrid applications," *IEEE Trans. Ind. Electron.*, vol. 61, no. 6, pp. 2804-2815, Jun. 2014.
- [35] X. Lu, K. Sun, J. M. Guerrero, J. C. Vasquez and L. Huang, "Double quadrant state-of-charge-based droop control method for distributed energy storage systems in autonomous DC microgrids," *IEEE Trans. Smart Grid*, vol. 6, no. 1, pp. 147-157, Jan. 2015.
- [36] S. Augustine, M. K. Mishra and N. Lakshminarasamma, "Adaptive droop control strategy for load sharing and circulating current minimization in low-voltage standalone dc microgrid," *IEEE Trans. Sust. Energy.*, vol. 6, no. 1, pp. 132-141, Jan. 2015.
- [37] J. Schonbergerschonberger, R. Duke and S. D. Round, "DC-bus signaling: a distributed control strategy for a hybrid renewable nanogrid," *IEEE Trans. Ind. Electron.*, vol. 53, no. 5, pp. 1453-1460, Oct. 2006.

- [38] K. Sun, L. Zhang, Y. Xing and J. M. Guerrero, "A distributed control strategy based on DC bus signaling for modular photovoltaic generation systems with battery energy storage," *IEEE Trans. Power Electron.*, vol. 26, no. 10, pp. 3032-3045, Oct. 2011.
- [39] N. Eghtedarpour and E. Farjah, "Control strategy for distributed integration of photovoltaic and energy storage systems in DC micro-grids", *Renew. Energy*, vol. 45, pp. 96–110, Sept. 2012.
- [40] Y. Gu, W. Li and X. He, "Frequency-coordinating virtual impedance for autonomous power management of DC microgrid," *IEEE Trans. Power Electron.*, vol. 30, no. 4, pp. 2328-2337, Apr. 2015.
- [41] Y. Gu, X. Xiang, W. Li and X. He, "Mode-adaptive decentralized control for renewable DC microgrid with enhanced reliability and flexibility," *IEEE Trans. Power Electron.*, vol. 29, no. 9, pp. 5072-5080, Sept. 2014.
- [42] L. Gao, Y. liu, H. Ren, J. M. Guerrero, "A DC microgrid coordinated control strategy based on integrator current-sharing", *Energies, MDPI, Open Acces Journal*, vol. 10, no. 8, pp. 1–17, Aug. 2017.
- [43] J. Meng, Y. Wang, C. Wang and H. Wang, "Design and implementation of hardware-in-the-loop simulation system for testing control and operation of DC microgrid with multiple distributed generation units", *IET Gener. Transm. Distrib.*, vol. 11, no. 12, pp. 3065–3072, Aug. 2017.
- [44] D. Chen, L. Xu and L. Yao, "DC voltage variation based autonomous control of DC microgrids," *IEEE Trans. Power Delivery*, vol. 28, no. 2, pp. 637-648, Apr. 2013.
- [45] D. Wu, F. Tang, T. Dragicevic, J. M. Guerrero and J. C. Vasquez, "Coordinated control based on bus-signaling and virtual inertia for islanded DC microgrids," *IEEE Trans. Smart Grid*, vol. 6, no. 6, pp. 2627-2638, Nov. 2015.
- [46] Y. Wang, M. Yu and Y. Li, "Self-adaptive inertia control of DC microgrid based on fast predictive converter regulation," *IET Renew. Power Gener.*, vol. 11, no. 8, pp. 1295-1303, Jul. 2017.
- [47] Y. Xia, M. Yu, P. Yang, Y. Peng and W. Wei, "Generation-storage coordination for islanded DC microgrids dominated by PV generators," *IEEE Trans. Energy Convers.*, vol. 34, no. 1, pp. 130-138, Mar. 2019.

- [48] N. L. Diaz, T. Dragičević, J. C. Vasquez and J. M. Guerrero, “Intelligent distributed generation and storage units for DC microgrids—a new concept on cooperative control without communications beyond droop control,” *IEEE Trans. Smart Grid*, vol. 5, no. 5, pp. 2476-2485, Sept. 2014.
- [49] Q. Yang, L. Jiang, H. Zhao and H. Zeng, “Autonomous voltage regulation and current sharing in islanded multi-inverter DC microgrid,” *IEEE Trans. Smart Grid*, vol. PP, pp. 1–1, 2017.
- [50] D. Chen and L. Xu, “Autonomous DC voltage control of a DC microgrid with multiple slack terminals,” *IEEE Trans. Power Systems*, vol. 27, no. 4, pp. 1897-1905, Nov. 2012.
- [51] L. Xu and D. Chen, “Control and operation of a DC microgrid with variable generation and energy storage,” *IEEE Trans. Power Delivery*, vol. 26, no. 4, pp. 2513-2522, Oct. 2011.
- [52] A. Khorsandi, M. Ashourloo and H. Mokhtari, “A decentralized control method for a low voltage DC microgrid,” *IEEE Trans. Energy Convers.*, vol. 29, no. 4, pp. 793-801, Dec. 2014.
- [53] T. Dragičević, J. M. Guerrero, J. C. Vasquez and D. Škrlec, “Supervisory control of an adaptive-droop regulated DC microgrid with battery management capability,” *IEEE Trans. Power Electron.*, vol. 29, no. 2, pp. 695-706, Feb. 2014.
- [54] M. Sechilariu, B. C. Wang, F. Locment and A. Jouglet, “DC microgrid power flow optimization by multi-layer supervision control. design and experimental validation,” *Energy Convers. Manag.* vol. 82, pp. 1–10, Jun. 2014.
- [55] M. Sechilariu, B. C. Wang, and F. Locment, “Supervision control for optimal energy cost management in DC microgrid: design and simulation,” *Int. J. Elec. Power Energy Syst.* vol. 58, pp. 140–149, Jun. 2014.
- [56] P. Sanjeev, N. P. Padhy and P. Agarwal, “Peak energy management using renewable integrated DC microgrid,” *IEEE Trans. Smart Grid*, vol. 9, no. 5, pp. 4906-4917, Sept. 2018.
- [57] M. Sechilariu, F. Locment, and B. Wang, “Photovoltaic electricity for sustainable building. efficiency and energy cost reduction for isolated DC microgrid,” *Energies*, vol. 8, no.8, pp. 7945–7967, Jul. 2015.

- [58] H. Wu, M. Sechilariu and F. Locment, "Influence of dynamic efficiency in the DC microgrid power balance," *Energies*, vol. 10, no. 10, pp. 1563-1580, Oct. 2017.
- [59] L.T.D. Santos, M. Sechilariu, and F. Locment, "Optimized load shedding approach for grid-connected DC microgrid systems under realistic constraints," *Buildings*, vol. 6, no. 4, Dec. 2016.
- [60] L.T.D. Santos, M. Sechilariu and F. Locment, "Day-ahead microgrid optimal self-scheduling: comparison between three methods applied to isolated DC microgrid," *IECON 2014-40th Annual Conference of the IEEE Industrial Electronics Society*, Dallas, TX, 2014, pp. 2010-2016.
- [61] T. D. Khoa, L. T. Dos Santos, M. Sechilariu and F. Locment, "Load shedding and restoration real-time optimization for DC microgrid power balancing," *2016 IEEE International Energy Conference (ENERGYCON)*, Leuven, 2016, pp. 1-6.
- [62] L. T. D. Santos, M. Sechilariu and F. Locment, "Prediction-based economic dispatch and online optimization for grid-connected DC microgrid," *IEEE Int. Energy Conf.*, Leuven, 2016, pp. 1-6.
- [63] M. Sechilariu, F. Locment and L. T. D. Santos, "A conceptual framework for full optimal operation of a grid-connected DC microgrid," *IEEE Int. Conf. on Ind. Elec. for Sust. Energy Sys.*, Hamilton, 2018, pp. 296-301.
- [64] D. Dam and H. Lee, "An adaptive power distributed control method to ensure proportional load power sharing in DC microgrid considering equivalent line impedances," *2016 IEEE Energy Conversion Congress and Exposition (ECCE)*, Milwaukee, WI, 2016, pp. 1-6.
- [65] D. Rwegasira, I. B. Dhaou, A. Anagnostou *et al.*, "A framework for load shedding and demand response in DC microgrid using multi agent system," *21st Conference of Open Innovations Association (FRUCT)*, Helsinki, 2017, pp. 284-289.
- [66] D. Rwegasira, I. B. Dhaou, A. Kondoro *et al.*, "A multi-agent system for solar driven DC microgrid," *Int. Conf. on Control, Electronics, Renewable Energy and Communications (ICCREC)*, Yogyakarta, 2017, pp. 252-257.

- [67] D. Rwegasira, N. Mvungi and H. Tenhunen, "Agent based system for improved control and monitoring of a solar driven DC microgrid," *2018 IEEE PES/IAS PowerAfrica*, Cape Town, 2018, pp. 890-894.
- [68] L. Zhang, Y. Wang, H. Li and P. Sun, "Hierarchical coordinated control of DC microgrid with wind turbines," *IECON 2012-38th Annual Conference on IEEE Industrial Electronics Society*, Montreal, QC, 2012, pp. 3547-3552.
- [69] H. Wen, K. Zheng and Y. Du, "Hierarchical coordinated control for DC microgrid with crowbar and load shedding control," *2017 IEEE 3rd International Future Energy Electronics Conference and ECCE Asia (IFEEC 2017-ECCE Asia)*, Kaohsiung, 2017, pp. 2208-2212.
- [70] S. Sahoo and S. Mishra, "A multi-objective adaptive control framework in autonomous DC microgrid," *IEEE Trans. Smart Grid*, vol. 9, no. 5, pp. 4918-4929, Sept. 2018.
- [71] A. Garg, B. M. Joshi and R. Oruganti, "Modeling a DC microgrid with real time power management using DC bus signalling," *IEEE Energy Conv. Congress and Expo. (ECCE)*, Portland, OR, 2018, pp. 46-53.
- [72] J. Schonberger, S. Round and R. Duke, "Autonomous load shedding in a nanogrid using DC bus signalling," *IECON 2006-32nd Annual Conference on IEEE Industrial Electronics*, Paris, 2006, pp. 5155-5160.
- [73] D. Chen and L. Xu, "DC microgrid with variable generations and energy storage," *IET Conference on Renewable Power Generation (RPG 2011)*, Edinburgh, 2011, pp. 1-6.
- [74] J. Mohammadi, and F. B. Ajaei, "Versatile decentralized control of the DC microgrid," *IET Smart Grid*, vol. 2, no. 1, pp. 77-88, Mar. 2019.
- [75] J. Mohammadi, and F. B. Ajaei, "Improved mode-adaptive droop control strategy for the DC microgrid," *IEEE Access*, vol. 7, pp. 86421-86435, Jun. 2019.
- [76] J. Mohammadi, and F. B. Ajaei, "DC microgrid load shedding schemes," *2019 IEEE/IAS 55th Ind. and Commer. Power Systems Technical Conference (I&CPS)*, Calgary, AL, Canada, 2019, pp. 1-7.
- [77] J. Mohammadi, and F. B. Ajaei, "Adaptive voltage-based load shedding scheme for the DC microgrid," *IEEE Access*, vol. 7, pp. 106002-106010, Aug. 2019.

- [78] IEEE 37 Node Test Feeder, IEEE Distribution Test Feeder Working Group Report. [Online]. Available: <http://sites.ieee.org/pes-testfeeders/resources/>
- [79] E. Rodriguez-Diaz, F. Chen, J. C. Vasquez, J. M. Guerrero, R. Burgos and D. Boroyevich “Voltage-level selection of future two-level LVdc distribution grids: a compromise between grid compatibility, safety, and efficiency,” *IEEE Electrification Magazine*, vol. 4, no. 2, pp. 20-28, June 2016.
- [80] H. Kakigano, Y. Miura and T. Ise, “Low-voltage bipolar-type DC microgrid for super high quality distribution,” *IEEE Trans. Power Electron.*, vol. 25, no. 12, pp. 3066-3075, Dec. 2010.
- [81] J. Mohammadi, F. B. Ajaei, and G. Stevens, “DC microgrid grounding strategies,” *2018 IEEE/IAS 54th Ind. and Commer. Power Systems Technical Conference (I&CPS)*, Niagara Falls, ON, Canada, 2018, pp. 1-6.
- [82] J. Mohammadi, F. B. Ajaei, and G. Stevens, “Grounding the DC microgrid,” *IEEE Trans. Ind. Appl.*, 2019.
- [83] B. Wu, Y. Lang, N. Zargari, and S. Kouro, Power conversion and control of wind energy systems. Hoboken, NJ: Wiley, 2011.
- [84] M. Jahanpour-Dehkordi, S. Vaez-Zadeh, and J. Mohammadi, “Development of a combined control system to improve performance of a PMSG based wind energy conversion system under normal and grid fault conditions,” *IEEE Trans. Energy Convers.*, vol. 34, no. 3, pp. 1287-1295, Sept. 2019.
- [85] P. Kou, D. Liang, J. Wang and L. Gao, “Stable and optimal load sharing of multiple PMSGs in an islanded DC microgrid,” *IEEE Trans. Energy Convers.*, vol. 33, no. 1, pp. 260-271, Mar. 2018.
- [86] O. Tremblay, L. A. Dessaint and A. I. Dekkiche, “A generic battery model for the dynamic simulation of hybrid electric vehicles,” *2007 IEEE Vehicle Power and Propulsion Conference*, Arlington, TX, 2007, pp. 284-289.
- [87] Amirnaser Yazdani, and Reza Iravani, Voltage-sourced converters in power systems: modeling, control, and applications. Hoboken, NJ: Wiley, 2010.
- [88] J. Mohammadi, S. Vaez-Zadeh, E. Ebrahimzadeh, and F. Blaabjerg, “A combined control method for grid side converter of doubly fed induction generator based wind

- energy conversion systems, “*IET Renew. Power Gener.*, vol. 12, no. 8, pp. 943-952, Jun. 2018.
- [89] F. Zhao, N. Li, Z. Yin and X. Tang, “Small-signal modeling and stability analysis of DC microgrid with multiple type of loads,” *2014 International Conference on Power System Technology*, Chengdu, 2014, pp. 3309-3315.
- [90] D. Salomonsson and A. Sannino, “Load modelling for steady-state and transient analysis of low-voltage DC systems,” *IET Electric Power Appl.*, vol. 1, no. 5, pp. 690-696, Sept. 2007.
- [91] D. Nilsson and A. Sannino, “Load modelling for steady-state and transient analysis of low-voltage dc systems,” *Conference Record of the 2004 IEEE Industry Applications Conference, 2004. 39th IAS Annual Meeting.*, Seattle, WA, USA, 2004, pp. 774-780, vol.2.
- [92] N. Bottrell, M. Prodanovic and T. C. Green, “Dynamic stability of a microgrid with an active load,” *IEEE Trans. Power Electron.*, vol. 28, no. 11, pp. 5107-5119, Nov. 2013.
- [93] A. Emadi, A. Khaligh, C. H. Rivetta and G. A. Williamson, “Constant power loads and negative impedance instability in automotive systems: Definition, modeling, stability, and control of power electronic converters and motor drives,” *IEEE Trans. Veh. Technol.*, vol. 55, no. 4, pp. 1112–1125, Jul. 2006.
- [94] General Cable. 600V-28kV TECK90 XLPE/PVC/AIA/PVC Armored Control and Power Cables. [Online]. Available: <http://www.generalcable.com>.
- [95] X. Lu, J. M. Guerrero, K. Sun and J. C. Vasquez, “An improved droop control method for DC microgrids based on low bandwidth communication with DC bus voltage restoration and enhanced current sharing accuracy,” *IEEE Trans. Power Electron.*, vol. 29, no. 4, pp. 1800-1812, Apr. 2014.
- [96] C. N. Papadimitriou, E. I. Zountouridou, and N. D. Hatziargyriou, “Review of hierarchical control in DC microgrids”, *Electr. Power Syst. Research*, vol. 122, pp. 159–167, May. 2015.

Curriculum Vitae

Name: Jafar Mohammadi

Post-secondary Education and Degrees: The University of Western Ontario
London, ON, Canada
2016-2019, Ph.D. in Electrical Engineering

University of Tehran
Tehran, Iran
2010-2012, M.Sc. in Electrical Engineering

University of Mazandaran
Babolsar, Iran
2005-2009, B.Sc. in Electrical Engineering

Honors and Awards: Graduate Student Award for Excellence in Research
The University of Western Ontario, Canada, 2019.

ECE Graduate Student Research Award
The University of Western Ontario, Canada, 2019.

Western Graduate Research Scholarship
The University of Western Ontario, Canada, 2016-2019.

Hydro One Graduate Scholarship
Hydro One Inc. Canada, 2018.

Mitacs Accelerate Award
Mitacs, Canada, 2017.

Related Work Experience Graduate Research Assistant
The University of Western Ontario.
2016-2019.

Graduate Teaching Assistant
The University of Western Ontario.
2016-2019.

Mitacs Accelerate Research Intern
S2e Technologies Inc. ON, Canada.
2017.

Publications:

Peer-Reviewed Journals:

1. J. Mohammadi, S. Vaez-Zadeh, S. Afsharnia, and E. Daryabeigi, "A combined vector and direct power control for DFIG based wind turbines," *IEEE Trans. Sust. Energy*, vol. 5, no. 3, pp. 767-775, Jul. 2014.
2. J. Mohammadi, S. Afsharnia, and S. Vaez-Zadeh, "Efficient fault ride through control strategy of DFIG-based wind turbines during the grid faults," *Energy Convers. Manage.*, vol. 78, pp. 88-95, Feb. 2014.
3. J. Mohammadi, S. Afsharnia, S. Vaez-Zadeh, and S. Farhangi, "Improved fault ride through strategy for doubly fed induction generator based wind turbines under both symmetrical and asymmetrical grid faults," *IET Renew. Power Gener.*, vol. 10, no. 8, pp. 1114-1122, Sep. 2016.
4. J. Mohammadi, S. Afsharnia, E. Ebrahimzadeh, and F. Blaabjerg, "An enhanced LVRT scheme for DFIG-based WECSs under both balanced and unbalanced grid voltage sags," *Electric Power Components and Systems*, vol. 45, no. 11, pp. 1242-1252, Jul. 2017.
5. J. Mohammadi, S. Vaez-Zadeh, E. Ebrahimzadeh, and F. Blaabjerg, "A combined control method for grid side converter of doubly fed induction generator based wind energy conversion systems," *IET Renew. Power Gener.*, vol. 12, no. 8, pp. 943-952, Jun. 2018.
6. J. Mohammadi, F. Badrkhani Ajaei, and G. Stevens, "Grounding the AC microgrid," *IEEE Trans. Ind. Appl.*, vol. 55, no. 1, pp. 98-105, Jan.-Feb. 2019.
7. J. Mohammadi, F. Badrkhani Ajaei, and G. Stevens, "Grounding the DC microgrid," *IEEE Trans. Ind. Appl.*, 2019.
8. J. Mohammadi, and F. Badrkhani Ajaei, "Versatile decentralized control of the DC microgrid," *IET Smart Grid*, vol. 2, no. 1, pp. 77-88, Mar. 2019.
9. J. Mohammadi, and F. Badrkhani Ajaei, "Improved mode-adaptive droop control strategy for the DC microgrid," *IEEE Access*, vol. 7, pp. 86421-86435, Jun. 2019.
10. J. Mohammadi, and F. Badrkhani Ajaei, "Adaptive voltage-based load shedding scheme for the DC microgrid," *IEEE Access*, vol. 7, pp. 106002-106010, Aug. 2019.
11. M. Jahanpour-Dehkordi, S. Vaez-Zadeh, and J. Mohammadi, "Development of a combined control system to improve performance of a PMSG based wind energy conversion system under normal and grid fault conditions," *IEEE Trans. Energy Convers.*, vol. 34, no. 3, pp. 1287-1295, Sept. 2019.

Refereed Conferences:

1. J. Mohammadi, F. Badrkhani Ajaei, and G. Stevens, "AC microgrid grounding strategies," *2018 IEEE/IAS 54th Ind. and Commer. Power Systems Tech. Conference (I&CPS)*, Niagara Falls, ON, Canada, 2018, pp. 1-7.
2. J. Mohammadi, F. Badrkhani Ajaei, and G. Stevens, "DC microgrid grounding strategies," *2018 IEEE/IAS 54th Ind. and Commer. Power Systems Tech. Conference (I&CPS)*, Niagara Falls, ON, Canada, 2018, pp. 1-6.
3. J. Mohammadi, and F. Badrkhani Ajaei, "DC microgrid load shedding schemes," *2019 IEEE/IAS 55th Ind. and Commer. Power Systems Tech. Conference (I&CPS)*, Calgary, AL, Canada, 2019, pp. 1-7.
4. H. Lahiji, J. Mohammadi, F. Badrkhani Ajaei, and R. Boudreau, "Damping power oscillations in the inverter-dominated microgrid," *2018 IEEE Electrical Power and Energy Conference (EPEC)*, Toronto, Canada, 2018.
5. F. Badrkhani Ajaei, J. Mohammadi, G. Stevens, and E. Akhavan, "Hybrid AC/DC microgrid configurations for a net-zero energy community," *2019 IEEE/IAS 55th Ind. and Commer. Power Systems Technical Conference (I&CPS)*, Calgary, AL, Canada, 2019, pp. 1-7.